

UNCLASSIFIED

AD NUMBER

ADB026145

LIMITATION CHANGES

TO:

Approved for public release; distribution is unlimited.

FROM:

Distribution authorized to U.S. Gov't. agencies only; Test and Evaluation; FEB 1977. Other requests shall be referred to Army Electronics Command, Fort Monmouth, NJ.

AUTHORITY


USAETD:L ltr 21 Jul 1978

THIS PAGE IS UNCLASSIFIED

THIS REPORT HAS BEEN DELIMITED  
AND CLEARED FOR PUBLIC RELEASE  
UNDER DOD DIRECTIVE 5200.20 AND  
NO RESTRICTIONS ARE IMPOSED UPON  
ITS USE AND DISCLOSURE.

DISTRIBUTION STATEMENT A

APPROVED FOR PUBLIC RELEASE;  
DISTRIBUTION UNLIMITED.





Research and Development Technical Report  
ECOM - 75-1357-F

AD B026145

SOURCE DEVELOPMENT FOR MILLIMETER-WAVE APPLICATIONS

Y. Chang  
J. M. Hellums  
J. A. Paul  
K. P. Weller

HUGHES AIRCRAFT COMPANY  
Electron Dynamics Division  
Torrance, CA 90509

February 1977

Final Report for Period 16 June 1975 - 16 June 1976



DISTRIBUTION STATEMENT

Distribution limited to U. S. Government agencies only, test and evaluation; February 1977.  
Other requests for this document must be referred to Commander, U.S. Army Electronics  
Research & Development Command, ATTN: DELET-MJ, Fort Monmouth, NJ 07703.

ECOM

US ARMY ELECTRONICS COMMAND FORT MONMOUTH, NEW JERSEY 07703

DDC FILE COPY

## NOTICES

### Disclaimers

The findings in this report are not to be construed as an official Department of the Army position, unless so designated by other authorized documents.

The citation of trade names and names of manufacturers in this report is not to be construed as official Government indorsement or approval of commercial products or services referenced herein.

### Disposition

Destroy this report when it is no longer needed. Do not return it to the originator.



UNCLASSIFIED

SECURITY CLASSIFICATION OF THIS PAGE (When Data Entered)

19 REPORT DOCUMENTATION PAGE		READ INSTRUCTIONS BEFORE COMPLETING FORM	
1. REPORT NUMBER ECON 75-1357-F	2. GOVT ACCESSION NO.	3. RECIPIENT'S CATALOG NUMBER	
4. TITLE (and Subtitle) SOURCES DEVELOPMENT FOR MILLIMETER-WAVE APPLICATIONS.		5. TYPE OF REPORT & PERIOD COVERED Final Technical Report. 16 Jun 75 - 16 Dec 76.	
7. AUTHOR(s) Y. Chang, J.M. Hellums, J.A. Paul, K.P. Weller		6. PERFORMING ORG. REPORT NUMBER EDD-W-41334-F	
9. PERFORMING ORGANIZATION NAME AND ADDRESS Hughes Aircraft Company Electron Dynamics Division 3100 West Lomita Boulevard, Torrance, CA 90509		10. PROGRAM ELEMENT, PROJECT, TASK AREA & WORK UNIT NUMBERS Feb 1977	
11. CONTROLLING OFFICE NAME AND ADDRESS U.S. Army Electronics Research and Development Command (ERADCOM) ATTN: DRSEL-TL-IJ Fort Monmouth, New Jersey 07703		12. REPORT DATE Feb 1977	
14. MONITORING AGENCY NAME & ADDRESS (if different from Controlling Office)		13. NUMBER OF PAGES 115	
		15. SECURITY CLASS. (of this report) UNCLASSIFIED	
		15a. DECLASSIFICATION/DOWNGRADING SCHEDULE	
16. DISTRIBUTION STATEMENT (of this Report) Distribution limited to U.S. Government agencies only, test and evaluation; Feb. 1977. Other requests for this document must be referred to Commander, U.S. Army Electronics Command, ATTN: DRSEL-TL-IJ, Fort Monmouth, NJ 07703			
17. DISTRIBUTION STATEMENT (of the abstract entered in Block 20, if different from Report)			
18. SUPPLEMENTARY NOTES			
19. KEY WORDS (Continue on reverse side if necessary and identify by block number) Semiconductor diodes      Transmitter oscillators      High data rate Millimeter waves      Varactor-tuned oscillators Double-drift IMPATT      Local oscillators Bit-error-rates      Frequency modulation			
20. ABSTRACT (Continue on reverse side if necessary and identify by block number) The objective of this program is the design, fabrication, testing, and evaluation of 60 GHz and 94 GHz high power FM IMPATT DIODE transmitter oscillators and low noise local oscillators system tested for 100 megabits per second data rate communication at bit error rates (BER) of less than $10^{-7}$ near the FM threshold. During the duration of this program, silicon double-drift IMPATT diodes on both copper and diamond heatsinks have been utilized and IMPATT transmitter oscillators of over 275 mW output power at 94 GHz and over 400 mW output power at 60 GHz have been developed. In addition, varactor tuned			

DD FORM 1 JAN 73 1473

EDITION OF 1 NOV 68 IS OBSOLETE

UNCLASSIFIED

SECURITY CLASSIFICATION OF THIS PAGE (When Data Entered)

402 638 ✓

1B

UNCLASSIFIED

SECURITY CLASSIFICATION OF THIS PAGE(When Data Entered)

IMPATT diode local oscillators at 60 and 94 GHz frequencies have also been developed. System performance evaluation of these oscillators achieved BER of less than  $10^{-8}$  at signal-to-noise ratios meeting the program goal. ↑

10 to the -8th

ADDRESS BY		
WTS	DATE	<input checked="" type="checkbox"/>
ONS	DATE	<input checked="" type="checkbox"/>
UNANNOUNCED		
JUSTIFICATION		
BY		
DISTRIBUTION/AVAILABILITY		
DATE		
AVAIL. NO. OF SPEC.		
B		

UNCLASSIFIED

SECURITY CLASSIFICATION OF THIS PAGE(When Data Entered)

## FORWARD

This project was initiated by the U.S. Army Electronic Command (ECOM) and is under the direction of Mr. A.J. Kerecman. This report is a summation of the entire research program conducted from 16 June 1975 through 16 June 1976.

The work described herein was carried out at the Hughes Aircraft Company, Electron Dynamics Division, 3100 West Lomita Boulevard, Torrance, California 90509 under the program direction of Dr. Y. Chang. Other principal contributors were Mr. J.M. Hellums, Mr. J.A. Paul, and Dr. K.P. Weller.

Project Monitor	U.S. Army Electronic Command A.J. Kerecman
Contract Number	DAAB07-75-C-1357
Contractor's Report Number	EDD W-41334
Reporting Period	16 June 1975 through 16 June 1976
Submitted	March 1977
Authors	Y. Chang, J.M. Hellums, J.A. Paul, and K.P. Weller

Publication of this report does not constitute Army approval of the report's finding or conclusions. It is published only for the exchange and stimulation of ideas.

## TABLE OF CONTENTS

<u>Section</u>	<u>Page</u>
1.0 INTRODUCTION AND SUMMARY	1
2.0 FM IMPATT DIODE TRANSMITTER OSCILLATOR DEVELOPMENT	7
2.1 IMPATT Diode Design	7
2.2 60 GHz FM Oscillators	21
2.2.1 60 GHz IMPATT Oscillator Circuit	21
2.2.2 60 GHz FM IMPATT Diode Transmitter Units (FM IDTUs)	31
2.3 94 GHz FM Transmitter Oscillators	45
2.3.1 94 GHz IMPATT Oscillator Circuit	45
2.3.2 94 GHz IMPATT Diode Transmitter Units (FM IDTUs)	49
3.0 LOW NOISE IMPATT DIODE LOCAL OSCILLATORS DEVELOPMENT	63
3.1 Varactor Tuned Oscillators (VTOs)	63
3.2 60 GHz Low Noise Local Oscillator Units (LNLOUs)	70
3.3 94 GHz Low Noise Local Oscillator Units (LNLOUs)	79
4.0 SYSTEM PERFORMANCE EVALUATION	87
4.1 System Function Block Diagram and Circuits	87
4.2 System Performance Characteristics	97
5.0 CONCLUSIONS	109
6.0 ACKNOWLEDGEMENTS	111
REFERENCES	113

Preceding Page BLANK -

# LIST OF ILLUSTRATIONS

<u>Figure</u>		<u>Page</u>
1-1	Photograph of the hardwares delivered to ECOM.	5
1-2	HP data generator, error detector and printer purchased for this program and delivered to ECOM.	6
2.1-1a	Design data for millimeter-wave double-drift IMPATT diode ( $T = 500^{\circ}\text{K}$ ).	8
2.1-1b	Design data for millimeter-wave single-drift diode ( $T = 500^{\circ}\text{K}$ ).	10
2.1-2a	60 GHz silicon single-drift IMPATT diode doping profile and field distribution (diode junction Temperation = $500^{\circ}\text{K}$ ).	11
2.1-2b	60 GHz silicon double-drift IMPATT diode doping profile and field distribution. (Junction Temperation = $500^{\circ}\text{K}$ ).	12
2.1-3a	94 GHz single-drift IMPATT diode doping profiles and field distribution (Diode Junction Tempera- tion = $500^{\circ}\text{K}$ ).	13
2.1-3b	94 GHz silicon double-drift IMPATT diode doping profile and field distribution.	14
2.1-4a	60 GHz silicon single-drift IMPATT diode admit- tance curve ( $T_j = 500^{\circ}\text{K}$ ).	15
2.1-4b	60 GHz silicon double-drift IMPATT diode admit- tance curve ( $T_j = 500^{\circ}\text{K}$ ).	16
2.1-5a	94 GHz single drift IMPATT diode admittance curve ( $T_j = 500^{\circ}\text{K}$ ).	17
2.1-5b	94 GHz silicon double-drift IMPATT diode admit- tance curve ( $T_j = 500^{\circ}\text{K}$ ).	18
2.1-6	Procedure for mounting IMPATT diodes on diamond heatsinks.	22
2.1-7a	Thermal resistance of double-drift silicon IMPATT diodes on diamond heatsinks.	23

# LIST OF ILLUSTRATIONS (CONTINUED)

<u>Figure</u>		<u>Page</u>
2.1-7b	Thermal resistance of single-drift silicon IMPATT diodes on copper heatsinks.	24
2.2-1	Coaxial coupled reduced height waveguide circuit.	26
2.2-2	Tuning characteristics of a silicon double-drift IMPATT oscillator as a function of the length of the coaxial section in which the diode was mounted.	27
2.2-3	Tuning characteristics of a double-drift IMPATT oscillator as the length in the RF choke section was varied.	28
2.2-4	Output power and dc to RF conversion efficiency of a silicon double-drift IMPATT diode oscillator in a coaxial-coupled reduced height waveguide circuit.	30
2.2-5	Bias current tuning characteristics of a 60 GHz oscillator using double-drift silicon IMPATT diode on copper heatsink. Diode breakdown voltage equals 23 volts, and diode capacitance equals 1.2 pf.	32
2.2-6	Bias current tuning characteristics of a 60 GHz oscillator using a double-drift IMPATT diode from the same diode lot as shown in Figure 2.2-5 but with a larger diode capacitance of 1.5 pf.	33
2.2-7	Bias current tuning characteristics of TO-V-A.	35
2.2-8	Bias current tuning characteristics of TO-V-B.	36
2.2-9	AM noise characteristics of TO-V-A.	39
2.2-10	AM noise characteristics of TO-V-B.	40
2.2-11	Frequency stability against ambient temperature variations of TO-V-A.	42
2.2-12	Frequency stability against ambient temperature variations of TO-V-B.	43
2.2-13	Picture of a 60 GHz FM IDTU.	44

# LIST OF ILLUSTRATIONS (CONTINUED)

<u>Figure</u>		<u>Page</u>
4.2-3	Spectral picture of the pair TO-W-A/LO-W-A, at 100 megabits/sec data rate with word normal pattern 1010 NRZ, and at S/N = 16 dB.	99
4.2-4	Spectral picture of the pair TO-W-A and LO-W-A at 200 megabits/sec data rate, 101010 word pattern NRZ, word normal 10 <sup>10</sup> -1, and S/N = 16 dB.	100
4.2-5	Spectral picture of the pair TO-W-A/LO-W-A at 100 megabits/sec data rate. Psuedo random binary sequence (PRBS normal) pattern of 10 <sup>10</sup> -1 word length was generated and detected.	101
4.2-6	BIT-ERROR-RATE of the pair TO-V-A/LO-V-A.	104
4.2-7	BIT-ERROR-RATE of the pair TO-V-B/LO-V-B.	105
4.2-8	BIT-ERROR-RATE of the pair TO-W-A/LO-W-A.	106
4.2-9	BIT-ERROR-RATE of the pair TO-W-B/LO-W-B.	107



## 1.0 INTRODUCTION AND SUMMARY

Millimeter waves have long been considered for adverse weather and secure communication applications especially at 94 GHz and 60 GHz respectively. The high frequencies also allow the use of small antennas, and provide wide bandwidth possible for high data rate communications. Recently, solid state devices such as oscillators, modulators, and mixers have been developed for millimeter wave applications, and, therefore, provide the potential of all solid-state compact systems. The purpose of this program are not only to advance the state-of-the-art of the solid state devices, especially, the IMPATT diode high power transmitter oscillators, and low noise local oscillators at these frequencies, but also to demonstrate the potential of these solid state devices for practical system applications.

The objectives of this research and development program are to develop high power IMPATT diode transmitter oscillators of 200 mW output power at 94 GHz frequencies and of 300 mW output power at 60 GHz frequencies; to develop low noise voltage-tuned IMPATT diode local oscillators at these frequencies; and to demonstrate the system performance capabilities of these solid state devices for transmitting and receiving FM FSK data at 100 megabits per second data rate with the bit-error-rate (BER) of less than  $10^{-7}$  at a signal-to-noise ratio of 15 dB or less. The development of these solid state devices can be applied to the future Army high data rate line-of-sight communications over a range of 2 Km at 60 GHz and of 5 Km at 94 GHz under heavy rainfall (20 mm/hr) conditions.

At these frequencies, the highest power possible, among all the solid state devices, is from silicon IMPATT diodes of  $p^+-p-n-n^+$  doping profile. The best results reported were all aimed at output power and efficiency, however, without taking into consideration the reasonable



tuning bandwidth for practical FM communications, and the reasonable diode junction temperatures (near  $250^{\circ}\text{C}$ ) for long term reliable applications.

GaAs Gunn oscillators were in general used as low noise local oscillators. Their noise is in general one order of magnitude lower than that of IMPATT devices. However, GaAs technology is not as well developed as Si technology, so that device reliability data were not available at these high frequencies for GaAs devices. This program demonstrated that low noise silicon IMPATT local oscillators using varactor diodes for frequency tuning (VTOs) can also be developed for FM data reception to achieve the program goals, at low diode junction temperatures to ensure long term ( $> 10^5$  hours) operation.

We have developed two 60 GHz and two 94 GHz FM IMPATT diode transmitter units (FM IDTUs) and two 60 GHz and two 94 GHz low noise local oscillator units (LN LOUs) during the course of this program to meet most of the program goals. Furthermore, for system performance evaluation using these oscillators, a FM receiver complete with balanced mixer, AFC, search/lock, AGC, and frequency discriminator/comparator circuits was also developed for 100 megabits/sec data reception and BER evaluation. Table 1.1 summarizes the expected program goals and the results we have achieved in this program.

FM noise of the two 60 GHz FM IDTUs and all the LN LOUs were not measured because of the limitations on delivery schedules and on the availability of calibrated setups for FM noise measurement. Similarly, the loaded Q of the oscillators, which relates directly to the oscillators FM noise and bias current tuning range has not been measured, although based on our experience, the Q-factors were in the order of 10 to 20 estimated. We also missed the data on the temperature stability of the two 94 GHz LN LOUs.

TABLE 1-1  
PROGRAM PERFORMANCE - EXPECTED AND MEASURED

Tasks	Expected	Measured	
		60 GHz	94 GHz
1. Transmitter Oscillators (FMIDTUs)			
Output Power	300 mW (60 GHz) 200 mW (94 GHz)	400 mW	275 mW
Frequency Deviation	±100 MHz	±150 MHz	±500 MHz
Efficiency	6%	5.5%	5.0%
Diode Junction Temperature	250°C	270°C	220°C
Stability	3 MHz/°C	4 MHz/°C	17 MHz/°C
AM Noise, Double-Sideband	-130 dBc/100 Hz	-132 dBc/100 Hz	-138 dBc/100 Hz
FM Noise (Bandwidth 100 Hz)	10 <sup>-9</sup>	--	10 <sup>-8</sup>
Loaded Q	100	--	--
Index of Modulation	2	2	2
Data Rate	10 <sup>8</sup> Bits/Sec	2.0 x 10 <sup>8</sup> Bits/Sec	2.0 x 10 <sup>8</sup> Bits/Sec
2. Local Oscillators (LNLOUs)			
Output Power	60 mW	63 mW	46 mW
Tuning Range	4 GHz	3 GHz	1 GHz
Stability	3 MHz/°C	10 MHz/°C	--
AM Noise, Double-Sideband	-130 dBc/100 Hz	-137 dBc/100 Hz	-133 dBc/100 Hz
FM Noise (Bandwidth 100 Hz)	10 <sup>-9</sup>	--	--
3. System Evaluation			
I.F. Bandwidth (centered at 1.50 GHz)	1 GHz	0.5 GHz	0.5 GHz
Index of Modulation	2	2	2
Receiver Noise Figure	9 dB	10 dB	10 dB
Search/Lock Time	0.01 Sec	0.01 Sec	0.01 Sec
AFC	Provided	Provided	Provided
AGC	Not specified	Provided	Provided
Bit-Error at Signal/Noise = 15 dB	10 <sup>-7</sup>	4 x 10 <sup>-9</sup>	7 x 10 <sup>-9</sup>
Data Rate	10 <sup>8</sup> Bits/Sec	2 x 10 <sup>8</sup> Bits/Sec	2 x 10 <sup>8</sup> Bits/Sec

The two FM IDTUs at 60 GHz and two FM IDTUs at 94 GHz have been delivered to ECOM for evaluation. The units were mounted on heatsinks with current regulator/modulator circuits and ferrite isolators mounted as integral parts of the transmitter oscillators. The two LN LOUs at 60 GHz and two LN LOUs at 94 GHz have also been delivered to ECOM. The units were also mounted on heatsinks with current regular circuit, varactor bias leads, and ferrite isolators as integral parts of the local oscillators.

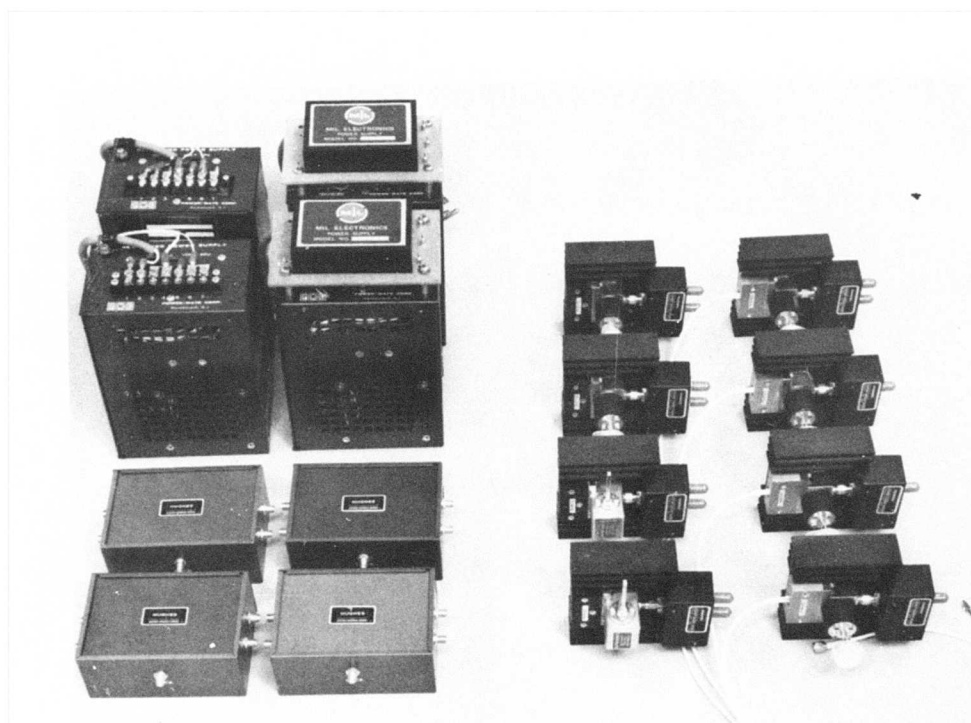
Four search/lock boxes have been constructed and delivered to ECOM for use with the four LN LOUs.

Figure 1-1 shows the picture of the FM IDTUs and LN LOUs and the S/L boxes with part of the power supplies delivered to ECOM.

For BER evaluation, a HP3760A data generator with option 012 and a HP3761A error detector with option 002, and a HP 5055 printer as shown in Figure 1-2 have also been delivered to ECOM.

In this report, we will first discuss silicon double-drift IMPATT diode FM transmitter oscillators development in Section 2.0. Then the low noise local oscillators development will be discussed in Section 3.0. System performance evaluation of those oscillators will be covered in Section 4.0. The discussions on the results achieved and future development work suggested will be concluded in Section 5.0.

E1173



0 1 2 3 4 5 6

Figure 1-1 Photograph of the hardware delivered to ECOM.



Figure 1-2 HP data generator, error detector and printer purchased for this program and delivered to ECOM.

## 2.0 FM IMPATT DIODE TRANSMITTER OSCILLATOR DEVELOPMENT

### 2.1 IMPATT DIODE DESIGN

#### DIODE PROFILE

The silicon double-drift IMPATT diode of  $p^+pnn^+$  doping profile is essentially two complementary single-drift IMPATT diodes ( $p^+nn^+$ , and  $p^+pn^+$ ) in series.<sup>1</sup> From the physics point of view, the negative resistance of a double-drift diode on a per unit area basis is therefore twice of that of a single-drift diode. Since the effective area of a double-drift diode is about half that of a single-drift diode, we expect four times more output power from a double-drift diode than from a single-drift of the same physical area. The efficiency of the double-drift diode is also better than the single-drift diode. This is because only one avalanche region is required for both drift regions. Since the avalanche region and drift region voltage are essentially equal, the total dc voltage of a double-drift diode is about 50% higher than a single-drift diode. Since the output power is about four times that of the single-drift diode, we expect an improvement in efficiency by about two to three times with the double-drift diode.

Theoretical design of silicon double-drift diodes doping profiles for optimum power and efficiency has been reported using large signal computer simulation.<sup>2</sup> The results are reproduced in Figure 2.1-la. The difference in both doping concentration,  $N_a$  and  $N_d$ , and in region thickness,  $X_p$  and  $X_n$ , shown in Figure 2.1-la is due to the difference in low-field mobilities, ionization rates, and saturation velocities between electrons and holes. For realistic double-drift diode design, however, one should take into consideration that for millimeter wave diodes at 60 and 94 GHz, the carrier diffusion lengths are significant compared with the thin n and p layer thickness which are in the order of

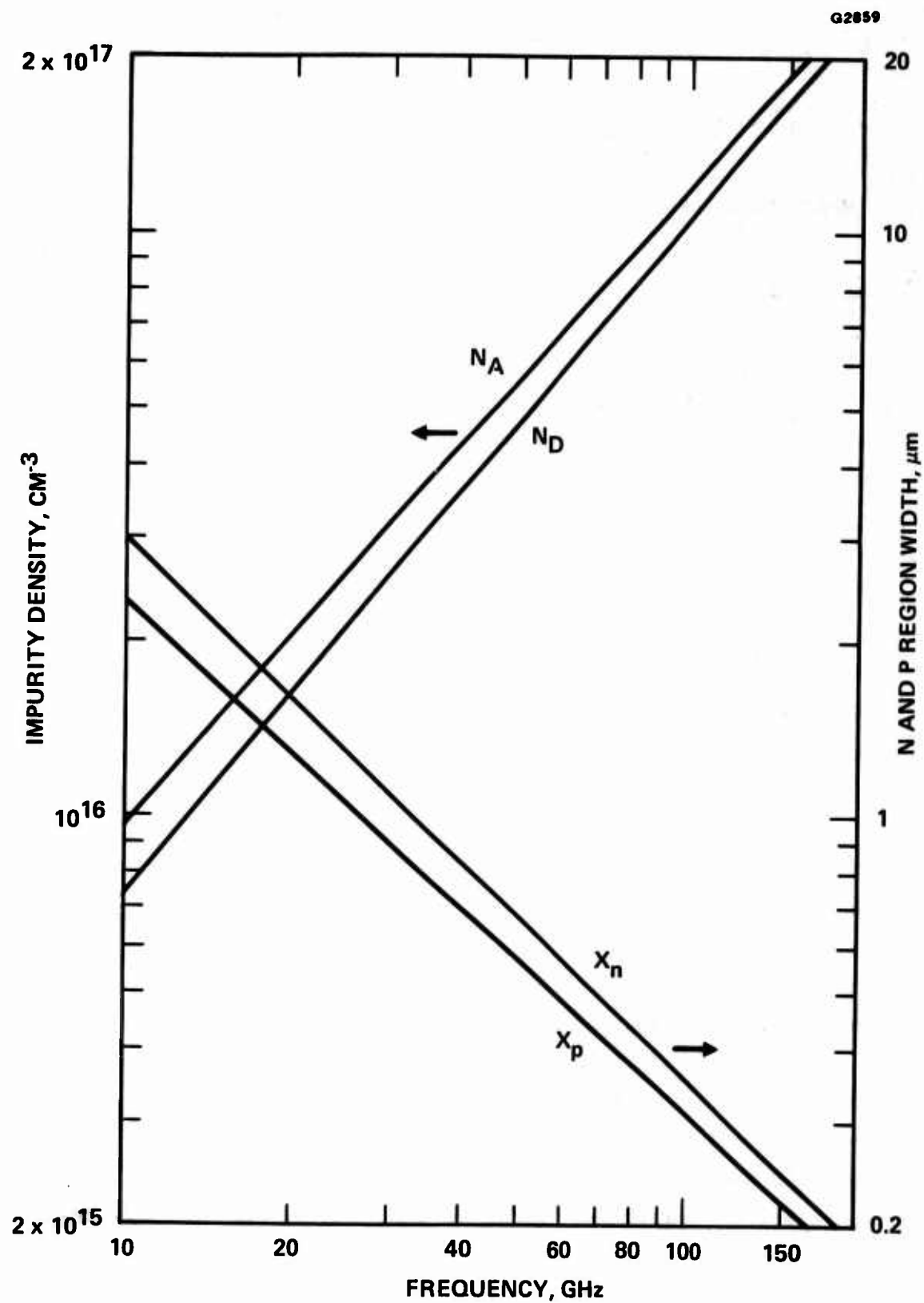


Figure 2.1-1a Design data for millimeter-wave double-drift IMPATT diode ( $T = 500^\circ\text{K}$ ).

$0.3 \times 10^{-4}$  cm to  $0.5 \times 10^{-4}$  cm. Not only is it difficult to control the layer thicknesses to the designed values, but also to realize flat doping profiles in both regions. Furthermore, there is always the out-diffusion from the  $n^+$  substrate material to further complicate the doping profile and lower the diode power and efficiency. For comparison, single-drift IMPATT diode design curve is shown in Figure 2.1-1b.

We have fabricated diodes of different doping profiles at 60 and 94 GHz. Multiple-epitaxial vapor layer growth technique was used to grow the n and p layers instead of the ion-implantation technique. We have found that the multiple-epitaxial growth technique is suitable for large quantity production. For the 60 GHz diodes, because of larger layer thicknesses than those of the 94 GHz diodes, attempts were made to follow the optimum computer design. For the 94 GHz diodes, it is more difficult to control the doping concentration and thickness so that equal n and p layer concentrations were targeted. Figure 2.1-2a and 2.1-2b are the doping profiles and calculated electric field for the 60 GHz single-drift and double-drift diodes respectively. The 94 GHz single-drift and double-drift diodes doping profiles and electric fields are shown respectively in Figure 2.1-3a and 2.1-3b. Small signal calculations of the diode admittances at 500°K diode junction temperature for the 60 GHz single-drift and double-drift diodes are shown in Figure 2.1-4a and 2.1-4b respectively. The design shows the operating frequencies and current densities that are expected for operation at these frequencies. Similarly, for the 94 GHz single-drift and double-drift diodes, the diode admittance curves are plotted in Figure 2.1-5a and 2.1-5b respectively.

Power output capabilities of the double-drift diodes compared with the single-drift diodes, however, cannot be determined by the admittance curves alone. From the circuit point of view they are also related to the r.f. voltage across the diode terminals and to the area of the diodes.



G4211

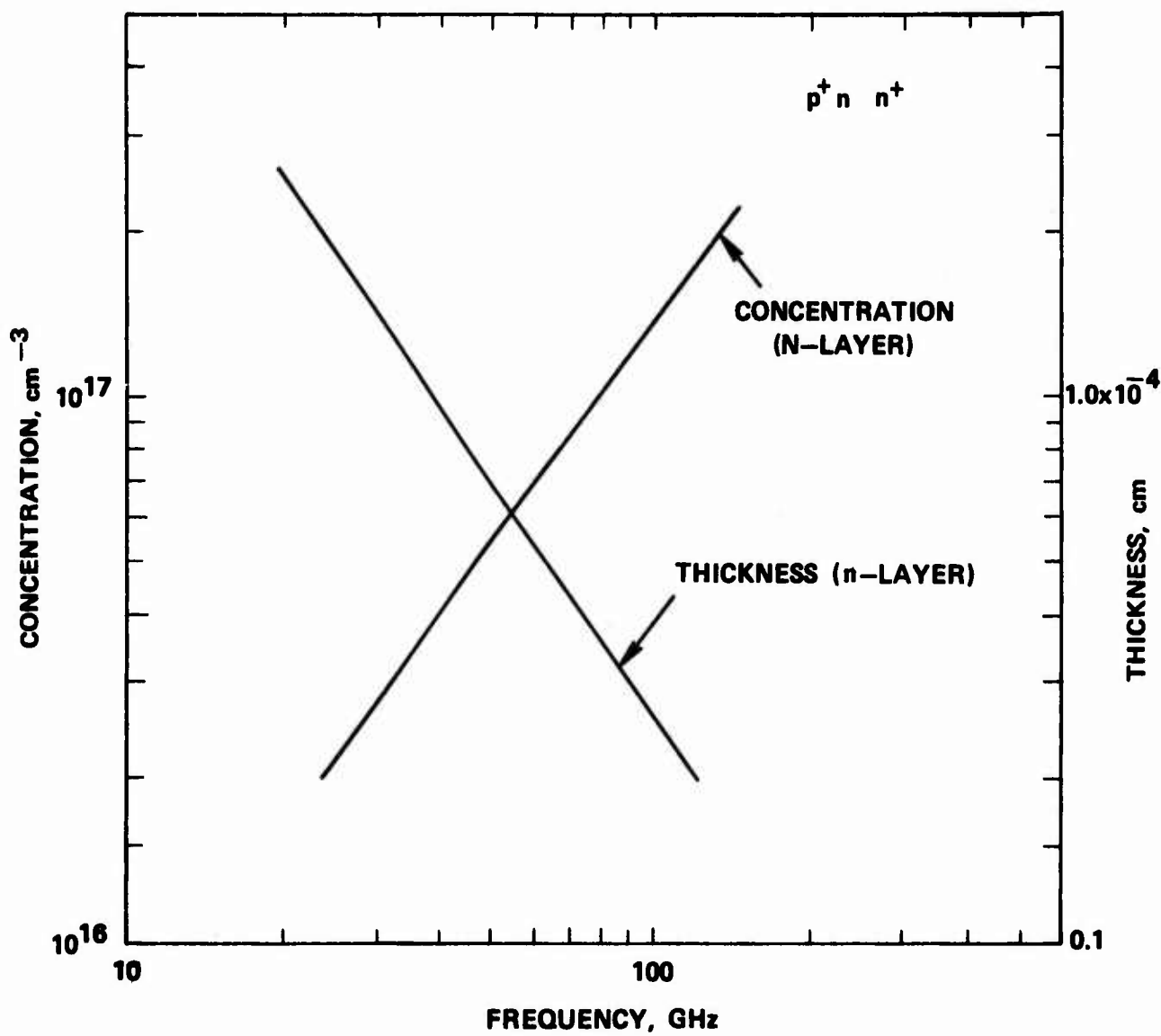


Figure 2.1-1b Design data for millimeter-wave single-drift diode ( $T = 500^\circ\text{K}$ ).

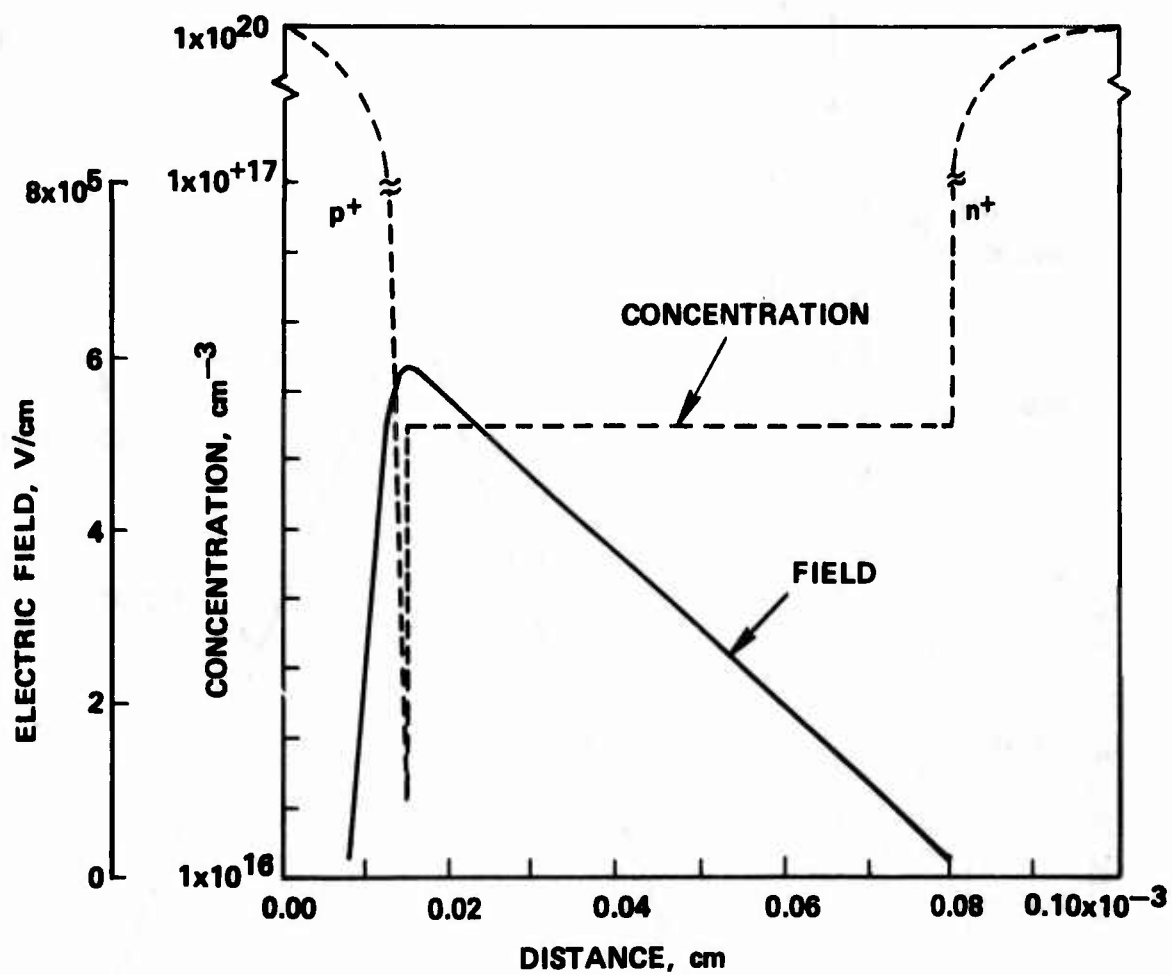


Figure 2.1-2a 60 GHz silicon single-drift IMPATT diode doping profile and field distribution (diode Junction Temperature =  $500^\circ\text{K}$ ).

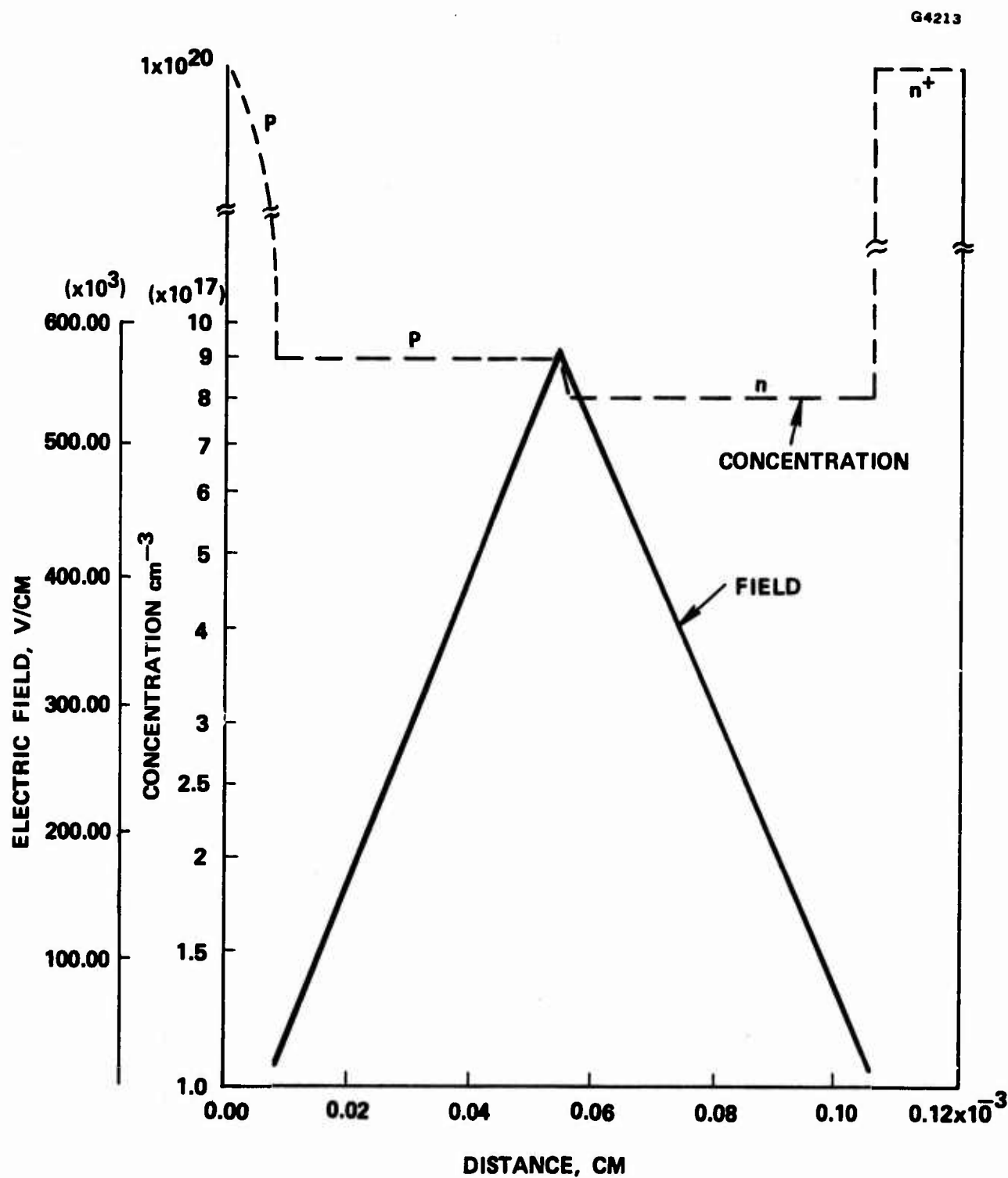


Figure 2.1-2b 60 GHz silicon double-drift IMPATT diode doping profile and field distribution. (Junction Temperature =  $500^{\circ}\text{K}$ )

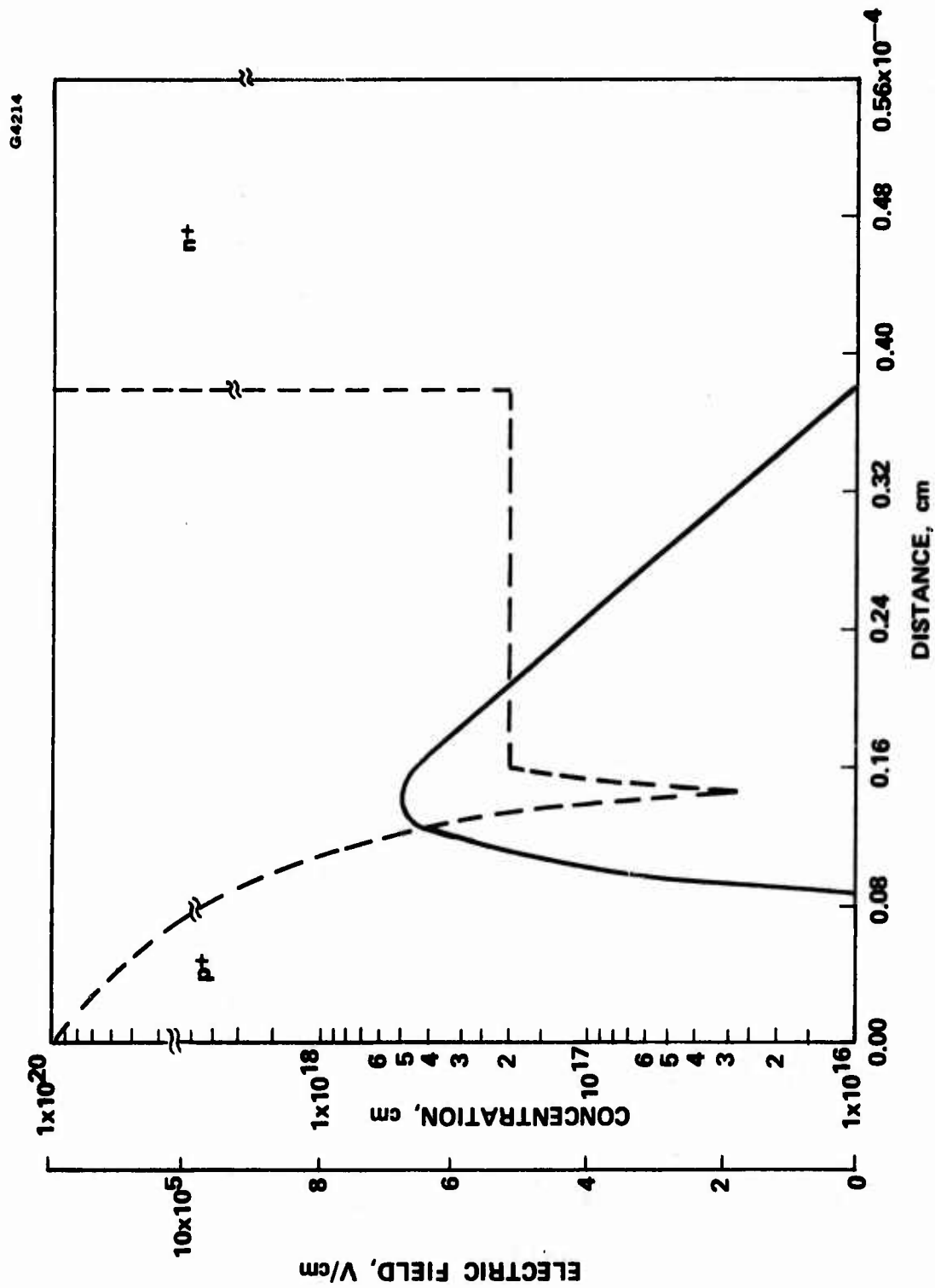


Figure 2.1-3a 94 GHz single-drift IMPATT diode doping profiles and field distribution (Diode Junction Temperature = 500°K).

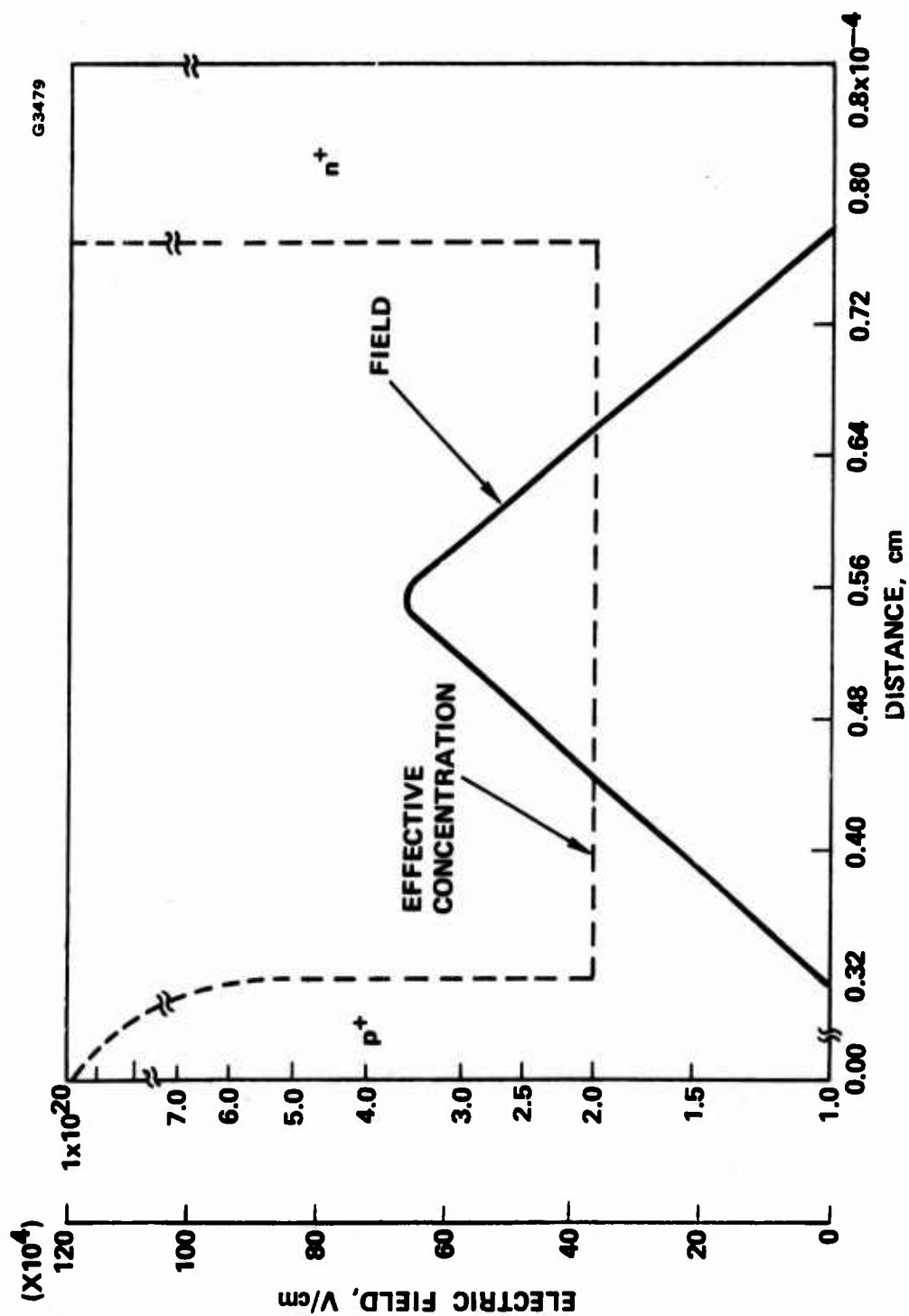


Figure 2.1-3b 94 GHz silicon double-drift IMPATT diode doping profile and field distribution.

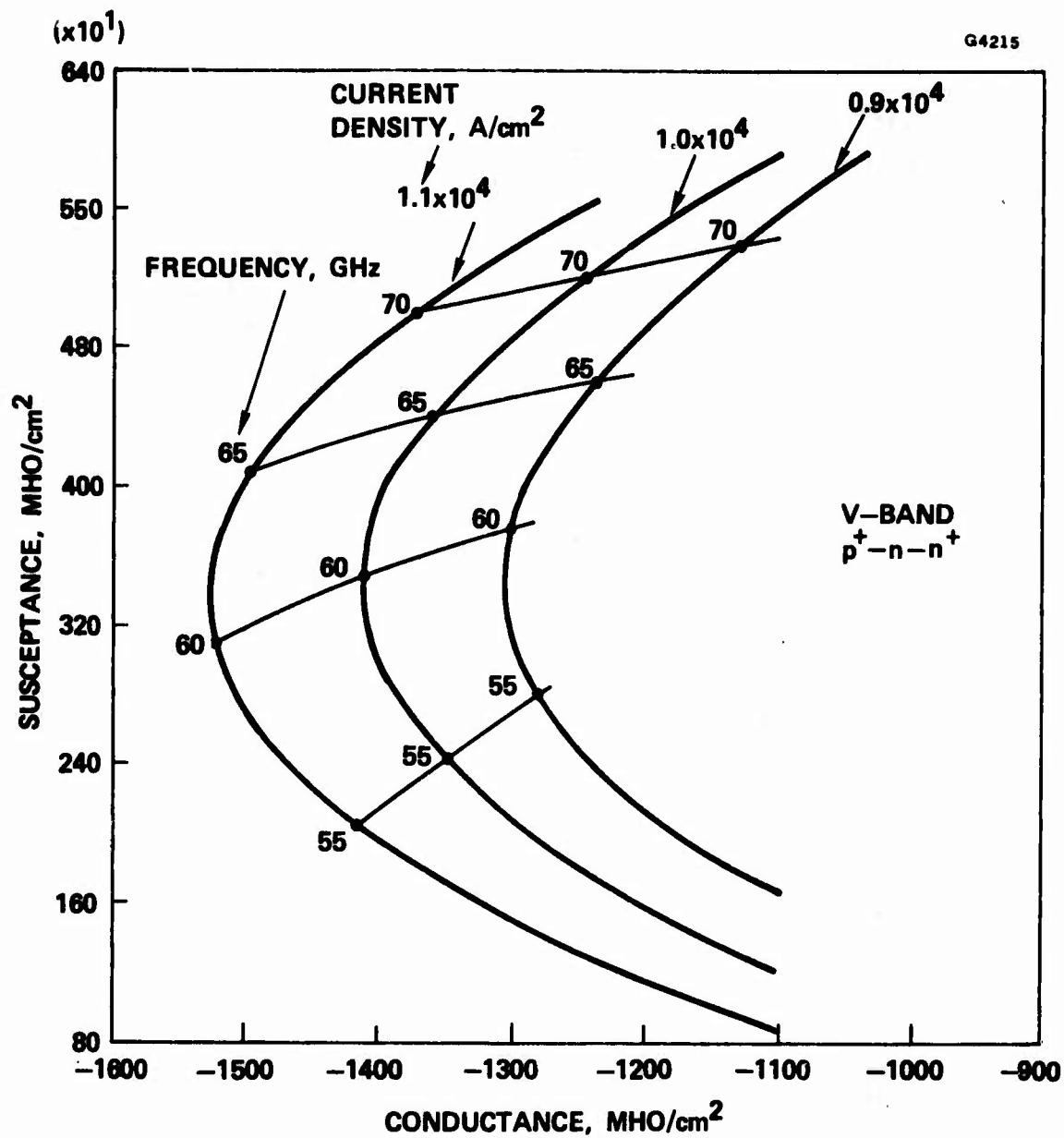


Figure 2.1-4a 60 GHz silicon single-drift IMPATT diode admittance curve ( $T_j = 500^\circ\text{K}$ ).

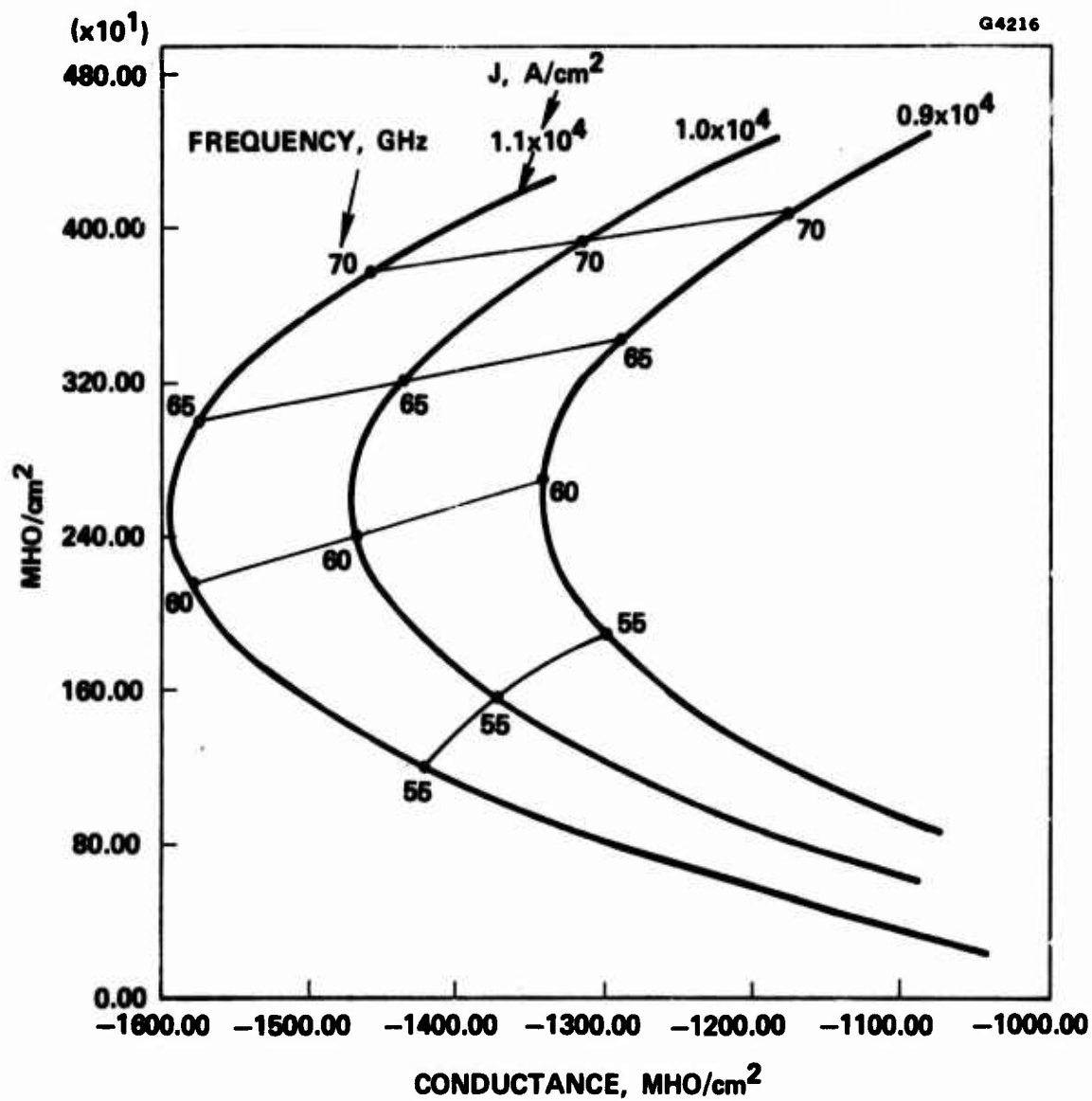


Figure 2.1-4b 60 GHz silicon double-drift IMPATT diode admittance curve ( $T_j = 500^\circ\text{K}$ ).

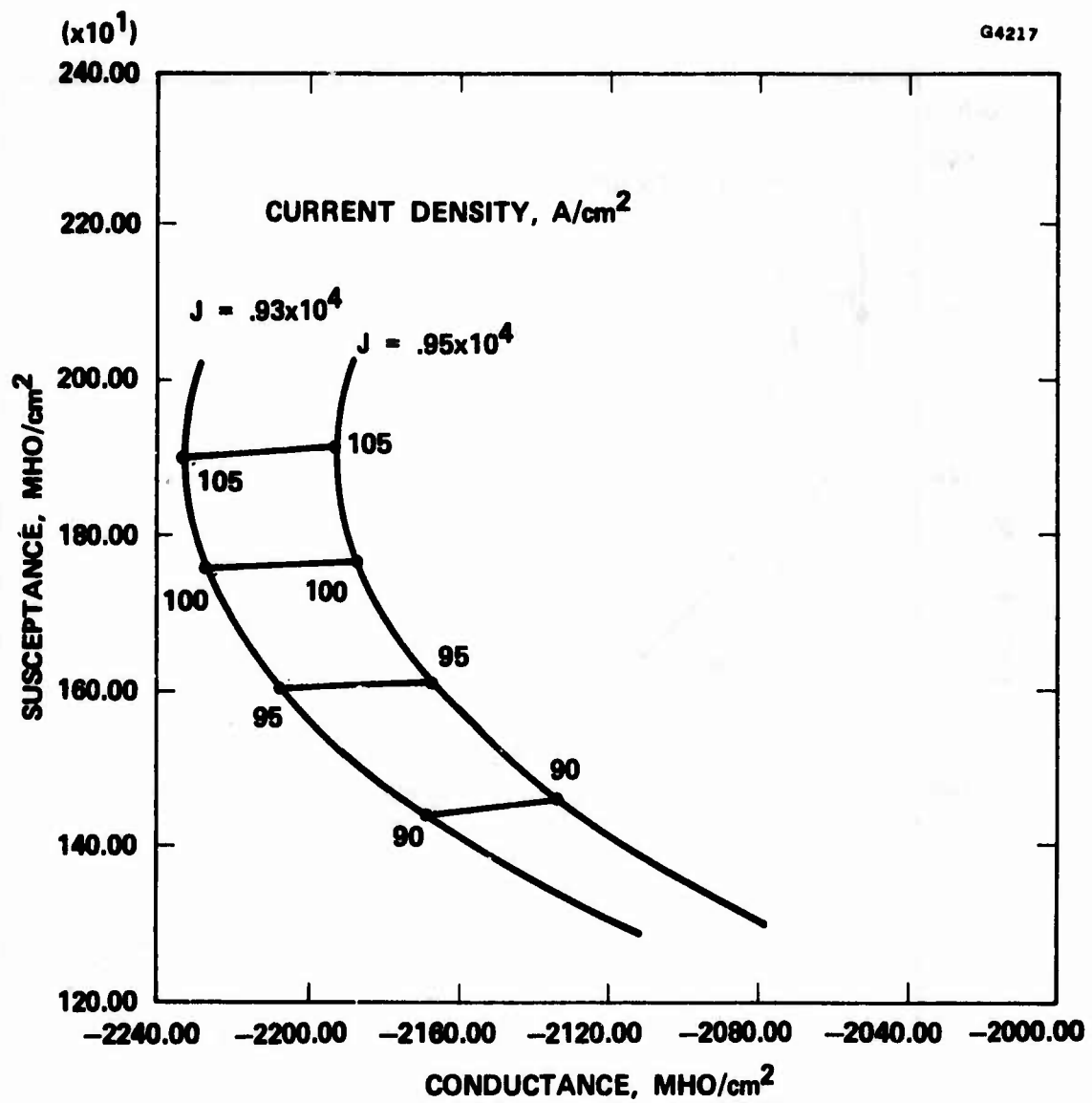


Figure 2.1-5a 94 GHz single drift IMPATT diode admittance curve ( $T_j = 500^\circ\text{K}$ ).



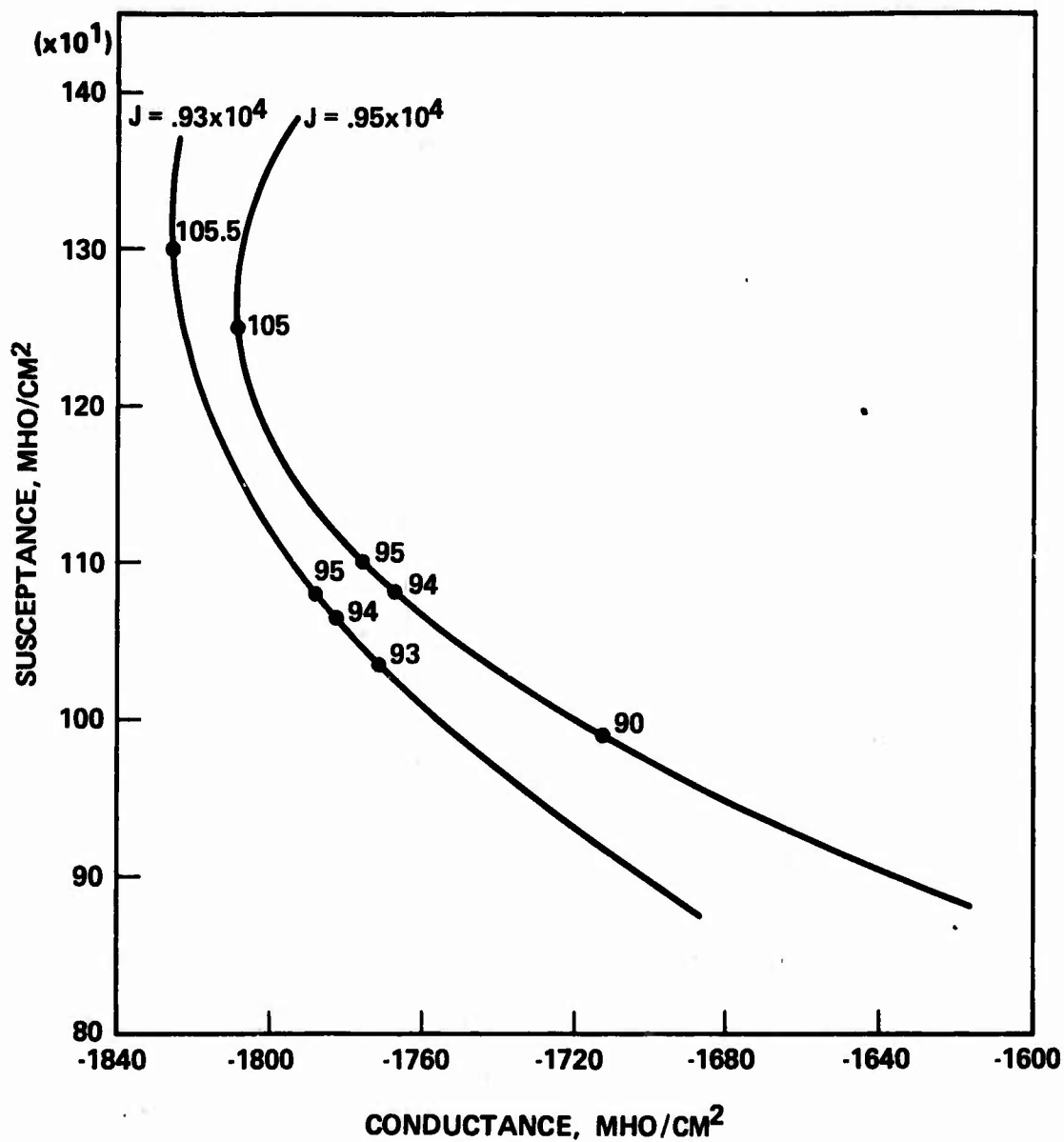


Figure 2.1-5b 94 GHz silicon double-drift IMPATT diode admittance curve. ( $T_j = 500^\circ\text{K}$ )

For the double-drift diodes, the breakdown voltage is about 1.4 times higher than that of the single-drift diodes of same effective doping concentration. Therefore, the r.f. voltage for the double-drift diodes is expected to be higher than that of the single-drift diodes by a factor of 1.4. This alone allows us to expect the double-drift diodes to have at least  $(1.4)^2$  times more output power capability than the single-drift diodes assuming same negative conductance values (in mhos). However, the single-drift diodes normally have more susceptance per unit area than the double-drift diodes. To match the same external circuit impedance, the diode area of the double-drift diodes must be increased to reach the same susceptance levels as the single-drift diodes. This also increases the negative conductance of the double-drift diodes. Depending on the diode design, we normally expect to have a power increase with the double-drift diodes in the order of 2 to 4 times over the single-drift diodes.

The output power and frequency of IMPATT oscillators are limited electronically and/or thermally.<sup>3</sup> For high frequency diodes, the maximum power capability,  $P_m$ , of the IMPATT diodes is limited by the breakdown voltage and maximum current, which in turn is limited by the avalanche breakdown process. A relationship between  $P_m$  and the frequency  $f$ ,

$$P_m \propto \frac{1}{f^2}$$

is predicted and is normally observed for frequencies higher than 100 GHz. At lower frequencies, the diode breakdown voltages are normally large, so that maximum power is limited by the thermal

resistance between the diode junction and the diode heatsink. The relationship

$$P_m \cdot f = \left( \frac{\Delta T}{R_T} \right) f \sim \frac{\sigma_s \Delta T}{\epsilon_s} = \text{Constant}$$

is normally observed. Here  $\Delta T$  is the junction temperature rise above the ambient,  $\sigma_s$  is the silicon thermal conductivity, and  $\epsilon_s$  is the silicon dielectric constant. For double-drift diodes, diode breakdown voltage is about 1.4 times higher than that of the single-drift diodes. We therefore expect that the thermal limitation will be the dominant effect, and this is generally observed in our laboratory.

To achieve the maximum power possible at 60 and 94 GHz, it is obvious that low thermal resistance must be required. We have initiated the work using type IIa diamond as heatsink to lower the thermal resistance for the 94 GHz diodes to achieve sufficient transmitter output power at low diode junction temperatures required for this program. For the 60 GHz diodes, since sufficient output power at low diode junction temperatures can be achieved using copper heatsinks, no attempts were made to use diamond heatsinks for this program.

#### DIAMOND HEATSINKS

The thermal resistance between the diode junction and the heatsink consists of a diode diffusion resistance in the silicon in series with a spreading resistance at the diode and heatsink interface region.<sup>4</sup> The diffusion resistance is normally about ten times smaller than the spreading resistance using copper as heatsinks. However, since type IIa diamond has a thermal conductivity of 12.0 W/cm-°K compared with that of copper, 3.94 W/cm-°K, the theoretical calculation<sup>4</sup> shows that one can

expect to achieve a 50% reduction of the overall thermal resistance by using diamond heatsinks.

Figure 2.1-6 shows the procedure for mounting double-drift IMPATT diodes on diamond heatsinks. Thermal resistance of double-drift diodes on diamond has been measured using combined d.c. and pulsed methods.<sup>5,6,7</sup> Figure 2.1-7a is the measured thermal resistance as a function of the diode capacitance for double-drift IMPATT diodes on type IIa diamond heatsinks for diodes with breakdown voltages of 18.5 volts and 23.5 volts. Thermal resistances of double-drift diodes on copper heatsinks with 23.5 volts breakdown voltage are also shown in Figure 2.1-7a for comparison. In general, we achieved a 1/3 reduction in thermal resistance with the use of diamond heatsinks. Measured thermal resistances of single-drift silicon IMPATT diodes on copper heatsinks are also recorded and shown in Figure 2.1-7b as a comparison with the double-drift IMPATT diodes results.

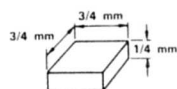
## 2.2 60 GHz FM OSCILLATORS

### 2.2.1 60 GHz IMPATT Oscillator Circuit

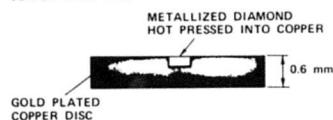
IMPATT diode oscillations occur when the external circuit impedance matches with the diode RF impedance. Normally, a simple reduced height waveguide circuit is sufficient to achieve device-circuit impedance matching when a  $p^+-n-n^+$  single-drift IMPATT diode is used. Wideband bias current tuned oscillations covering almost full waveguide frequency band or high power narrow tuned oscillators can be achieved using single-drift IMPATT diodes with relatively little effort. However, with double-drift IMPATT diodes, since the device admittance curves are compressed toward the negative conductance axis of the device admittance plot, the present simple reduced height waveguide circuit was not able to achieve good device-circuit impedance matching for

## DIAMOND HEAT SINKS

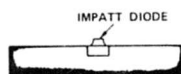
## 1. TYPE IIA DIAMOND



## 2. METALLIZE (Cr-Pt-Au) DIAMOND IMBEDDED IN GOLD PLATED COPPER HEAT SINK



## 3. T. C. BOND IMPATT DIODE ON DIAMOND



## 4. SOLDER QUARTZ RING AND RIBBON BOND (CAPPING NOT SHOWN)



## 5. SOLDER COPPER DISC ON HEAT SINK

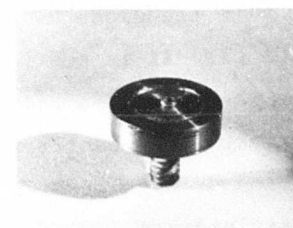
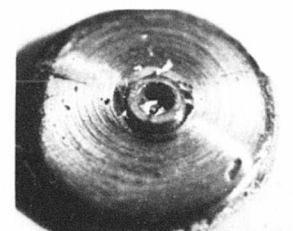
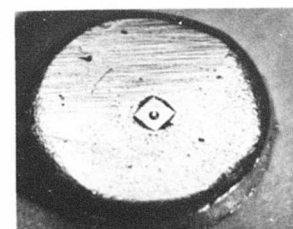
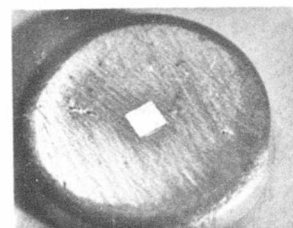
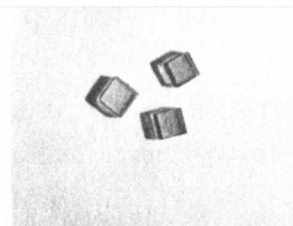
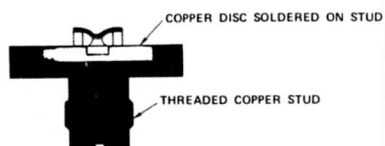


Figure 2.1-6 Procedure for mounting IMPATT diodes on diamond heatsinks.

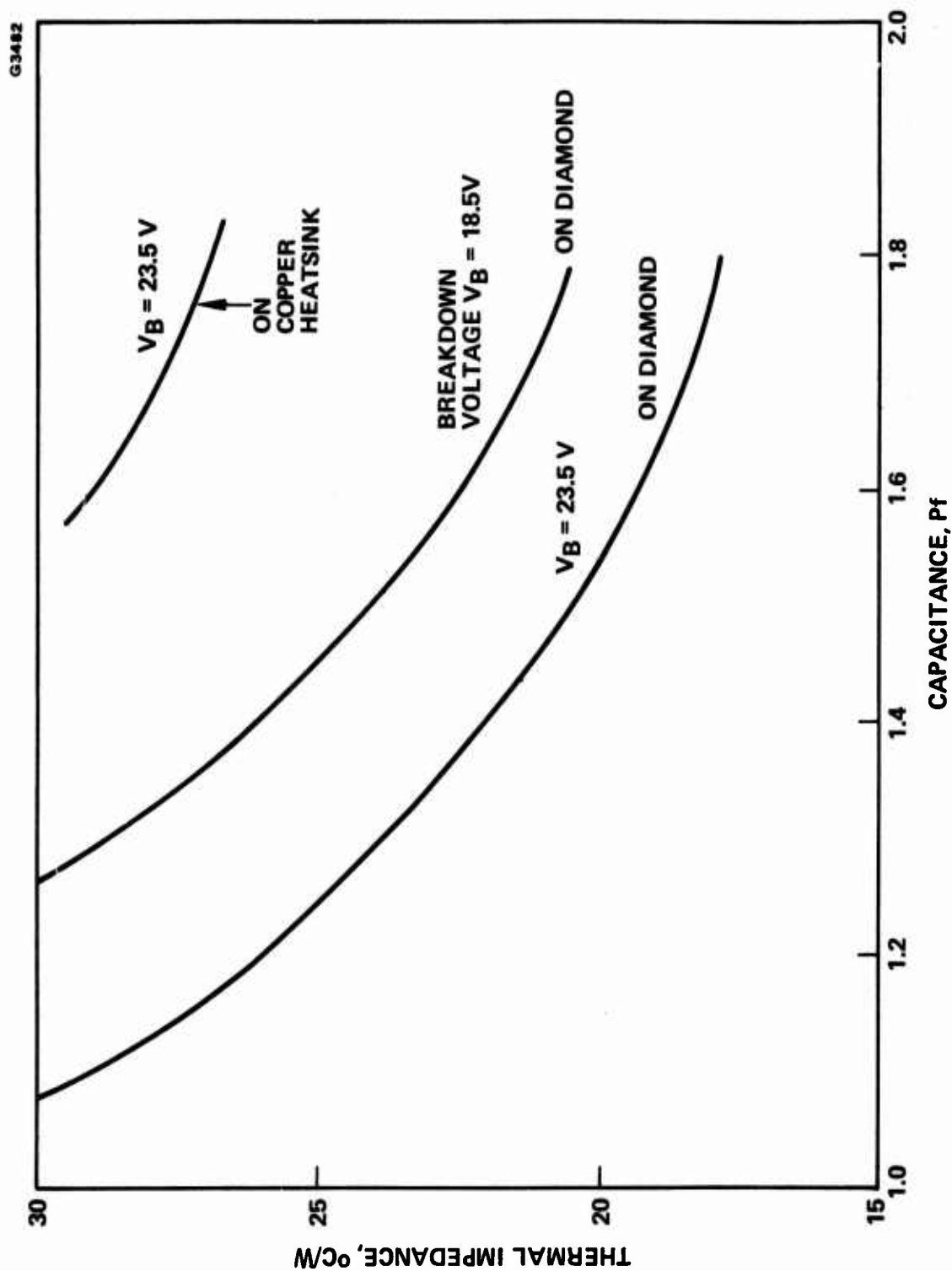


Figure 2.1-7a Thermal resistance of double-drift silicon IMPATT diodes on diamond heatsinks.

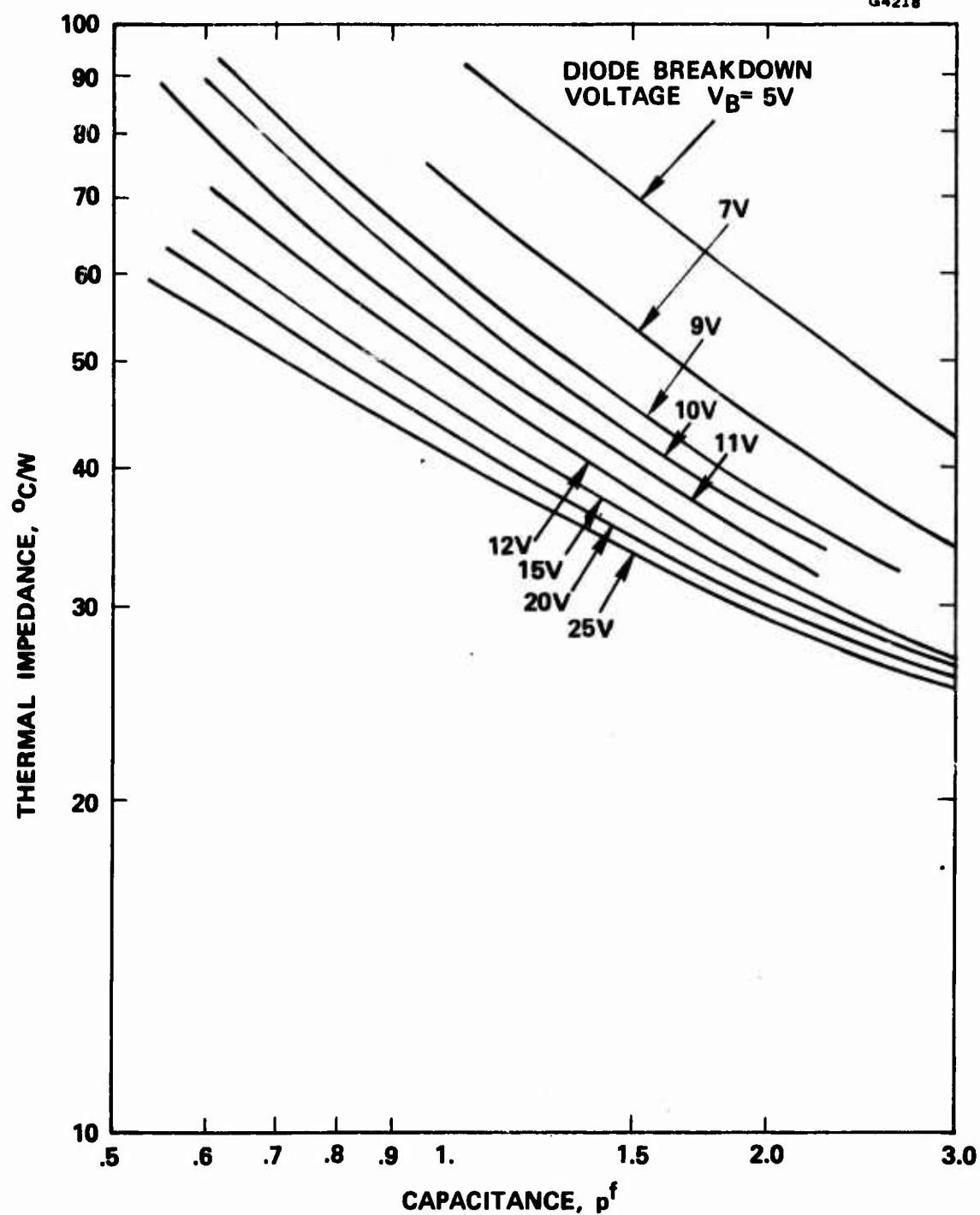


Figure 2.1-7b Thermal resistance of single-drift silicon IMPATT diodes on copper heatsinks.

high power, high efficiency oscillation with good RF tuning characteristics. Therefore, various cavity circuits have been investigated. Some degree of success has been achieved, in terms of oscillator output power and efficiency, with the coaxial coupled reduced height waveguide circuit shown in Figure 2.2-1. A packaged double-drift IMPATT diode is mounted at the end of a coaxial section which is cross-coupled to the reduced height waveguide section. The bias to the diode is by a metal pin through an anodized aluminum dc bypass as shown in the figure. A contacting sliding short is provided behind the bias pin which also serves as a coupling post between the coaxial section (where the diode is mounted) and the reduced height waveguide section. The sliding short is generally placed approximately one half of a guided wavelength behind the coupling post to achieve a low impedance across the post. However, the impedance level can be tuned mechanically by moving the sliding short. The length  $L$  of the coaxial section where the diode is mounted can be varied in steps using spacers from zero length (simple reduced height waveguide circuit) to as much as a quarter wavelength to provide impedance transformation from the low diode impedance to the high waveguide impedance. The coaxial section formed by the anodized aluminum dc bypass (RF choke) and the bias pin can also be used for impedance matching by moving the position of the RF choke along the bias pin to vary the distance as indicated in the figure.

Figure 2.2-2 shows the tuning characteristics of a double-drift IMPATT oscillator as a function of the length of the coaxial section in which the diode is mounted. Best power is achieved when the diode is mounted about 0.040 inch recessed from the reduced height waveguide section and with  $a = 0$ . This indicates that certain impedance transformations can be provided with a short section of coaxial length in the RF choke section as discussed earlier and shown in Figure 2.2-3. The diode is mounted in a coaxial recess  $L$  of about 0.040 inch in length. The data is obtained with the diode biased at junction temperature



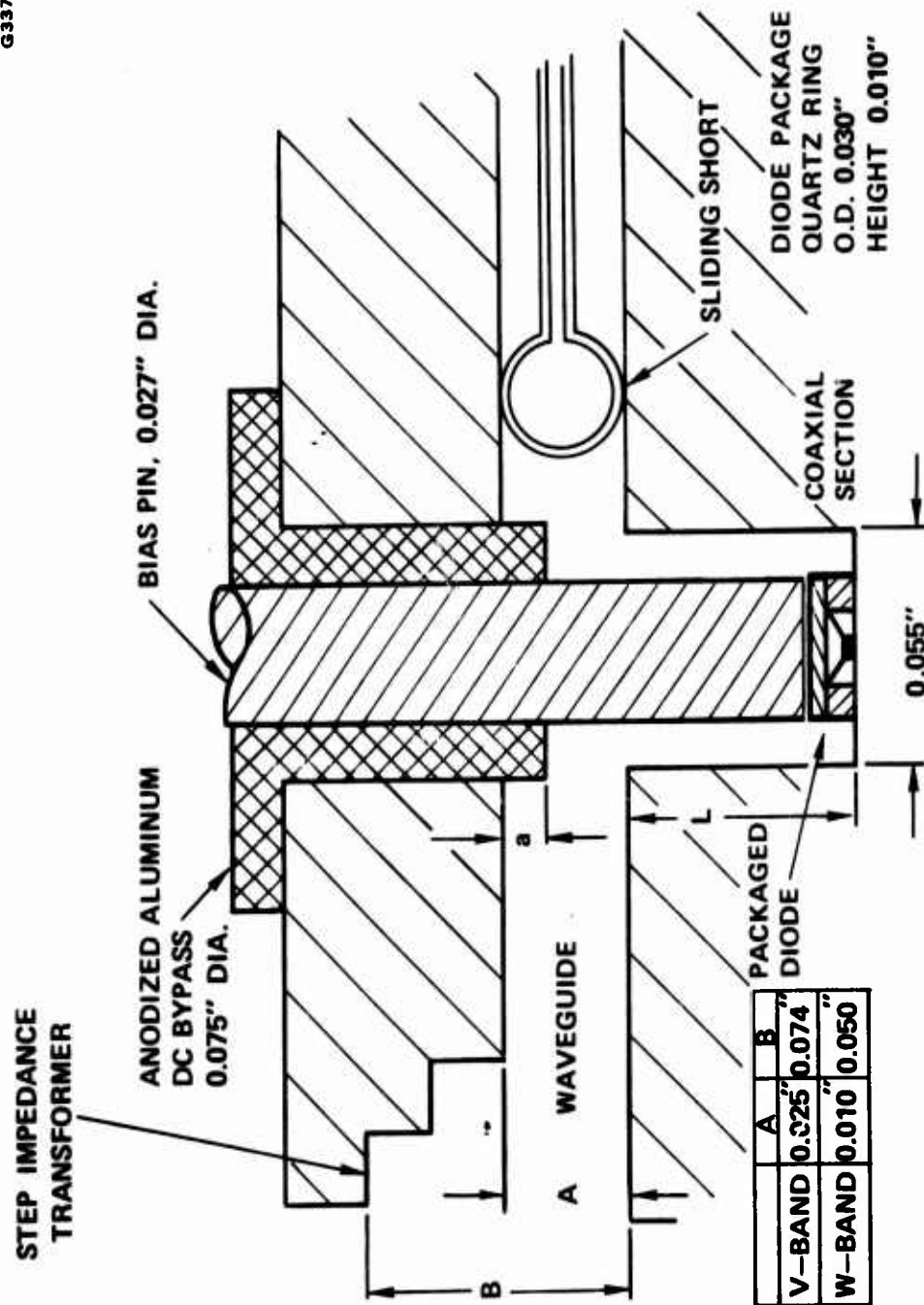


Figure 2.2-1 Coaxial coupled reduced height waveguide circuit.

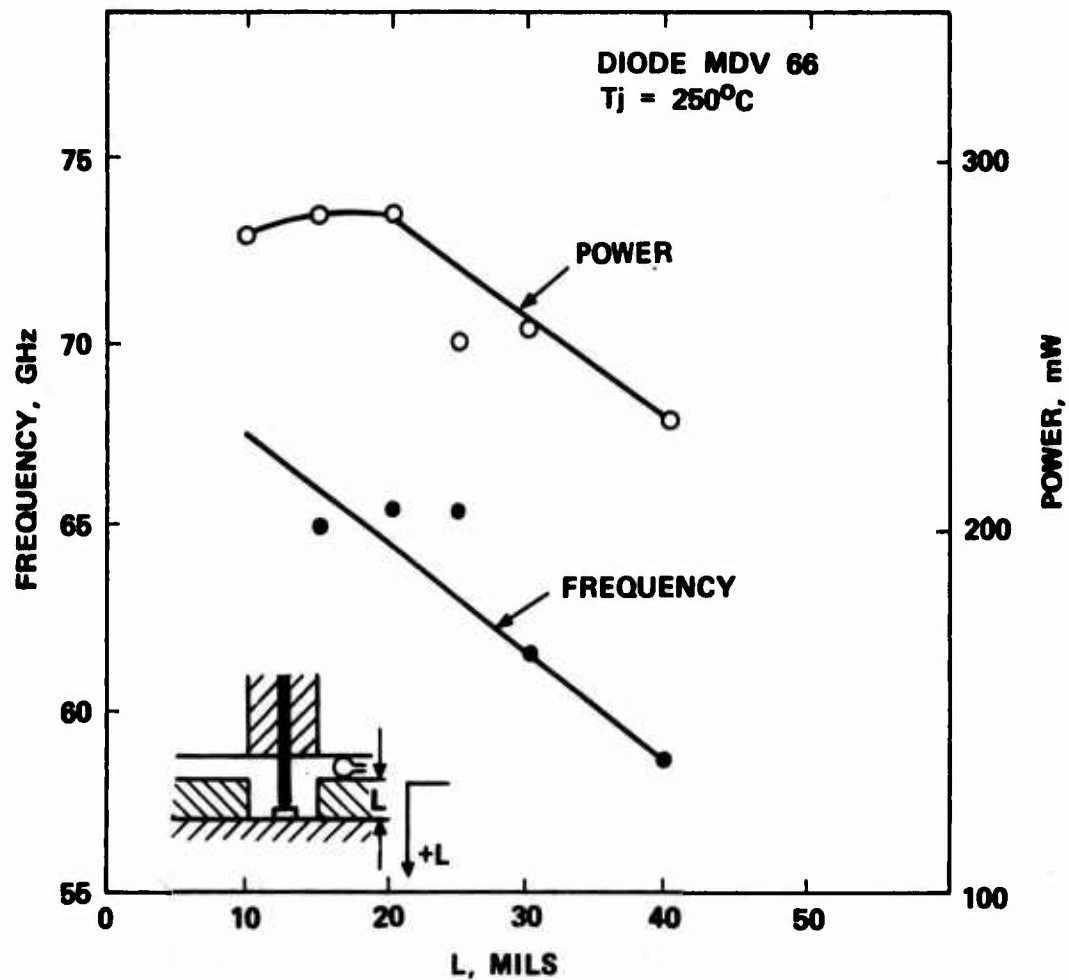


Figure 2.2-2 Tuning characteristics of a silicon double-drift IMPATT oscillator as a function of the length of the coaxial section in which the diode was mounted.

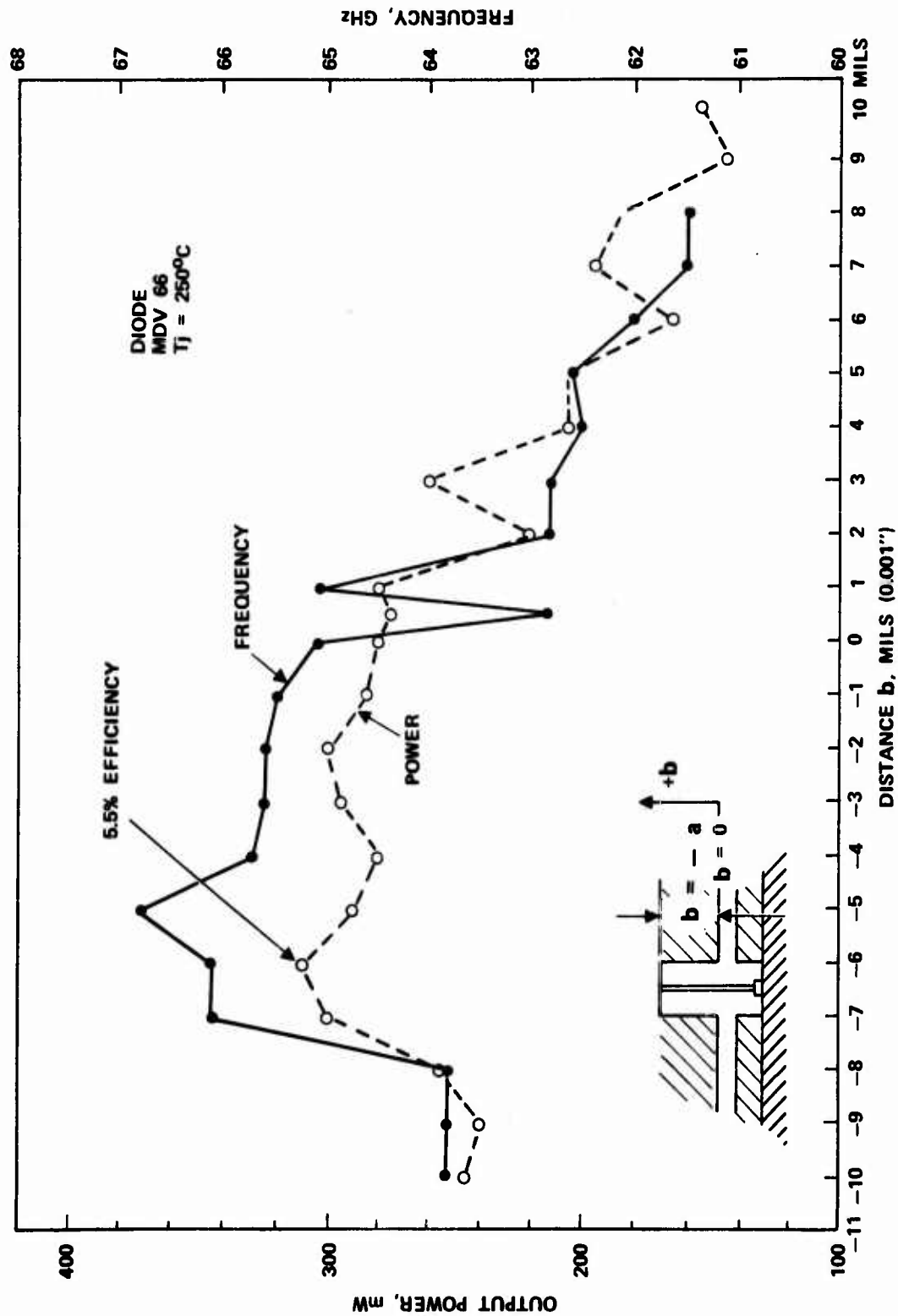


Figure 2.2-3 Tuning characteristics of a double-drift IMPATT oscillator as the length in the RF choke section was varied.

of 250°C which is determined from the total dc power input to the diode multiplied by the measured thermal impedance (°C/watts) between the junction of the diode and the diode heat sink at ambient temperature. Best output power and dc to RF conversion efficiency was achieved when the RF choke (the anodized aluminum dc bypass) was actually inserted into the reduced height waveguide section. Output power of 310 mW at 5.5% efficiency was obtained at approximately 66 GHz. Both power and frequency were reduced as the choke was recessed into its coaxial section. This circuit is reasonably effective in achieving device-circuit impedance matching over a given mechanical tuning range. However, frequency tuning range with bias current at fixed mechanical tuning is in general narrow. We have found it is difficult to achieve bias current tuning range at both 60 GHz and 94 GHz frequencies. Nevertheless, we have achieved bias current tuning range over 100 MHz at both 60 GHz and 94 GHz frequencies by selecting the diodes to match the circuit impedance. Figure 2.2-4 is the result of the best efficiency and output power we have achieved with this circuit. At a low diode junction temperature of 250°C, 8.6% efficiency and 480 mW output power at 58.15 GHz have been obtained, with diodes on copper heatsinks.

This result compares closely with the best reported result of about 600 mW output power and about 11% efficiency at 250°C diode junction temperature at 50 GHz for a silicon p+p nn+ IMPATT diode on metal heatsink.<sup>8</sup>

Recently, output power of 1 watt and 11% efficiency with a p+pnn+ silicon IMPATT diode on diamond heatsink operated at 250°C junction temperature and 50 GHz was reported.<sup>9</sup> Our diode performance can therefore be further improved by using diamond heatsinks so that the output power will not be thermally limited. Recently, the performance of our 60 GHz diodes on diamond heatsinks have been reported.<sup>10</sup> For example, 605 mW output power at 231°C diode junction temperature has

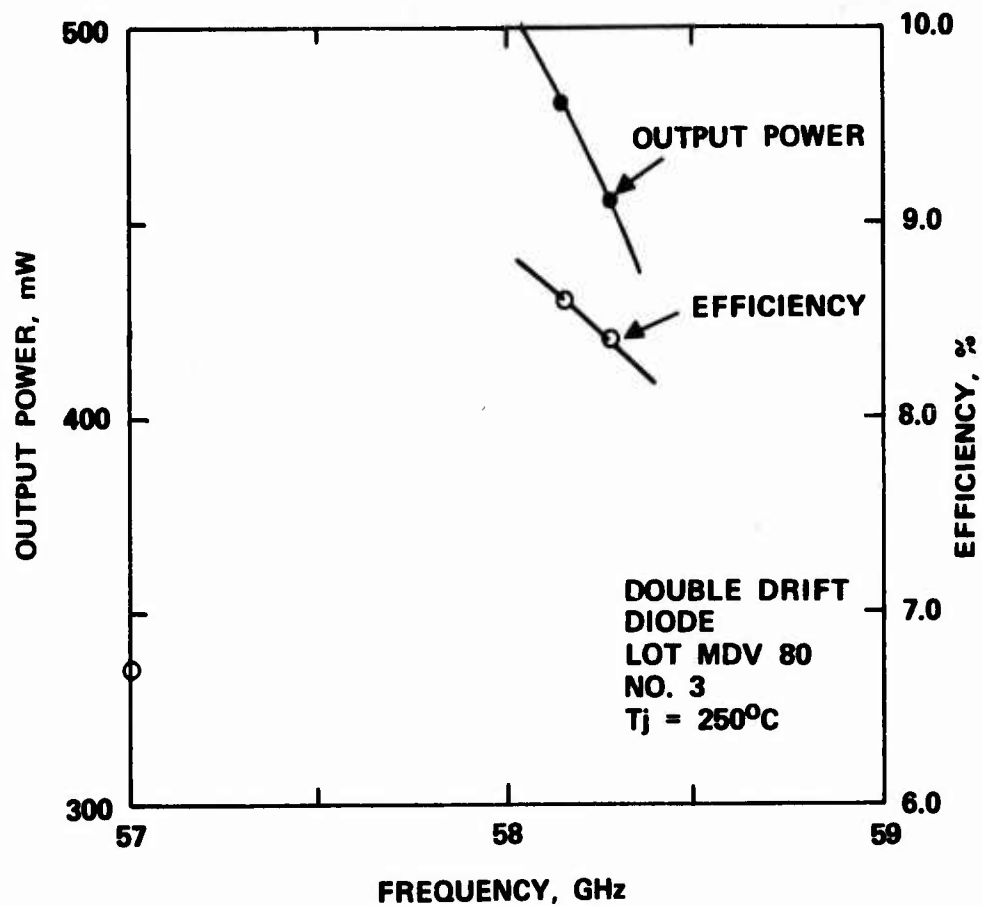


Figure 2.2-4 Output power and dc to RF conversion efficiency of a silicon double-drift IMPATT diode oscillator in a coaxial-coupled reduced height waveguide circuit.

been achieved at 67.5 GHz, however, with an efficiency of 4.7% limited mainly by the circuit.

Most of the high power and efficiency results reported in the literature were obtained by optimally tuning the oscillator at single or narrow frequency range. For FM transmitter oscillator applications, reasonable frequency tuning range ( $\pm 100$  MHz minimum for this program) with bias current is essential, even at the expense of obtaining lower output power and efficiency. Our emphasis was therefore centered on obtaining sufficient bias tuning range and, at the same time, obtaining maximum output power at reasonable diode junction temperature for long term reliable operations.

Bias current tuning characteristics of an identical cavity circuit using diodes from the same wafer lots with similar diode package configurations and diode parameters such as breakdown voltage and zero bias capacitance are in general similar. Figure 2.2-5 and 2.2-6 are the bias current tuning characteristics of two double-drift IMPATT diodes from the same diode lot, (Lot No. MDV 87) and same diode package configuration (quartz ring package with half-strap (HS) gold ribbon connecting the diode to the quartz ring), but with zero bias capacitance of 1.2 pf and 1.5 pf respectively. The diode with the 1.2 pf capacitance matched with the circuit better and resulted in 6% efficient and lower junction temperatures. A frequency tuning range of  $\pm 100$  MHz was achieved.

#### 2.2.2 60 GHz FM IMPATT Diode Transmitter Units (FM IDTUs)

For developing reliable FM IDTUs, all the oscillators developed were subjected to a "burn-in" period, in which, the units were continuously operated at their normal operating junction temperatures for at least 48 hours. Diodes of poor metallization or soldered poorly onto the

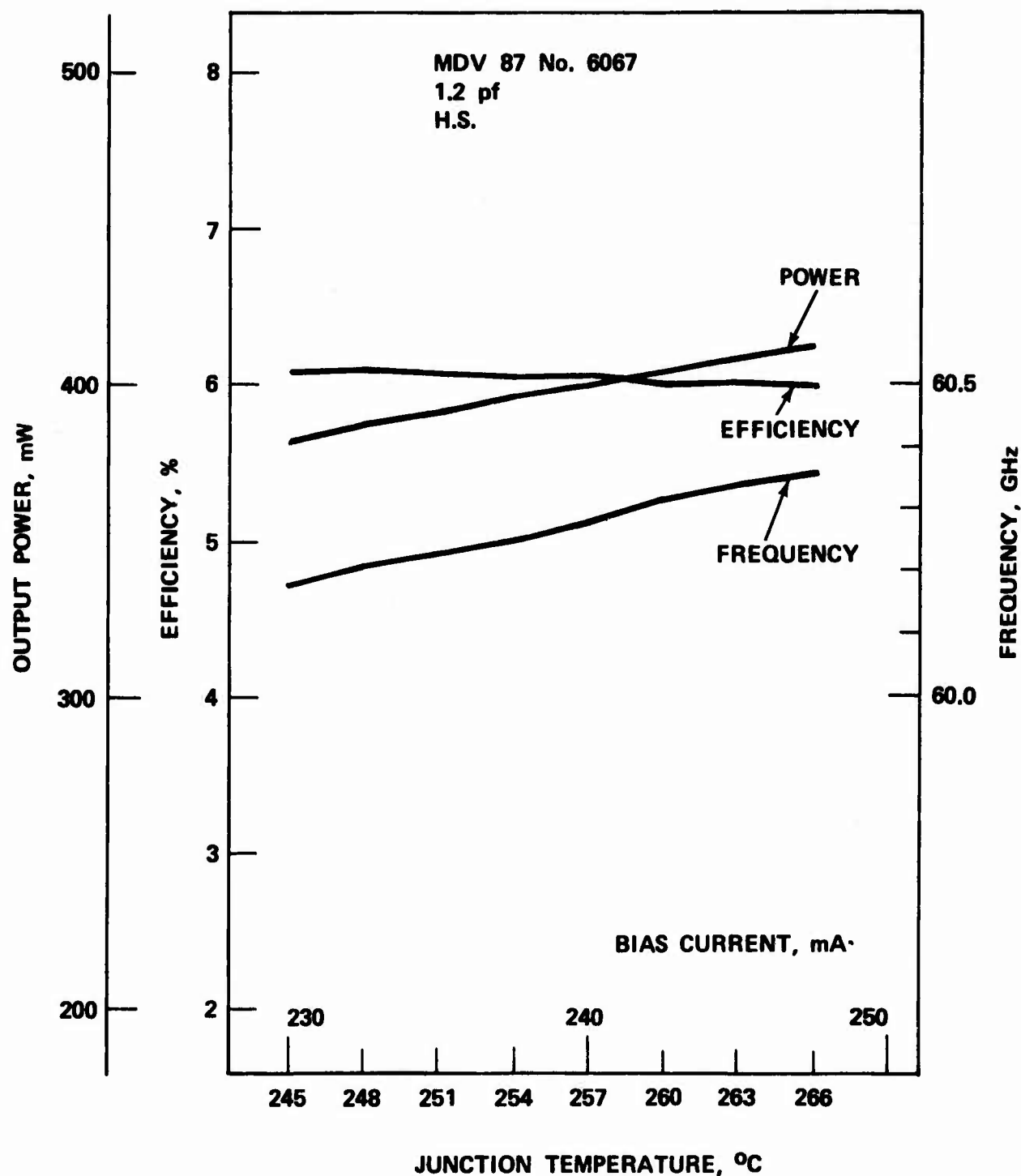


Figure 2.2-5 Bias current tuning characteristics of a 60 GHz oscillator using double-drift silicon IMPATT diode on copper heatsink. Diode breakdown voltage equals 23 volts, and diode capacitance equals 1.2 pf.

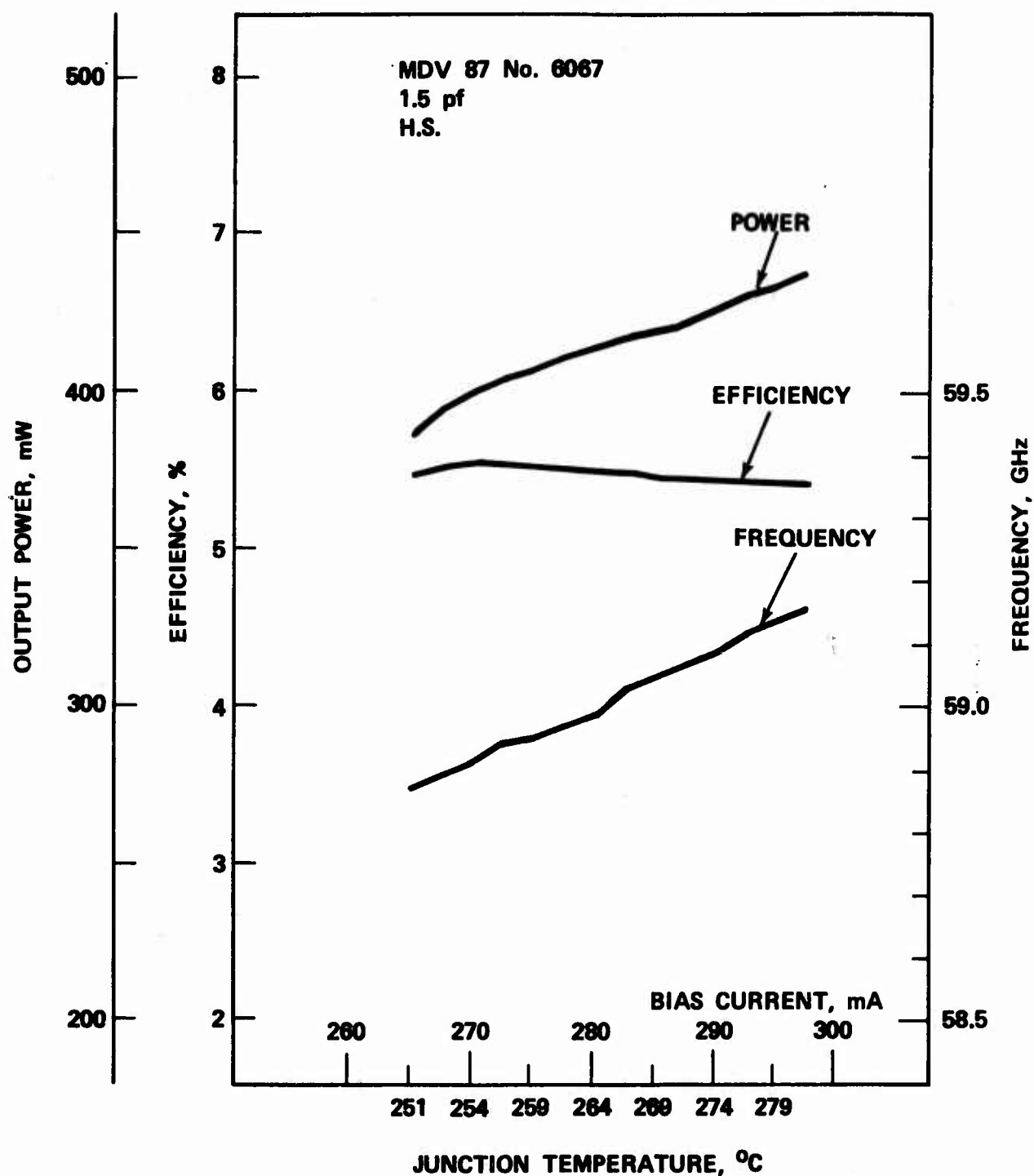


Figure 2.2-6 Bias current tuning characteristics of a 60 GHz oscillator using a double-drift IMPATT diode from the same diode lot as shown in Figure 2.2-5 but with a larger diode capacitance of 1.5 pf.



heatsinks were likely to burnout or their r.f. characteristics (i.e., output power and frequency) would shift. Two FM IDTUs were finally completed and delivered to ECOM for evaluation. This section reports our test results of the units (Unit A: TO-V-A, and Unit B: TO-V-B, where TO stands for transmitter oscillator, and V, for V-band units).

#### Output Power - Frequency Tuning Characteristics

Bias tuning characteristics of TO-V-A is shown in Figure 2.2-7. This oscillator achieved 520 mW output power at 5.7% efficiency. It has a frequency tuning range of over 500 MHz with minimum output power of 320 mW. The diodes were very stable during the burn-in period and led us to suspect that the estimated diode junction temperatures based on the extrapolated experimental thermal resistance data, were perhaps higher than the actual junction temperatures for this diode. The output power of this oscillator varied over  $\pm 1$  dB. The oscillator frequency decreased as the bias current increased which is common depending on the external circuit characteristics.

Tuning characteristics of the second unit, TO-V-B is shown in Figure 2.2-8. This unit is continuously bias current tunable from 60.2 GHz to 61.4 GHz, a tuning range of 1.2 GHz. However, the unit has a maximum efficiency of 5% at 340 mW, lower than those of unit A. The unit can be operated at the normal junction temperature of 260°C and 330 mW to meet the requirement of this program. External circuit looping caused a frequency jump at a bias current of 270 mA as shown in the figure. This is expected because of the complexity of the coaxial-cross coupled waveguide circuit. VSWR at either the tuning short terminal or the cross-guide section will cause phase shift loops that form external circuit looping on the circuit admittance plot. When more than two points are intercepted between the diode (device)

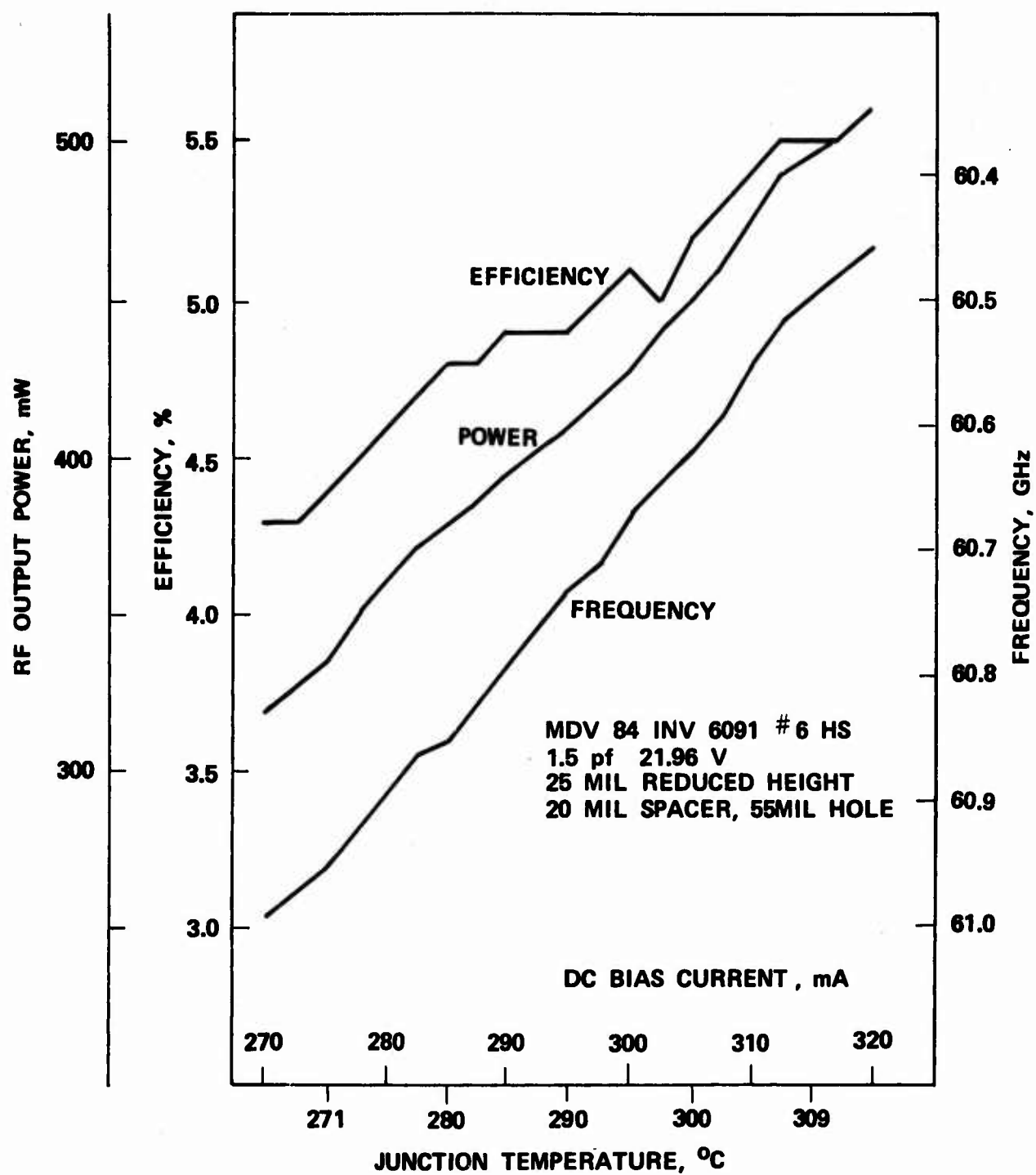


Figure 2.2-7 Bias current tuning characteristics of TO-V-A.

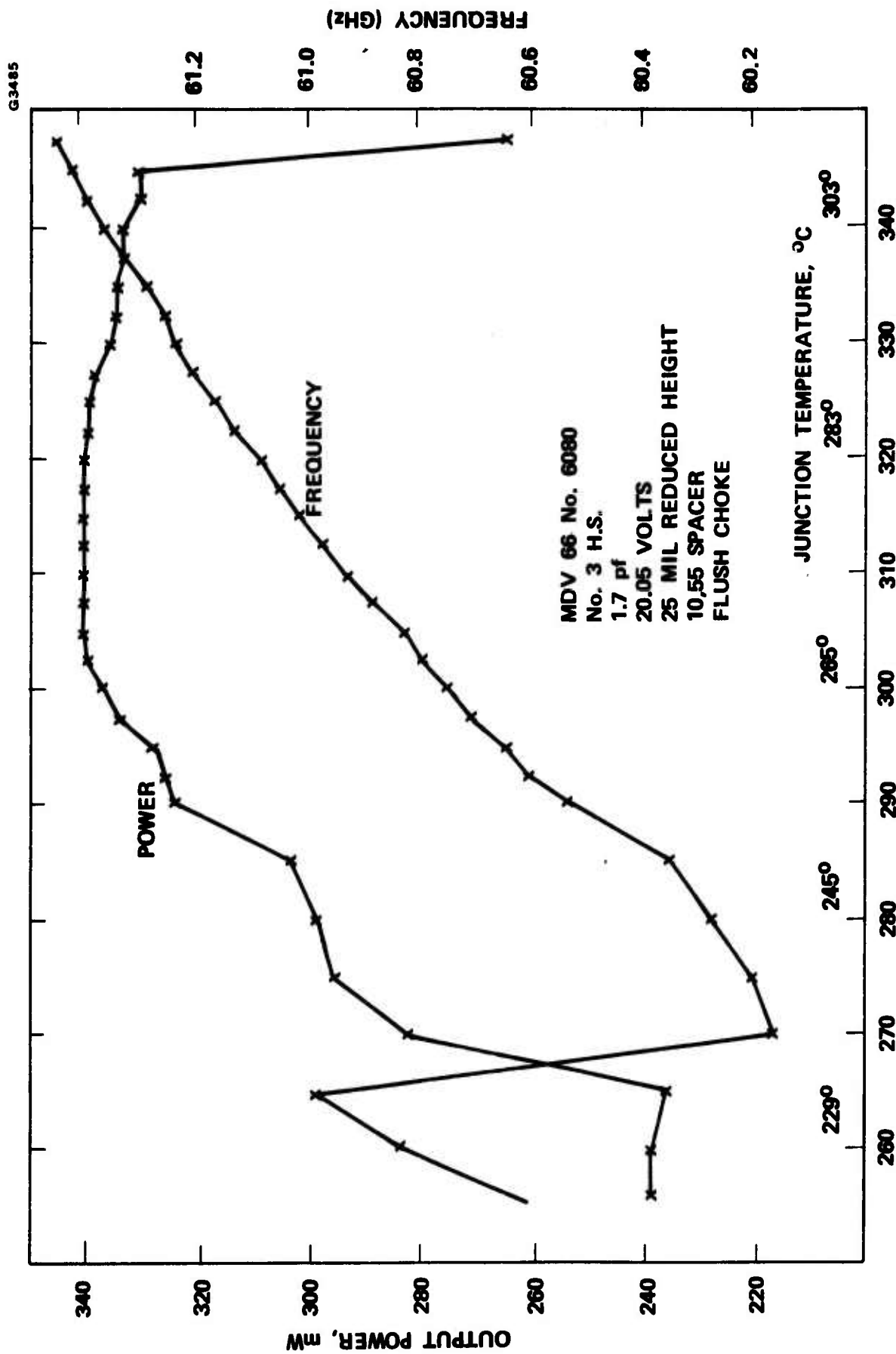


Figure 2.2-8 Bias current tuning characteristics of TO-V-B.

admittance and the external circuit admittance (because of the external circuit looping) the oscillation can jump from one frequency (at one admittance intercept) to another frequency (at another admittance intercept).<sup>11</sup>

### Noise Characteristics

IMPATT diode oscillators are in general considered noisy because of their intrinsic noise characteristics associated with the random avalanche process. The noise can be reduced by either injection locking the oscillator with a quiet source or using a high Q cavity circuit to either trigger or limit a more uniform avalanche process in the device. For free running IMPATT oscillators, not only the external circuit impedance determines the noise behavior, the bias circuit used for the oscillator at certain conditions will have negative resistance at very low frequencies and can cause bias circuit oscillations which form noise like sidebands in the oscillators.<sup>3,9,12,13</sup> Normally, for double-drift diodes with larger negative impedance, power capability, and efficiency, we expect lower noise than the single-drift diodes based on theoretical considerations. However, high efficiency diodes also are more prone to bias circuit oscillations. The maximum bias oscillation frequency  $f_{BM}$  can be expressed as

$$f_{BM} = \frac{f}{Q_L} \sqrt{\frac{R_-}{R_s} - 1}$$

where  $f$  is the carrier frequency,  $Q_L$  is the circuit loaded quality factor.  $R_s$  is the diode space charge resistance, and

$$R_- = \frac{m}{4 e E_c} \frac{1}{|G|} \left( \frac{dP_o}{dI} \right)$$

where  $d$  is the active layer width,  $E_c$  is the critical field.  $G$  is the optimum negative conductance, and  $dP_o/dI$  is the slope of the output power versus dc bias current.

$$m = \left[ \frac{E_c}{\alpha_n} \frac{d\alpha_n}{dE} \right]_{E_c} + \left[ \frac{E_c}{\alpha_p} \frac{d\alpha_p}{dE} \right]_{E_c}$$

where  $\alpha_n$ , and  $\alpha_p$  are ionization coefficients for electrons and holes, respectively. For 50 GHz diodes, calculation shows that

$$f_{BM} \sim 3.6 \text{ GHz}$$

is possible.<sup>9</sup> These high frequency bias oscillations cannot be suppressed by using a bias current regulator circuit. They can be suppressed by either loading the bias with lossy materials at these frequencies, or properly terminating the low frequency oscillations with a filter design at the R.F. choke section of the diode bias.

We have measured the double sideband (DSB) AM noise of the units TO-V-A and TO-V-B as shown respectively in Figure 2.2-9 and Figure 2.2-10. The unit TO-V-A shows lower noise at 60 MHz from carrier than at 1.5 GHz from carrier. This indicates noise generation due to bias circuit oscillations near 1.5 GHz which cannot be properly terminated with the present anodized aluminum R.F. choke design. This will be more obvious as we later present more of our noise data on transmitter oscillators and local oscillators with the same choke design. However, the overall AM noise of TO-V-A is less than -128 dBc/100 Hz with the best result at -132.4 dBc/100 Hz which is reasonably low noise for IMPATT oscillators.

The unit TO-V-B shows more noise than TO-V-A. Here the near carrier (60 MHz away) and far carrier (1.5 GHz away) noise are about the same order of magnitude simply because the noise of the oscillator is

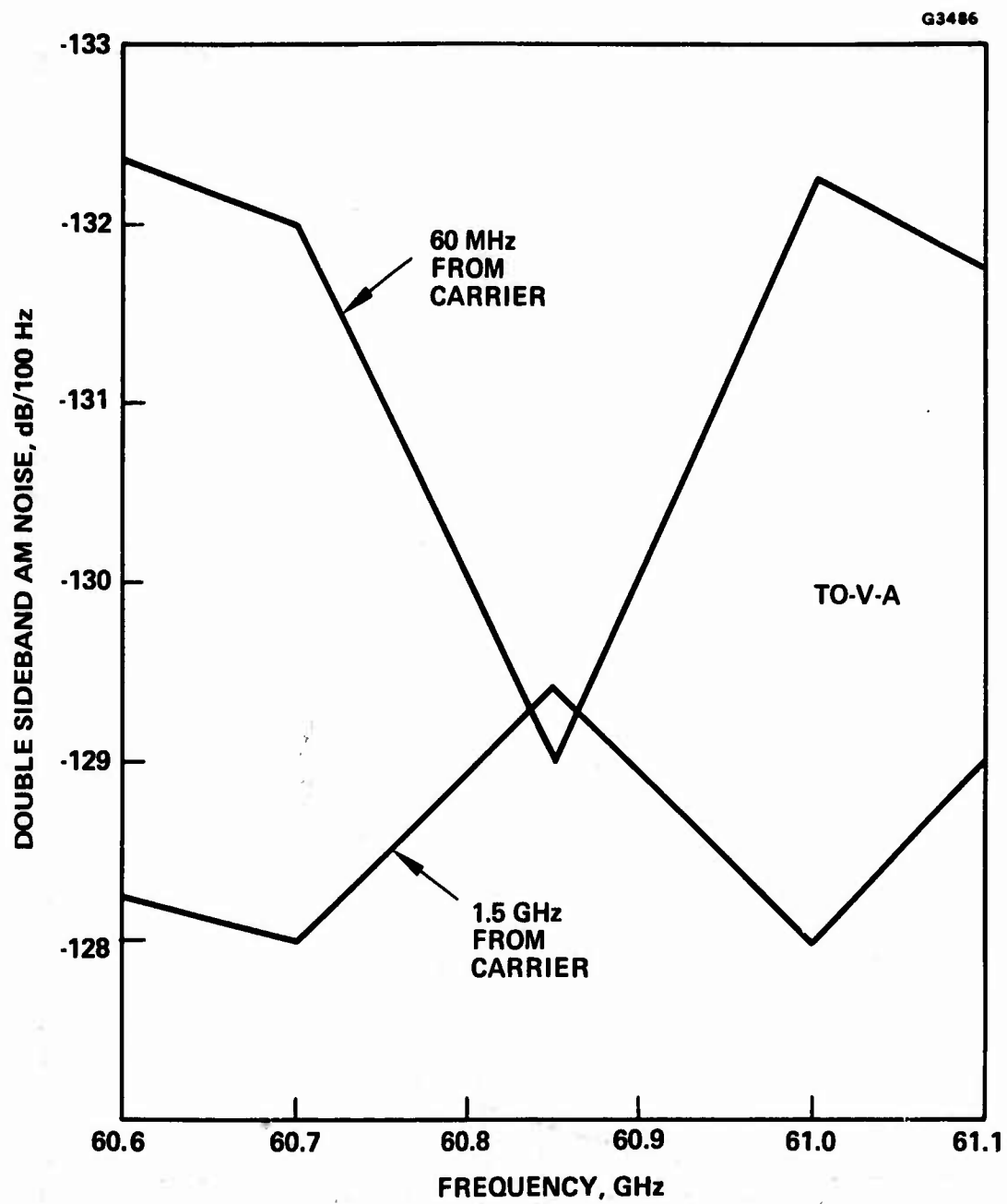


Figure 2.2-9 AM noise characteristics of TO-V-A.

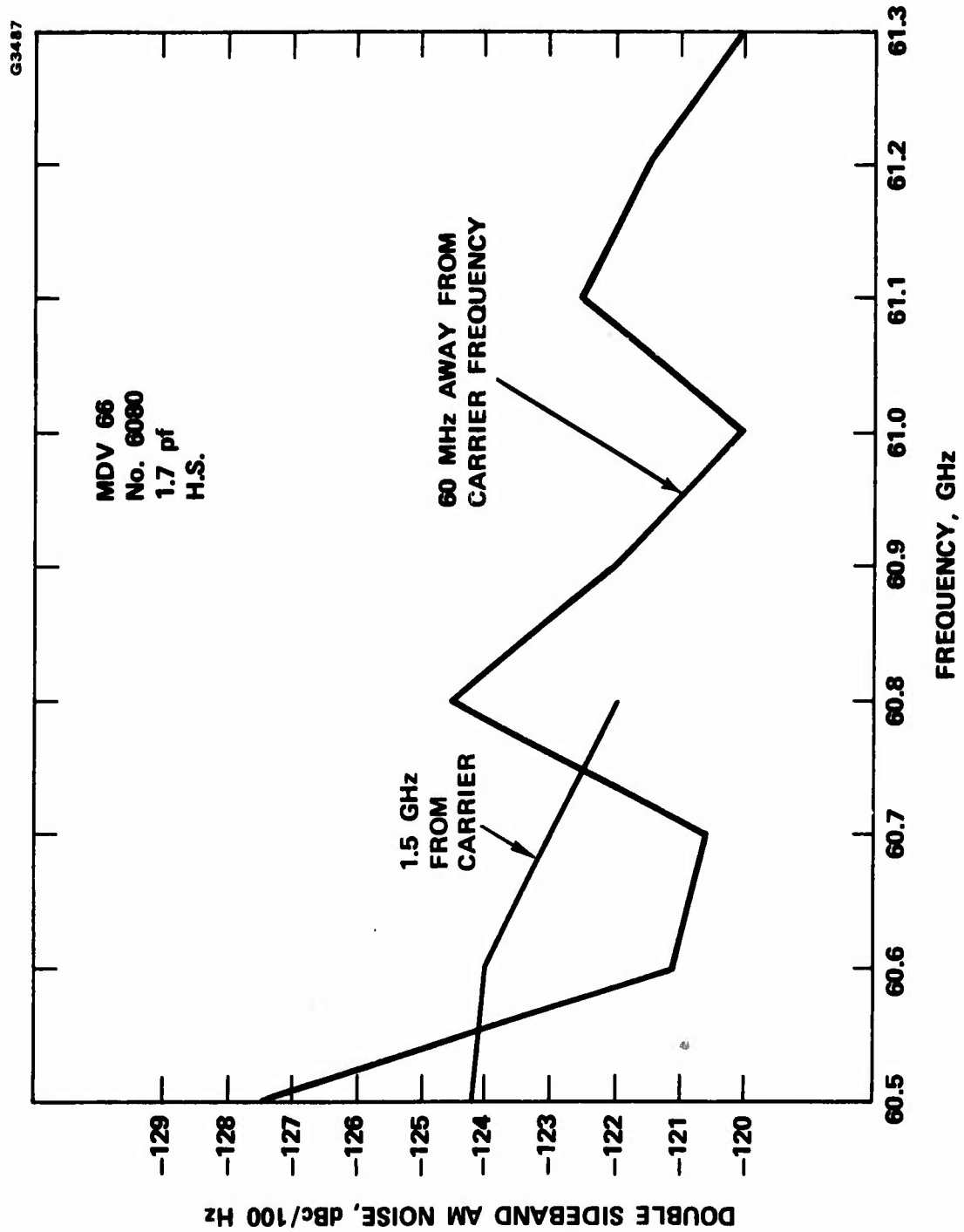


Figure 2.2-10 AM noise characteristics of TO-V-B.

in general high. The fluctuation of noise at different carrier frequencies is related to the external circuit and device-circuit interaction, which also causes minor output power fluctuations. No attempts were made in this program to specially suppress bias oscillations.

#### Frequency Shift - Ambient Temperature Effect

IMPATT oscillator characteristics change as ambient temperature varies. This is because the avalanche coefficients of IMPATT diodes are a strong function of temperature so that the diode r.f. impedance also varies strongly with the temperature. This can be compensated however by using an external heater to control the IMPATT oscillator heatsink temperature to a fixed elevated value against ambient temperature variations. If the transmitter oscillator frequency shift is small, the receiver circuit with AFC search/lock can also compensate for the transmitter drift. Nevertheless, it is important to know the frequency shift characteristics of the transmitter oscillators. Figure 2.2-11 is the frequency shift effect of TO-V-A. The IMPATT oscillator was placed in a temperature controlled chamber while the frequency of the oscillator was monitored. The average frequency drift is about  $4 \text{ MHz}/^{\circ}\text{C}$  at  $25^{\circ}\text{C}$ . Figure 2.2-12 is the frequency shift characteristics to TO-V-B. It has a frequency drift of  $20 \text{ MHz}/^{\circ}\text{C}$  at  $25^{\circ}\text{C}$ . The higher the circuit Q-factor the better the temperature stability, but smaller bias current frequency tuning range results.

A picture of one of the 60 GHz FM IDTUs is shown in Figure 2.2-13. The oscillator cavity is mounted on a copper heatsink block with aluminum heatsink fins. A ferrite isolator is connected to the oscillator output to prevent frequency pulling due to external load



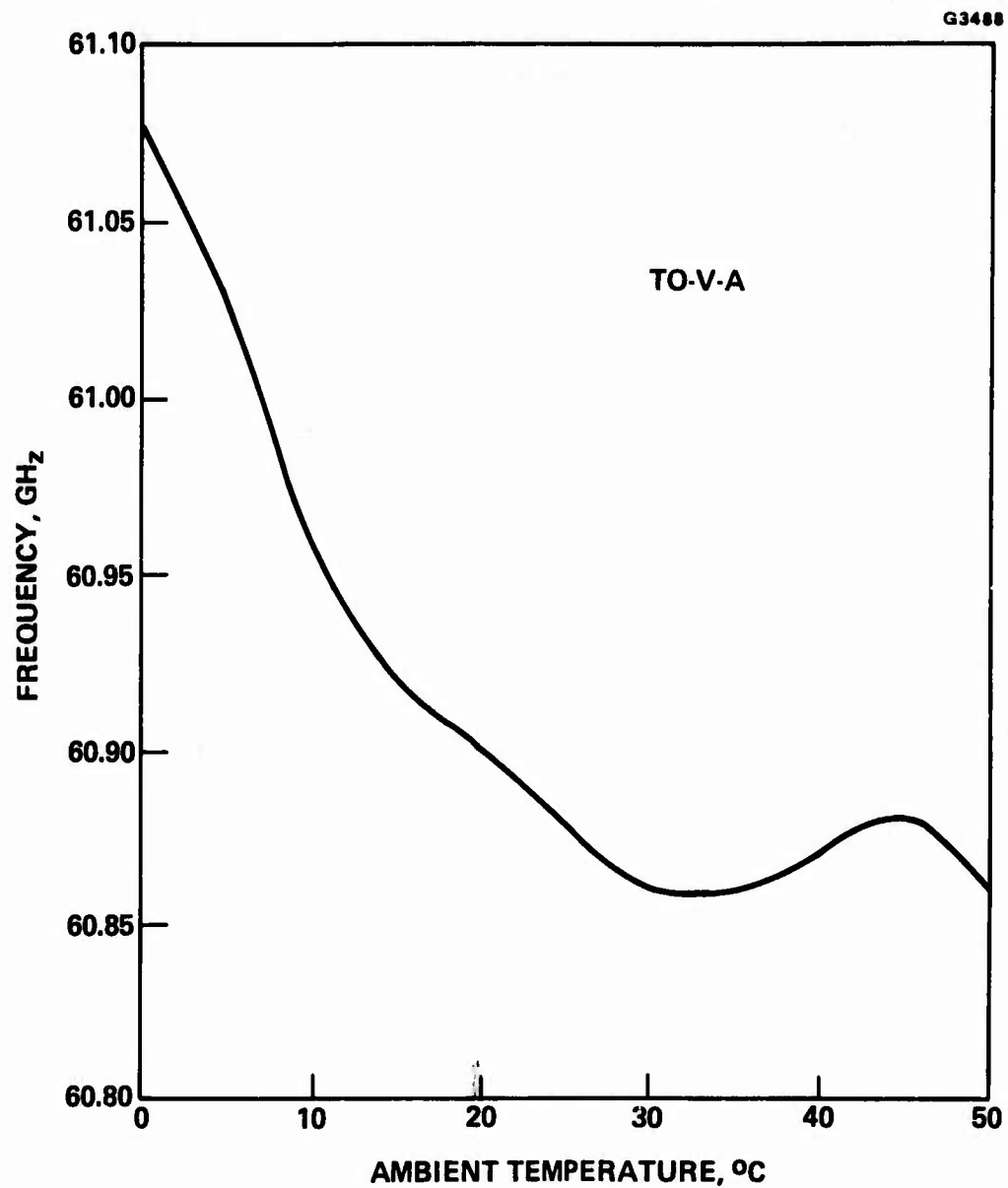


Figure 2.2-11 Frequency stability against ambient temperature variations of TO-V-A.

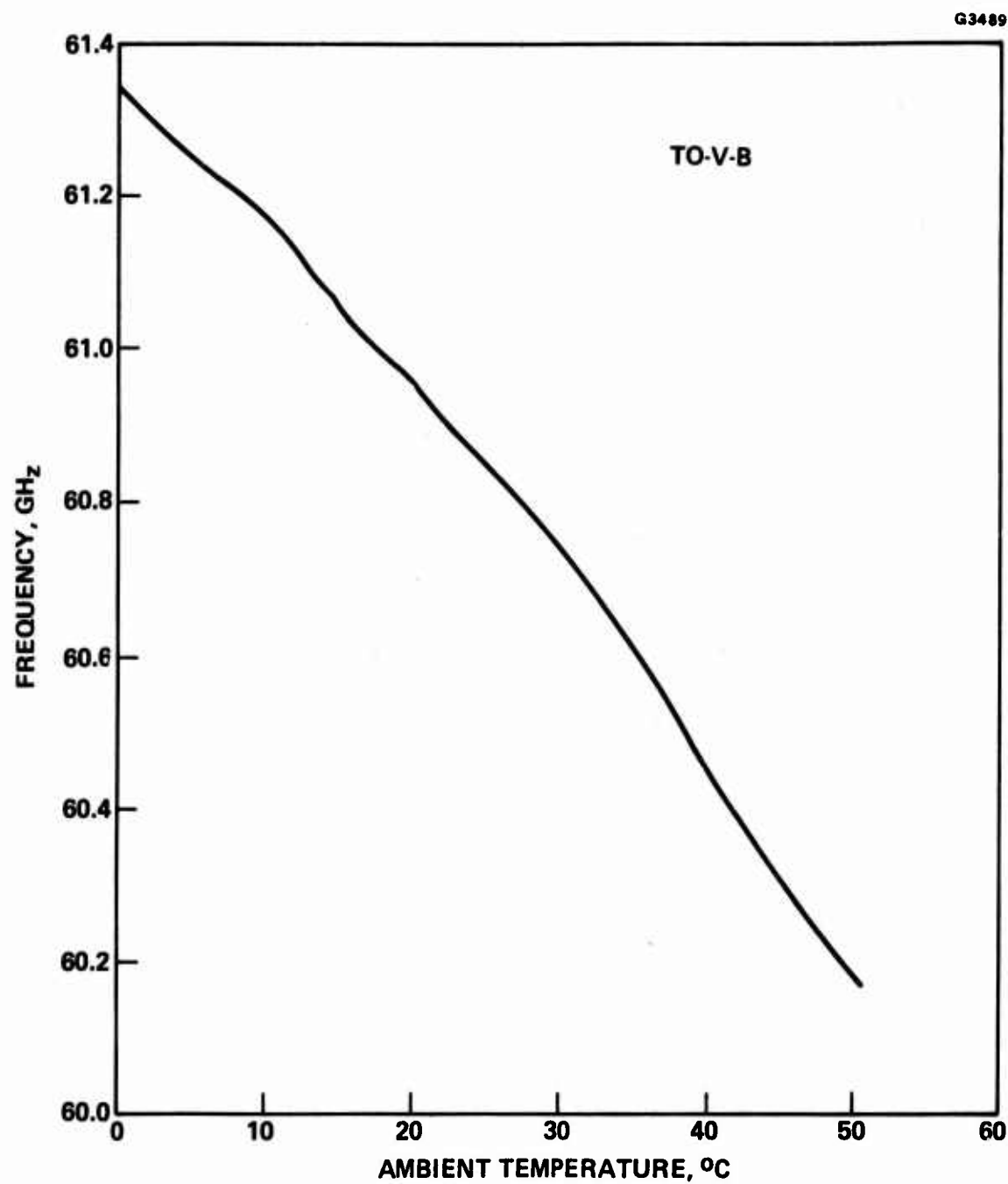


Figure 2.2-12 Frequency stability against ambient temperature variations of TO-V-B.

E1175

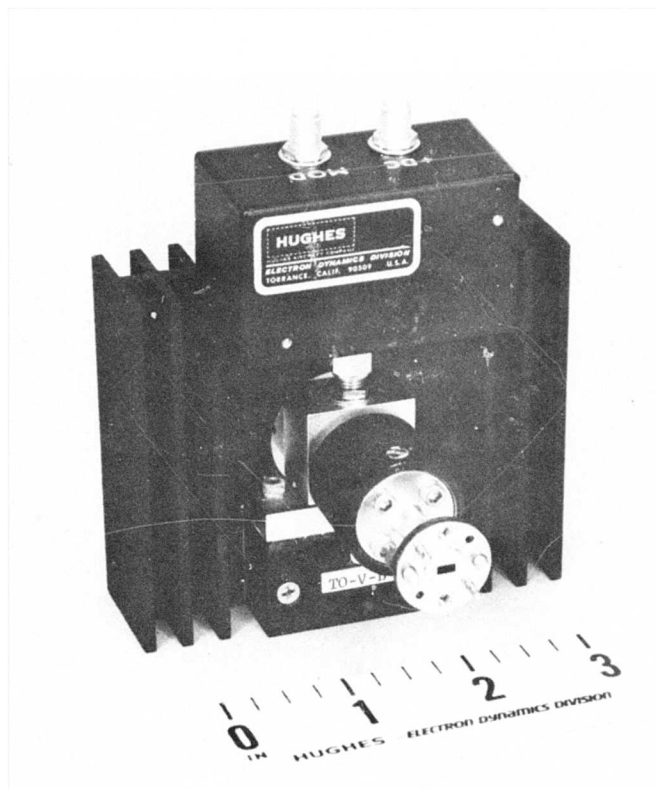


Figure 2.2-13 Picture of a 60 GHz FM IDTU.

mismatch. The isolators used were tuned to have a low insertion loss of between 0.7 and 1.0dB. A regulator/modulator circuit box is mounted directly above the IMPATT diode bias and securely anchored to the heatsinks. The bias current of the IMPATT is well regulated with the use of an IC regulator. Current modulation is achieved by sharing the total bias current between the IMPATT diode and a modulation transistor. The IMPATT oscillator can be modulated up to 150 MHz with this simple circuit. (See Figure 4.1.2).

## 2.3 94 GHz FM TRANSMITTER OSCILLATORS

### 2.3.1 94 GHz IMPATT Oscillator Circuit

The 94 GHz double-drift IMPATT oscillators using the circuit shown previously in Figure 2.2-1 have been extensively evaluated. Our first approach was to use  $p^+-p-n-n^+$  doping profile silicon diodes mounted on copper heatsinks for device evaluation. We have found in general that the devices were capable of generating high output power at reasonable efficiency but with substantially higher diode junction temperature than the normal reliable operating junction temperature of 250°C. Figure 2.3-1 is the performance characteristic of one of these oscillators. The oscillator power and efficiency was peaked with the mechanical tuning short at each different fixed bias current. Bias current frequency tuning range at each optimal output power level was limited to less than 50 MHz. Maximum output power of 390 mW at 5.9% efficiency was obtained at a high junction temperature of 370°C near diode burn-out. The results suggest that either the device design was not optimized or the circuit impedance level was not compatible with that of the device impedance. One major circuit problem is perhaps the use of quartz ring packages for the high frequency diodes. The package parasitics become dominant parts of the overall circuit.

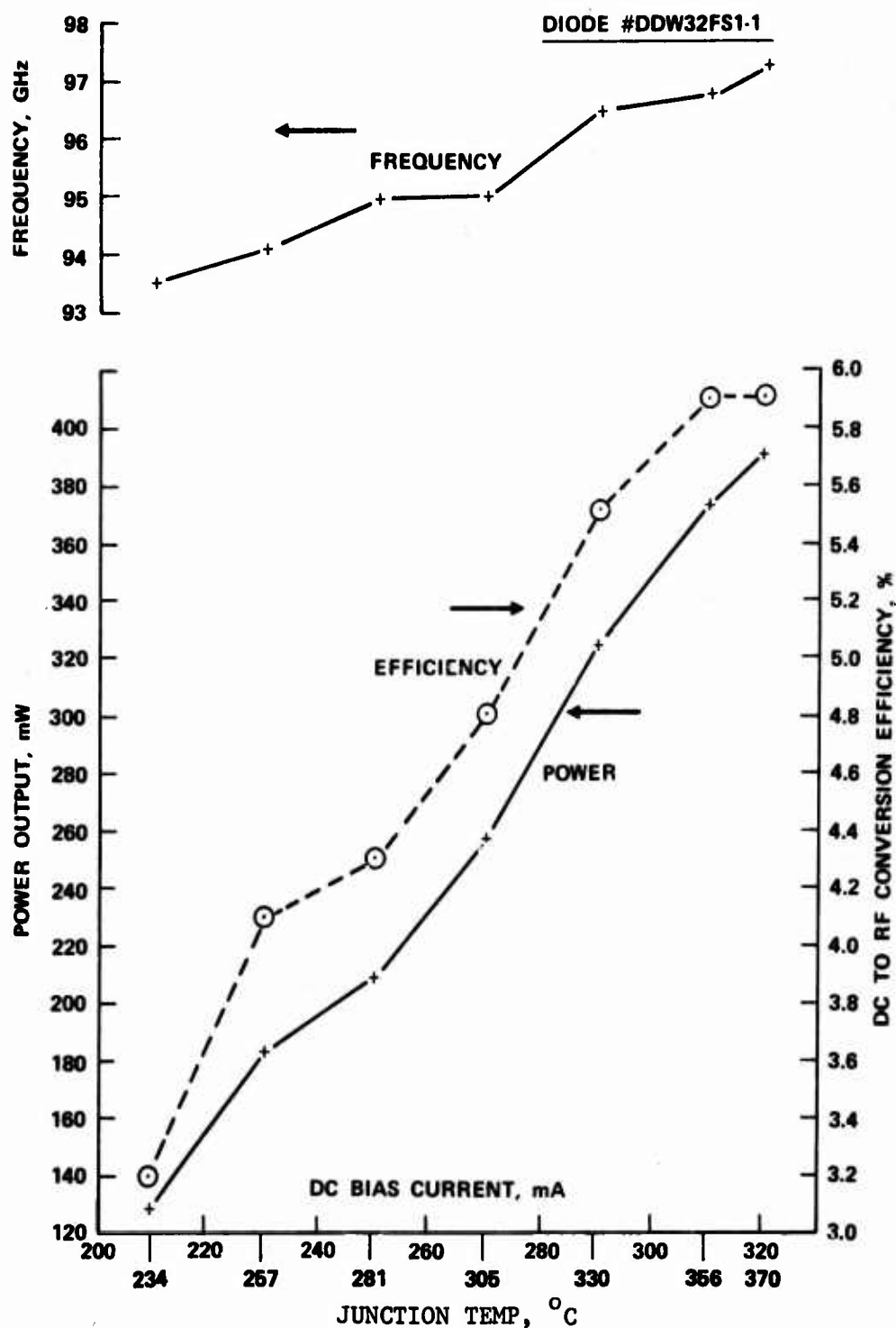


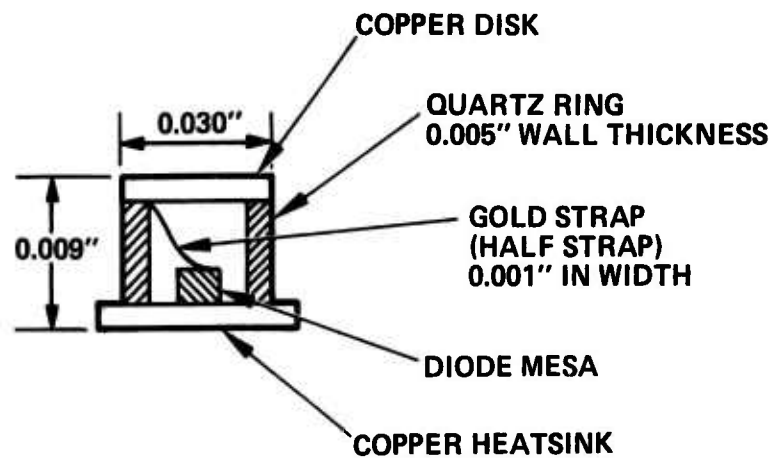
Figure 2.3-1 Tuning characteristics of a 94 GHz double-drift IMPATT diode oscillator in a coaxial coupled reduced height waveguide circuit. Output power was peaked for each fixed bias current by tuning with the sliding short.

We have found, for example, that by using the quartz ring package with a single gold strap, close to 10 GHz of frequency downshift was generally observed from that of using the package of full strap configuration as shown in Figure 2.3-2. Furthermore, the orientation of the straps with respect to the waveguide propagation direction also affects the output power and frequency, and should be further studied.

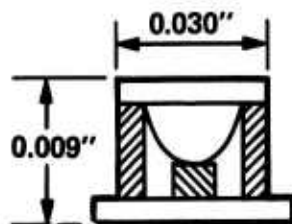
In order to meet our program goals of achieving transmitter output power of larger than 200 mW at 94 GHz and bias current tuning range in excess of  $\pm 100$  MHz, for effective 100 Megabits per second data transmission, we have chosen to use devices mounted on type-IIa diamond heatsinks so that the diode thermal impedance can be lowered and better impedance match between the device and the circuit can be realized at higher bias current levels with lower junction temperatures.

The use of diamond heatsinks to minimize the thermal limitation of output power by lowering the thermal resistance between the diode junction and heatsink has been discussed in Section 2.1. For typical 94 GHz silicon double-drift IMPATT diodes, a thermal resistance of  $28.5^{\circ}\text{C/W}$  using diamond heatsinks compared with  $43.0^{\circ}\text{C/W}$  using copper heatsinks represents a  $1/3$  reduction in thermal impedance.<sup>10</sup>

The use of a quartz ring diode package at 94 GHz, normally degrades the output power and efficiency of an oscillator because of the package parasitics which are difficult to tune out. Our results of 390 mW at 5.9% efficiency using a packaged diode on a copper heatsink are compatible with the best results reported in the literature using metal heatsinks for double-drift diodes at these frequencies,<sup>18,8</sup> without using packaged diodes. However, by mounting diodes on diamond heatsinks, the best results achieved are 550 mW and 8.1% efficiency at  $292^{\circ}\text{C}$  junction temperature and 620 mW at 7.7% efficiency at  $370^{\circ}\text{C}$  near diode burn-out.<sup>10</sup>



(a) HALF-STRAP QUARTZ RING PACKAGE



(b) FULL-STRAP QUARTZ RING PACKAGE

Figure 2.3-2 Different IMPATT diode package configurations.

In the next section, experimental results of 94 GHz FM transmitter oscillators using packaged silicon double-drift IMPATT diodes on diamond heatsinks will be discussed. The emphasis will not only be on obtaining maximum output power, but also on achieving the desired bias current frequency tuning range as transmitter oscillators.

### 2.3.2 94 GHz IMPATT Diode Transmitter Units (FM IDTUs)

FM IDTUs at 94 GHz have been developed using silicon double-drift IMPATT diodes mounted on diamond heatsinks. The oscillator circuit, which matches reasonably well with the devices, turned out to be very similar to the simple reduced height waveguide circuit with the dimensions  $a$  and  $L$  in Figure 2.2-1 almost reduced to zero. Bias current tuned output power and frequency characteristics of the first FM IDTU unit, TO-W-A, are shown in Figure 2.3-3. This unit shows a 1 GHz bias current tuning range with output power ranges from 240 mW to 275 mW. Although the maximum bias current was close to 420 mA, the junction temperature was less than  $232^{\circ}\text{C}$  above ambient because of the use of diamond heatsink for the double drift diode (thermal impedance of the device was measured to be  $29^{\circ}\text{C/W}$ ). The second FM IDTU, TO-W-B, also has a wide bias current tuning range of 1 GHz as shown in Figure 2.3-4. However, output power of TO-W-B is lower than that of TO-W-A. Because of the low diode junction temperatures of TO-W-B, less than  $212^{\circ}\text{C}$  above ambient, it was possible to generate higher output power at larger bias current levels. However, it tended to operate at higher frequencies at high current levels. The average dc-to-rf conversion efficiency of both 94 GHz FM IDTUs was about 5%.

We have also investigated the AM noise characteristics of TO-W-A and TO-W-B as shown in Figure 2.3-5 and Figure 2.3-6 respectively. The AM noise was measured continuously from 1 KHz away from carrier to 100 KHz away from carrier, and between 1 and 2 GHz away from carrier.



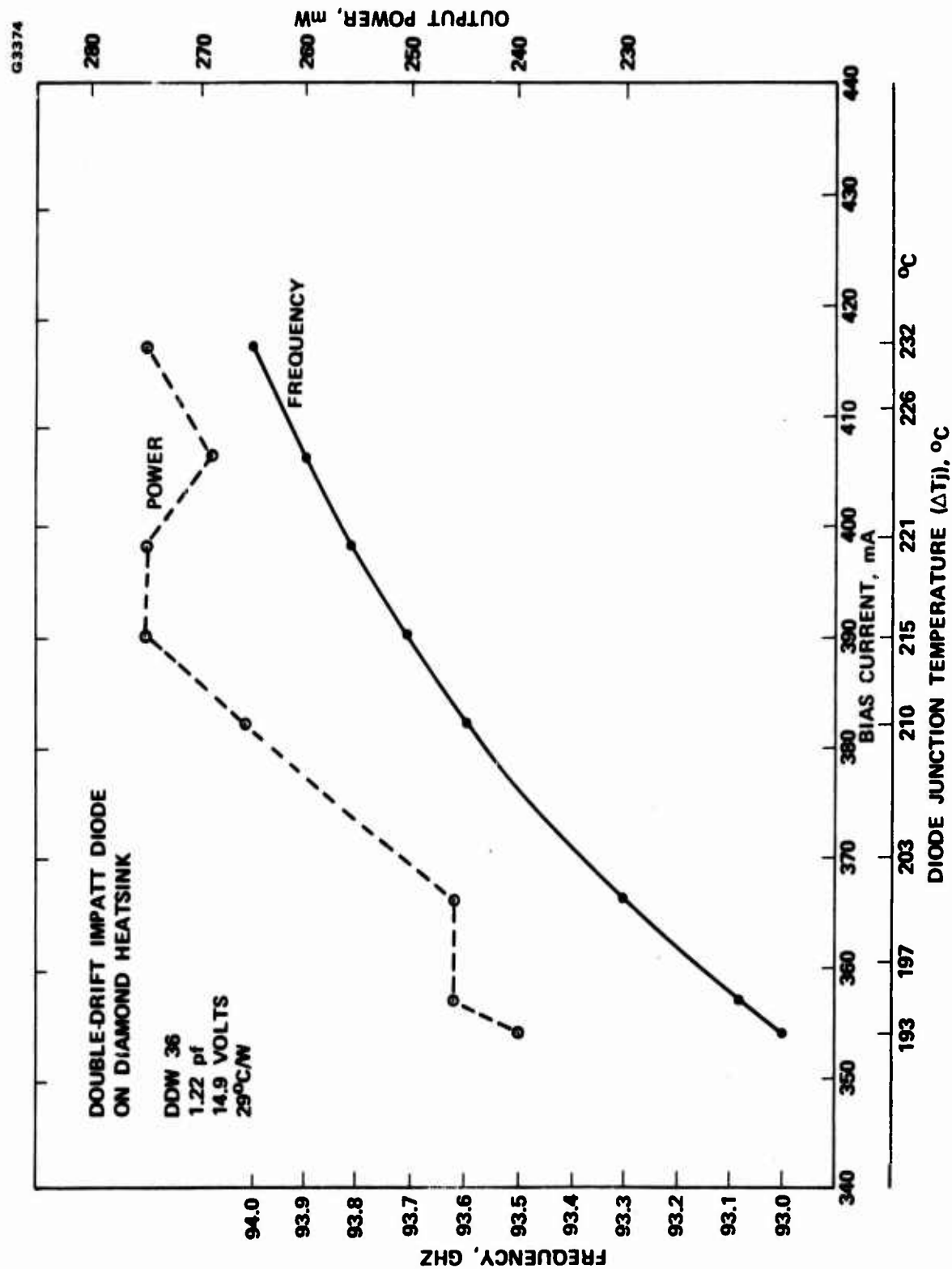


Figure 2.3-3 Bias current tuning characteristics of the 94 GHz FM IDTU, TO-W-A.

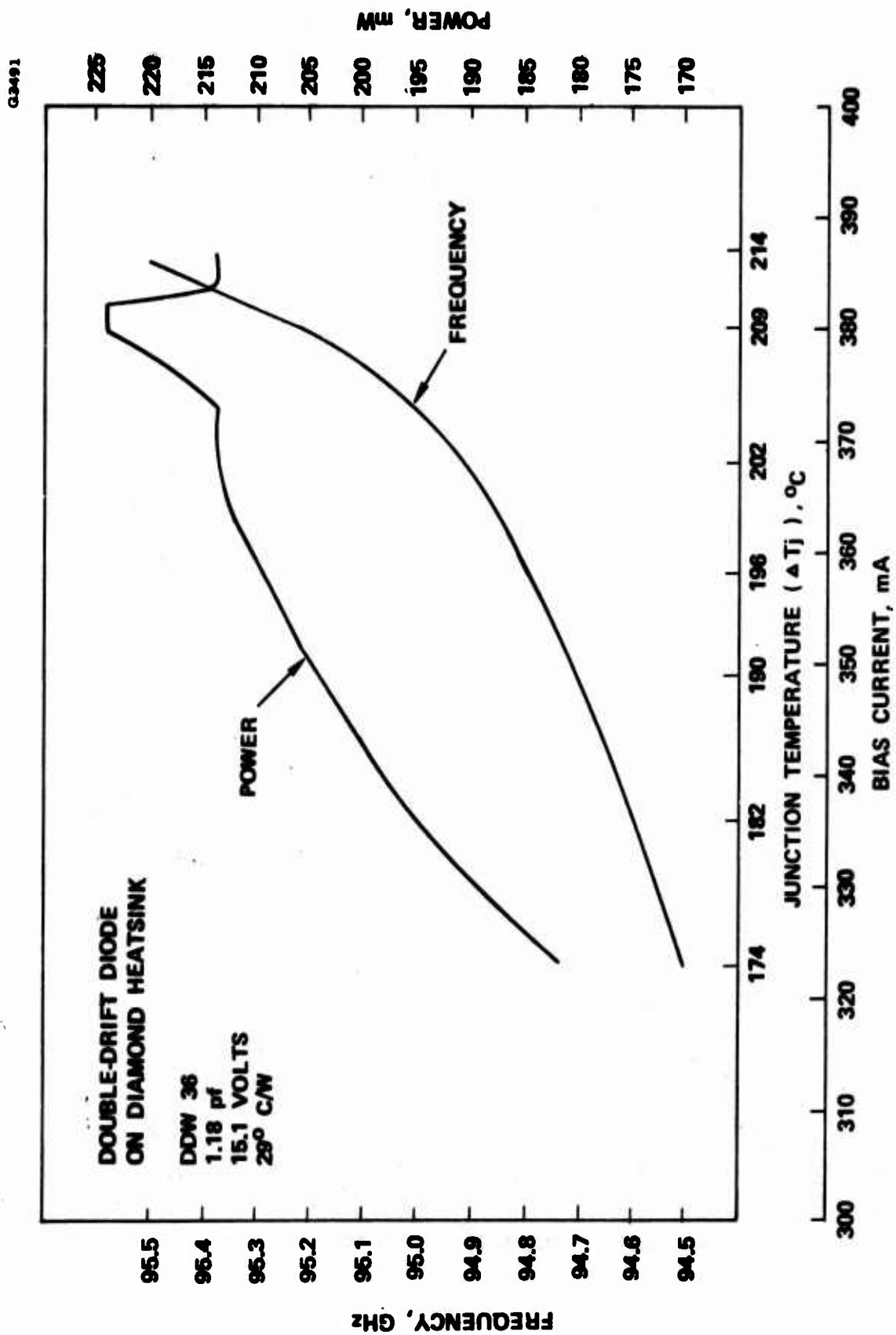


Figure 2.3-4 Bias current tuning characteristics of the 94 GHz FM IDTU, TO-W-B.

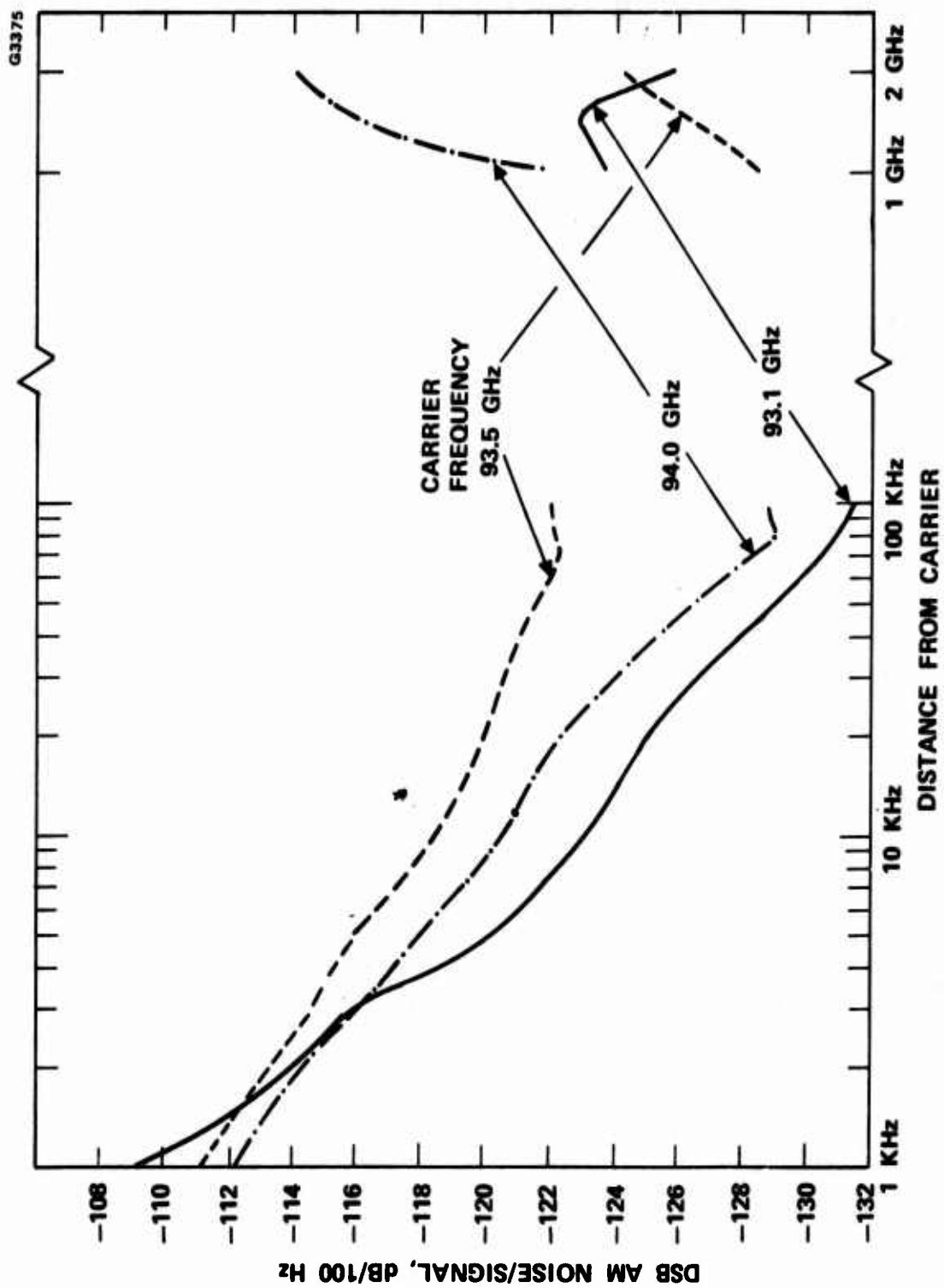


Figure 2.3-5 AM noise characteristics of the 94 GHz FM IDTU, TO-W-A.

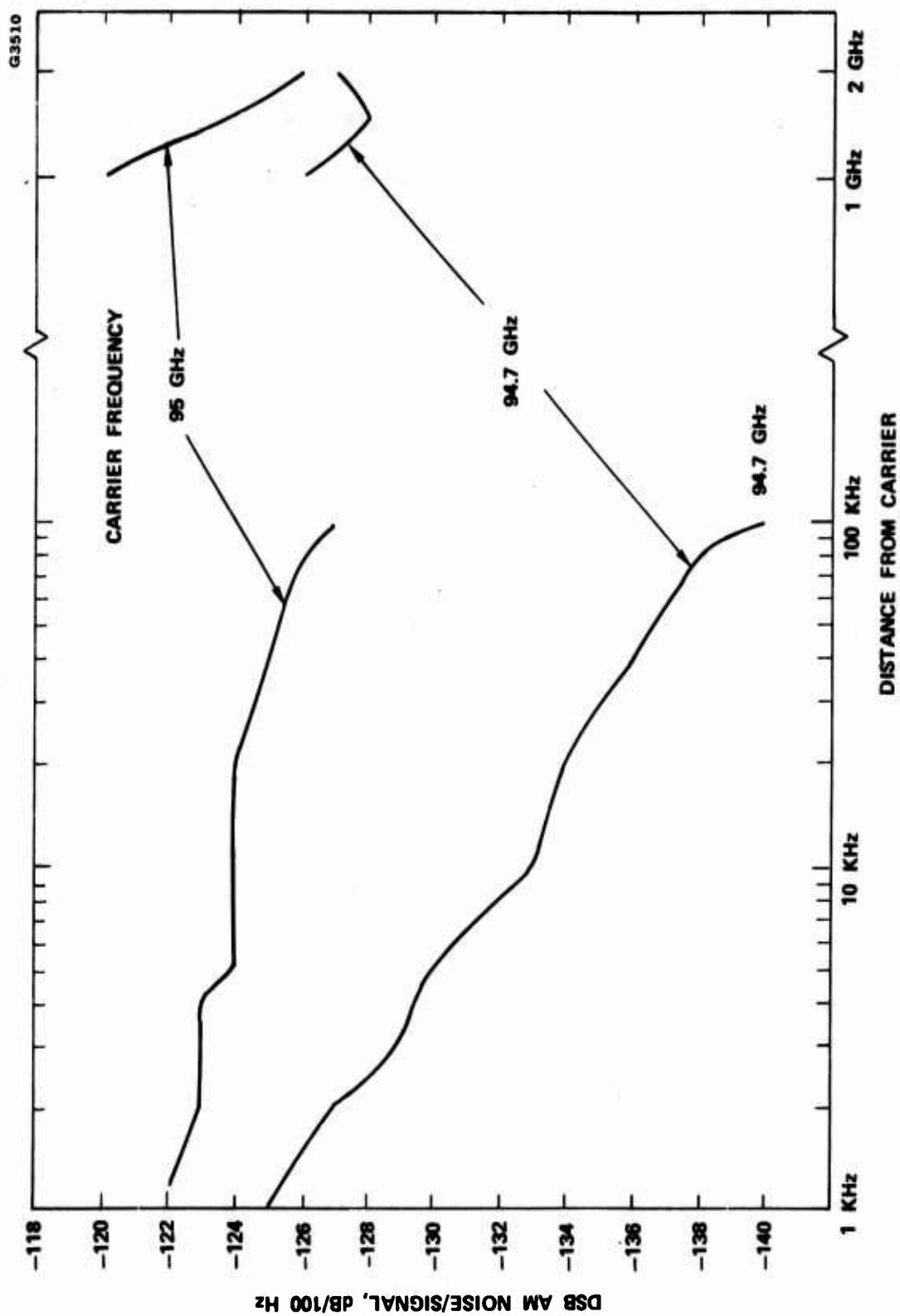


Figure 2.3-6 AM noise characteristics of the 94 GHz FM IDTU, TO-W-B.

Both units showed a gradual decrease in noise toward 100 KHz away from the carrier similar to a  $1/f$  dependence ( $f$  is frequency away from carrier).

However, as we have stated earlier in Section 2.2.2 on 60 GHz FM IDTUs, the same noise characteristics have also been observed here, i.e., the noise at 1 to 2 GHz away from carrier is larger than the near carrier noise. Because of identical R.F. choke designs for both 60 GHz and 94 GHz oscillators, the excess noise at 1 to 2 GHz is caused by the bias circuit oscillation discussed earlier in Section 2.2.

The AM noise for the unit TO-W-B was measured to be as low as -140 dBc/100 Hz at 100 KHz away from carrier. However, down in such a low noise region, experimental uncertainty also becomes significant. Nevertheless, it is certain that double sideband (DSB) AM noise of -138 dbc/100 Hz was obtained.

AM noise at different carrier frequencies of the unit TO-W-A, and TO-W-B is shown in Figure 2.3-7 and Figure 2.3-8 respectively. It is clear from these figures that AM noise was in general higher at 1 GHz away from carrier than at 100 KHz near carrier.

The 94 GHz double-drift IMPATT oscillator noise results, although still not as good as those obtained with Gunn oscillators, have shown a large improvement over single-drift IMPATT oscillators.<sup>14,15,16</sup>

FM noise characteristics of the two 94 GHz units, TO-W-A, and TO-W-B are shown in Figure 2.3-9 and 2.3-10 respectively. The FM noise measured continuously from 1 KHz to 10 MHz away from carrier were about 1 to 2 orders of magnitude higher than normal narrow-tuned IMPATT oscillators.<sup>15,17</sup> This indicates that the circuit Q-factors of the oscillators were small. These affect FM noise more than AM Noise. The

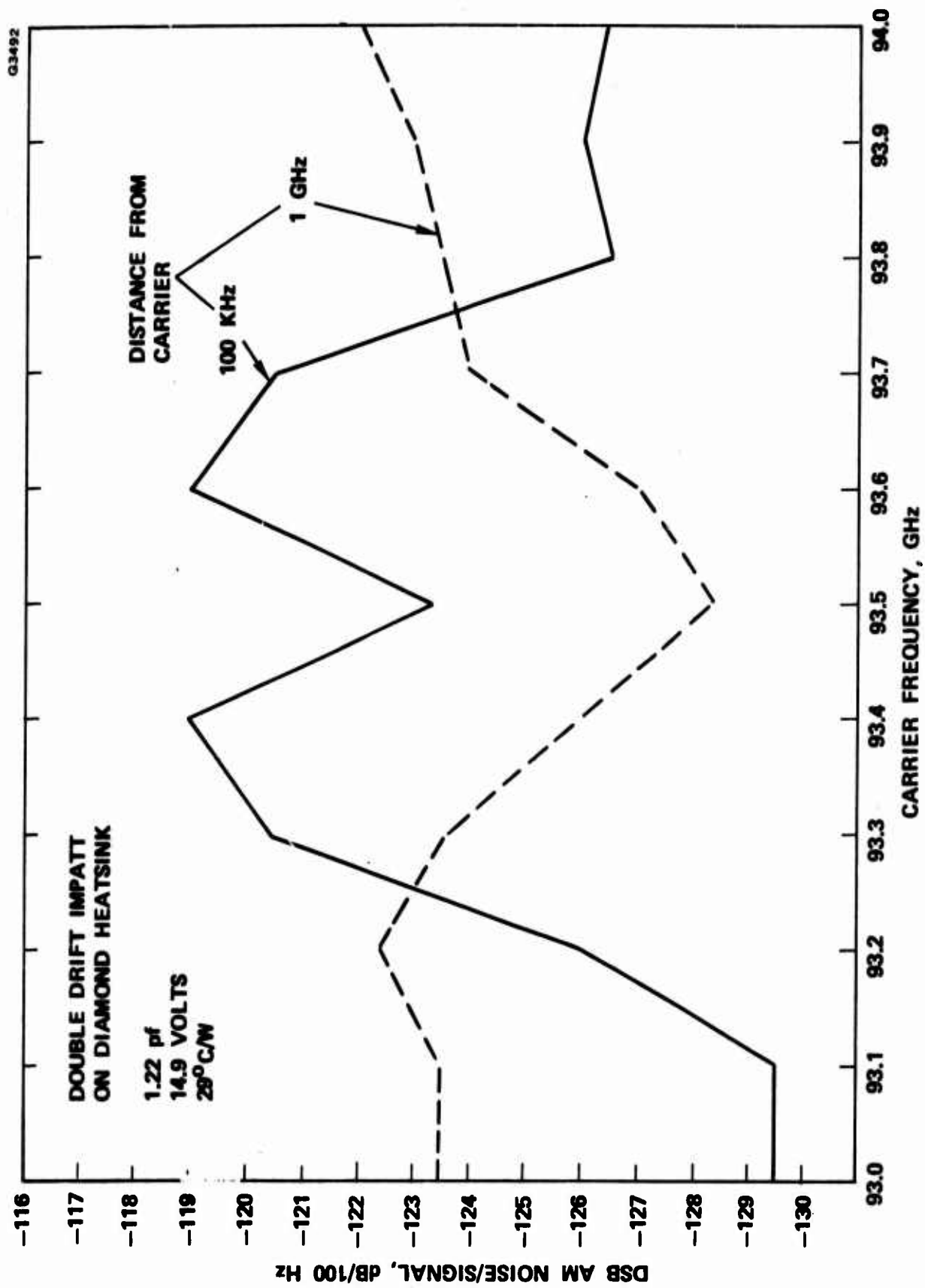


Figure 2.3-7 DSB AM noise at different carrier frequencies of the FM IDTU, TO-W-A.

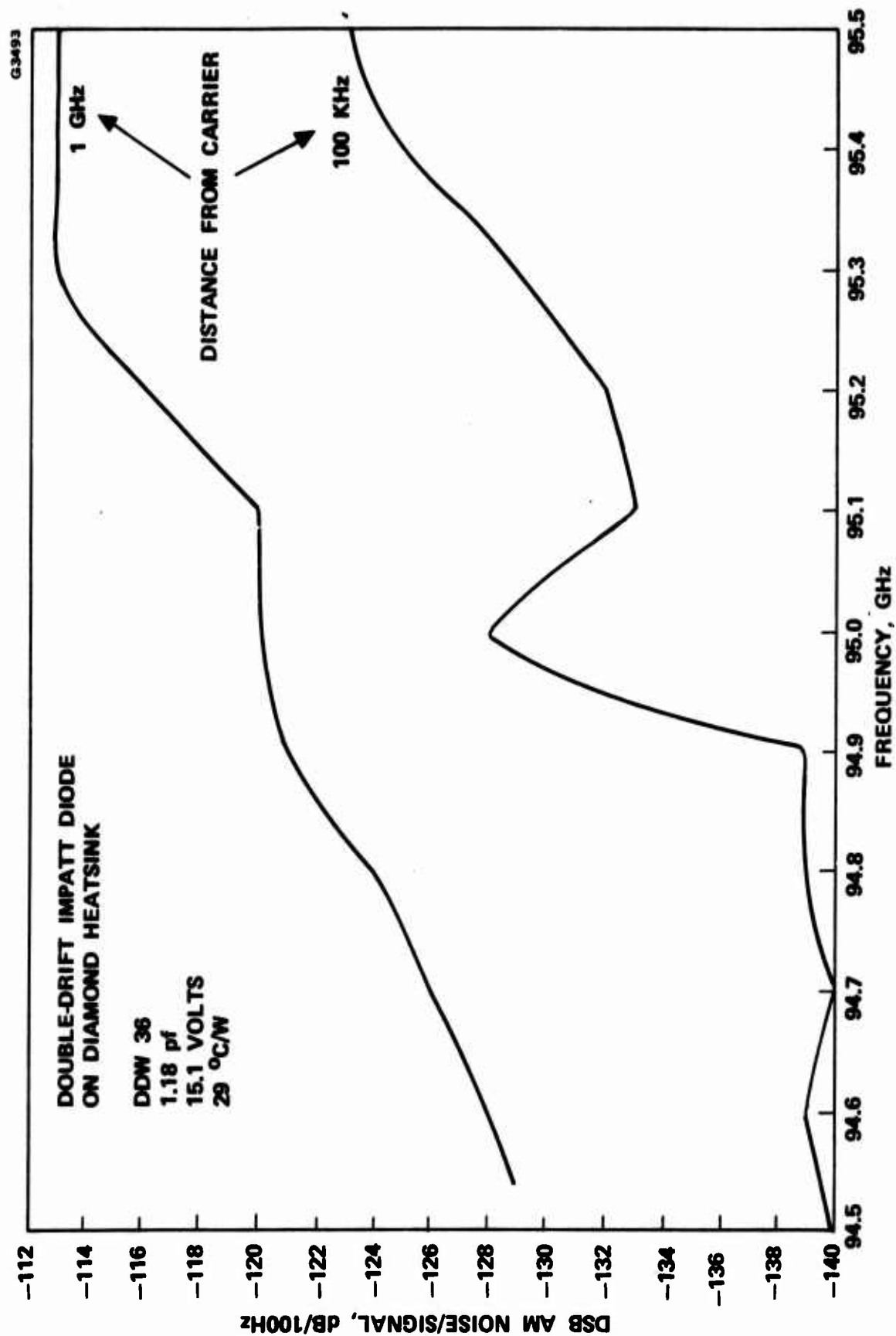


Figure 2.3-8 DSB AM noise at different carrier frequencies of FM IDTU, TO-W-B.

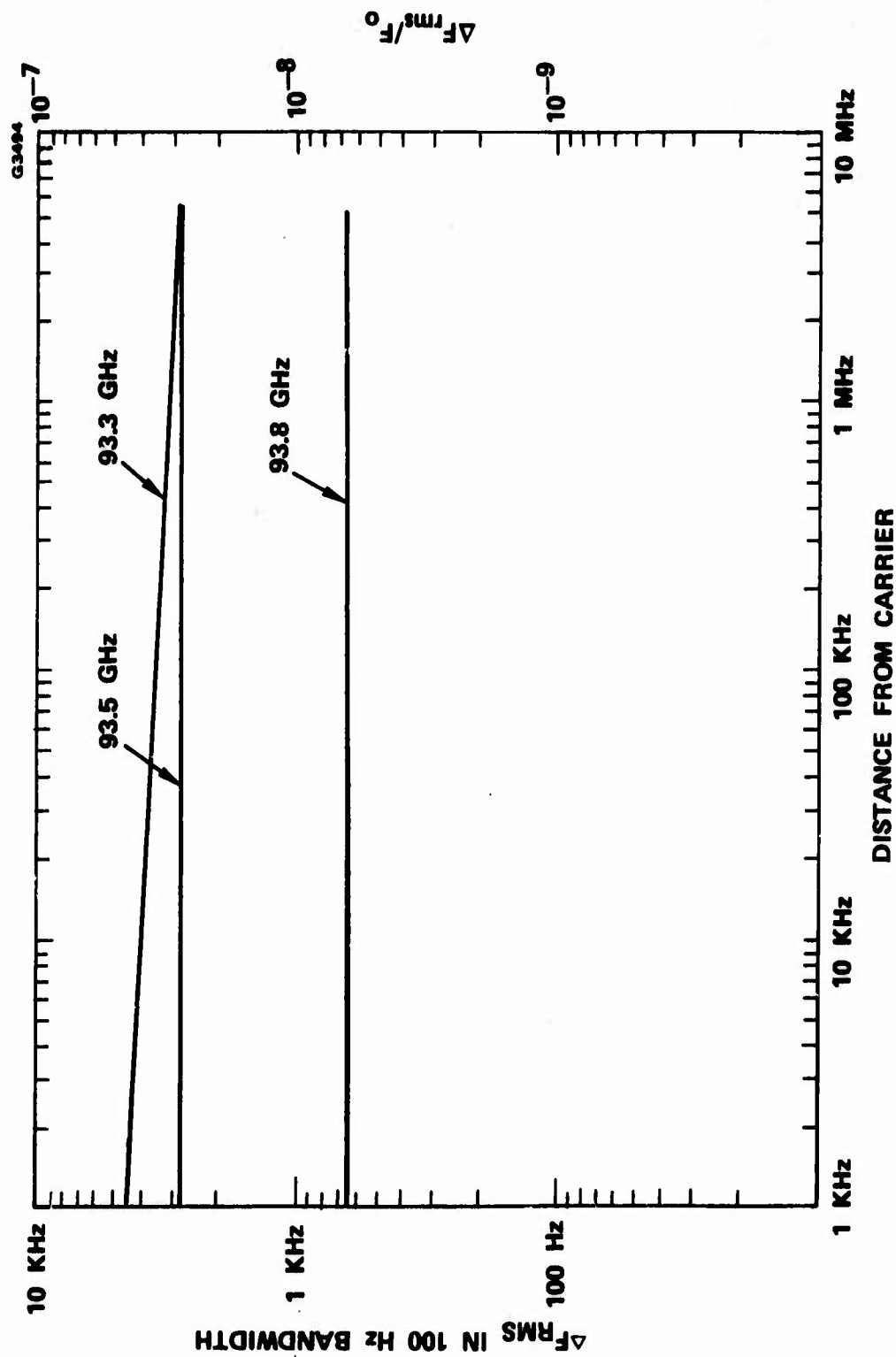


Figure 2.3-9 FM noise characteristics of FM IDTU, TO-W-A.



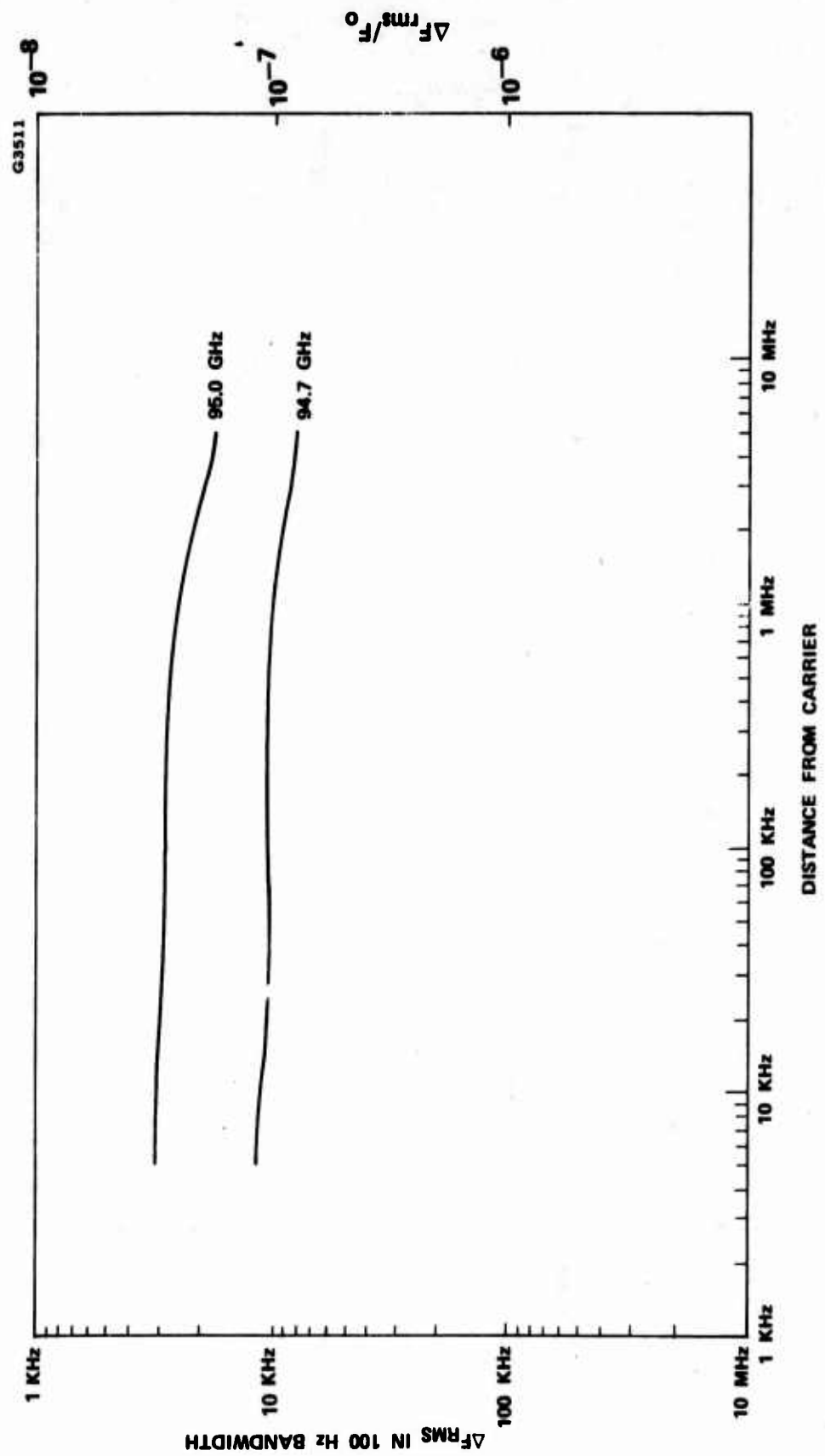


Figure 2.3-10 FM noise characteristics of FM IDTU, TO-W-B.

FM noise may be reduced, however, by reducing the bias current frequency tuning range by tuning to higher Q-factors.

Frequency variations due to ambient temperature change of TO-W-A, and TO-W-B were also measured and shown in Figure 2.3.11 and Figure 2.3.12 respectively. The results are very similar, about  $17 \text{ MHz}/^{\circ}\text{C}$ .

A photograph of the 94 GHz transmitter oscillator unit TO-W-B is shown in Figure 2.3-13. A ferrite Y-function circulator terminated at one port was used as isolator with an insertion loss of about 0.7 dB. The picture shows the regulator/modulator circuit box mounted with the IMPATT oscillator onto a finned heatsink.

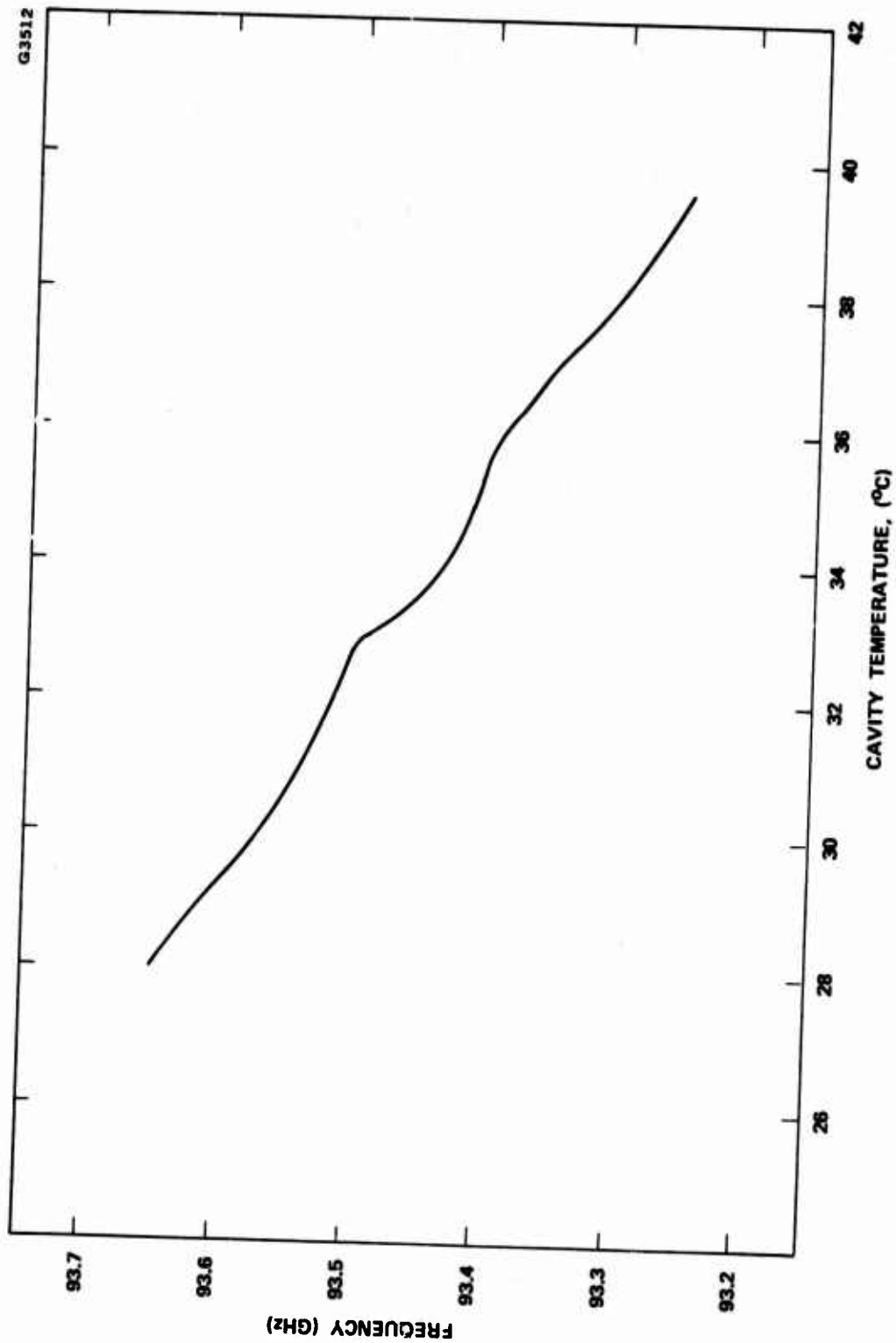


Figure 2.3-11 Frequency shift as a function of ambient temperature variation of 94 GHz FM IDTU, TO-W-A.

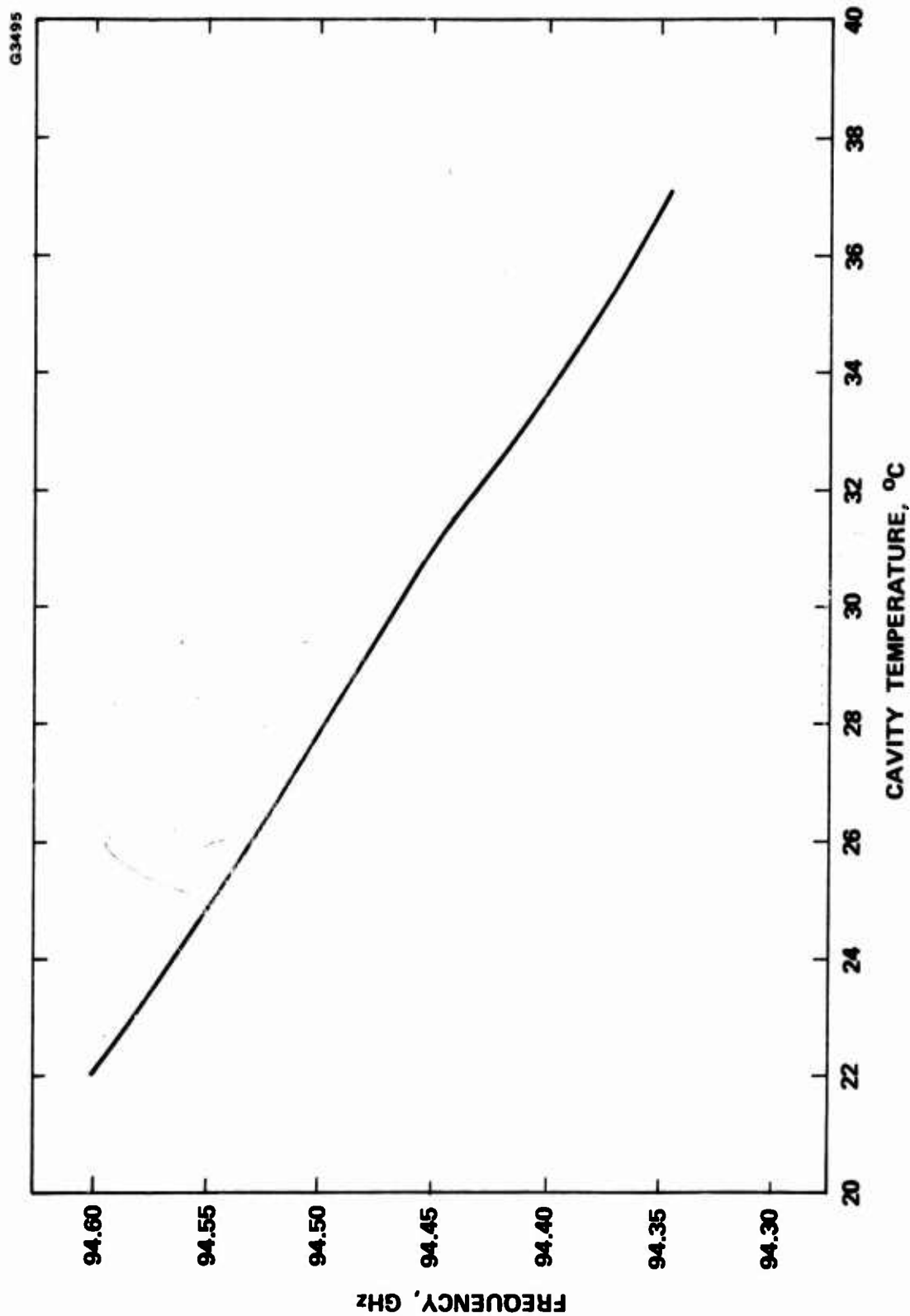


Figure 2.3-12 Frequency shift as a function of ambient temperature variations of 94 GHz FM IDTU, TO-W-B.

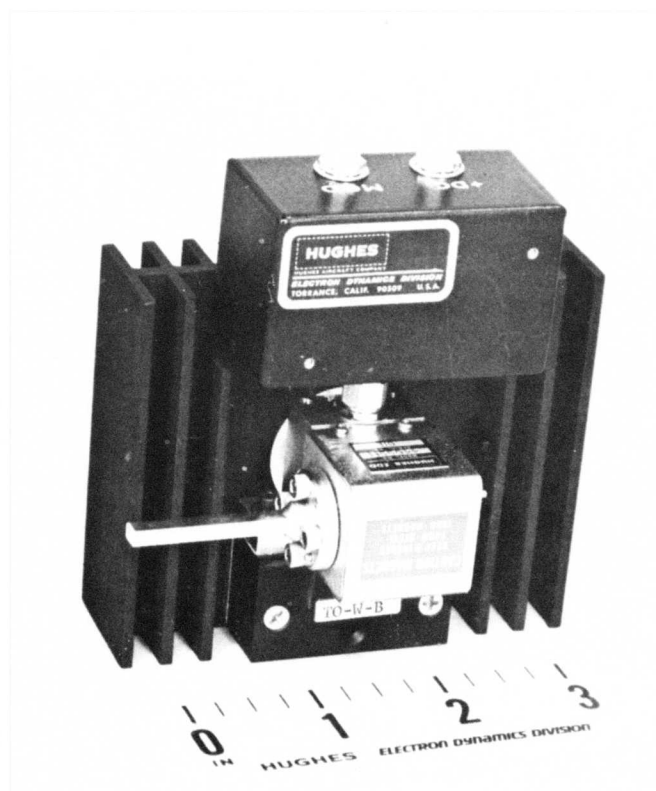


Figure 2.3-13 Photograph of the unit TO-W-B.

### 3.0 LOW NOISE IMPATT DIODE LOCAL OSCILLATORS DEVELOPMENT

#### 3.1 VARACTOR TUNED OSCILLATORS (VTOs)

##### Circuit Description

The VTO circuits have been qualitatively analyzed by several authors without taking into consideration the position of the mechanical tuning short and by assuming high Q-factors for the varactor diodes.<sup>19,20,21</sup> A simplified equivalent circuit model with the tuning short is shown in Figure 3.1-1. The oscillation frequency can be determined by noting

$$Y_D + Y_L = 0$$

where

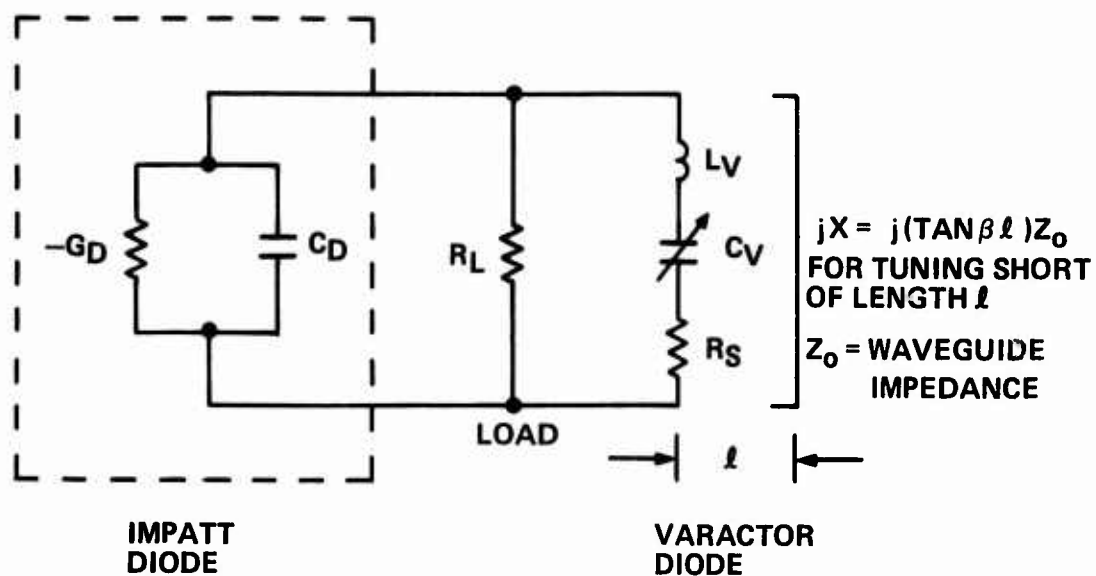
$$Y_L = \frac{1}{R_L} + \frac{1}{R_S + j(\omega L_V - \frac{1}{\omega C_V})} - j \frac{1}{X}$$

$$Y_D = G_D + j\omega C_D$$

$\omega$  = angular frequency

From the imaginary part of the above equations, one can see that

$$K^2 - \frac{1}{\left(\frac{C_D}{C_V} - \frac{R_S}{X} Q_V\right)} K + \frac{1}{Q_V^2} = 0$$



IMPATT DIODE:  $G_D$  NEGATIVE CONDUCTANCE  
 $C_D$  CAPACITANCE

VARACTOR DIODE:  $L_V$  POST INDUCTANCE  
 $C_V$  CAPACITANCE, VOLTAGE TUNABLE  
 $R_S$  SERIES RESISTANCE

LOAD:  $R_L$  LOAD RESISTANCE

OTHER DIODE PACKAGE PARASITICS NEGLECTED

Figure 3.1-1 Simplified equivalent circuit of VTO.

where

$$K = (\omega^2 C_V L_V - 1)$$

$$Q_V = \frac{1}{\omega C_V R_S} \quad \begin{array}{l} \text{varactor diode} \\ \text{Q-factor} \end{array}$$

At 60 GHz, for a typical GaAs varactor diode of zero bias voltage capacitance of 0.14 pf and  $R_S = 1$  ohm,  $Q_V = 18.93$  so that the quality factor of varactor diodes at millimeter-wave frequencies is not high compared with lower microwave frequency diodes.

The solution to K, which, in turn, determines the oscillation frequency  $\omega$ , can be written as

$$K = \frac{1}{2} \left( \frac{C_D}{C_V} - \frac{R_S}{X} Q_V \right) \left[ 1 \pm \left\{ 1 - \frac{4}{Q_V^2} \left( \frac{C_D}{C_V} - \frac{R_S}{X} Q_V \right)^2 \right\}^{1/2} \right]$$

For oscillation to occur, the condition

$$\frac{Q_V}{2} \geq \left| \frac{C_D}{C_V} - \frac{R_S}{X} Q_V \right|$$

is required. This condition clearly sets a tuning range for the tuning short for proper oscillations, i.e.,

$$\frac{\frac{R_S Q_V}{C_D} - \frac{Q_V}{2}}{\frac{C_D}{C_V} - \frac{Q_V}{2}} \geq X \geq \frac{\frac{R_S Q_V}{C_D} + \frac{Q_V}{2}}{\frac{C_D}{C_V} + \frac{Q_V}{2}}$$



For a typical VTO, constructed at 60 GHz,  $C_D \sim 1.6$  pf,  $C_V \sim 0.14$  pf,  $R_S \sim 1$  ohm and  $Q_V \sim 18.93$ , the value for X is restricted to

$$9.64 \geq X \geq 0.906 \text{ ohms}$$

This indicates that the tuning short needs to be placed very close to the varactor diode and can have but a very narrow tuning range. This was indeed qualitatively observed for our 60 GHz VTOs.

The frequency tuning bandwidth BW can be obtained from

$$\omega = \left[ \frac{1 + K}{L_V C_V} \right]^{1/2}$$

so that

$$BW = \frac{1}{\sqrt{L_V}} \left\{ \left[ \frac{1 + K}{C_V} \right]_{V_B}^{1/2} - \left[ \frac{1 + K}{C_V} \right]_0^{1/2} \right\}$$

where  $V_B$  = varactor breakdown voltage and the subscript "0" for zero bias voltage.

The power dissipated in the circuit,  $P_V$ , other than in the load,  $R_L$ , and the power dissipated in  $R_L$ ,  $P_L$ , can be written as

$$\frac{P_V}{P_L} = \frac{R_L}{R_S} \left\{ \frac{\left( 1 + K \frac{R_S}{X} Q_V \right)^2 + \left( \frac{R_S}{X} \right)^2}{1 + (KQ_V)^2} \right\}^{1/2}$$

Hence the varactor circuit will degrade the oscillator power  $P_D$  by the relationship

$$P_L = \frac{P_D}{1 + \frac{P_V}{P_L}}$$

For  $R_L \approx 1/G_D \sim 5$  ohms,  $X \approx 9$  and  $K \approx 0.062$ , we expect an output power degradation in the order of 6 dB, which is close to what we have observed.

The VTO waveguide cavity circuit is shown in Figure 3.1-2. The mounting of the IMPATT and varactor diodes on the opposite faces of the waveguide broadwalls has the advantage that the two diodes can be placed close to each other, within one half of wavelength, for the desired coupling. Furthermore, this also allows the replacement of the diodes separately.

#### GaAs Varactor Diode

The  $p^+-n-n^+$  mesa structure GaAs varactor diodes were used for this program at 60 GHz. The diodes were placed in a quartz ring package with full strap gold ribbon connecting the diode to the top of the quartz ring. The configuration and dimensions of the varactor diodes are similar to the IMPATT packages shown earlier in Figure 3.1-2. A typical diode capacitance as a function of reverse bias voltage of a GaAs varactor diode is shown in Figure 2.3-3. This diode has a  $R_S = 2$  ohms, and breakdown voltage of 10.5 volts. The cut-off frequency of the diode is estimated as 500 GHz. The diode has a capacitance ratio between zero bias and bias near breakdown of 2.67 with zero bias capacitance at 0.16 pf. The quartz ring package has a measured capacitance 0.03 pf. Therefore, the capacitance ratio, without package should be somewhere near 4.0.

	Dimensions, Inches		
	A	B	C
V-BAND	.074	.025	.060
W-BAND	.050	.010	.060

G2644

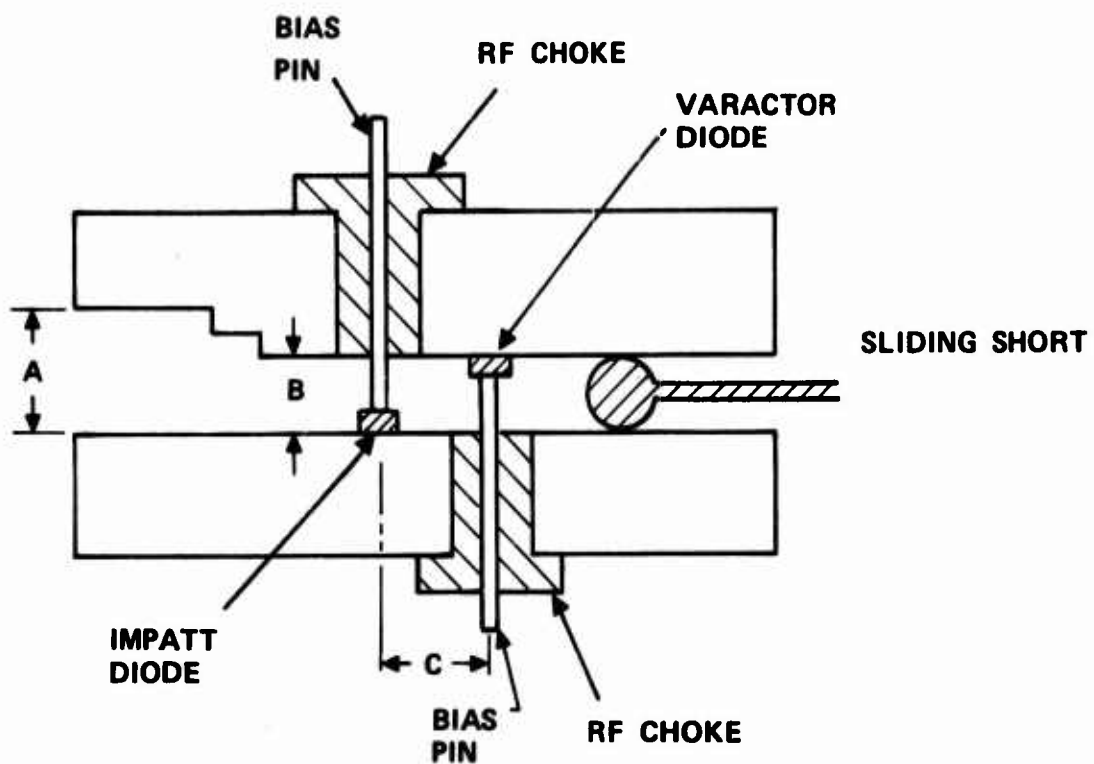


Figure 3.1-2 VTO reduced height waveguide circuit.

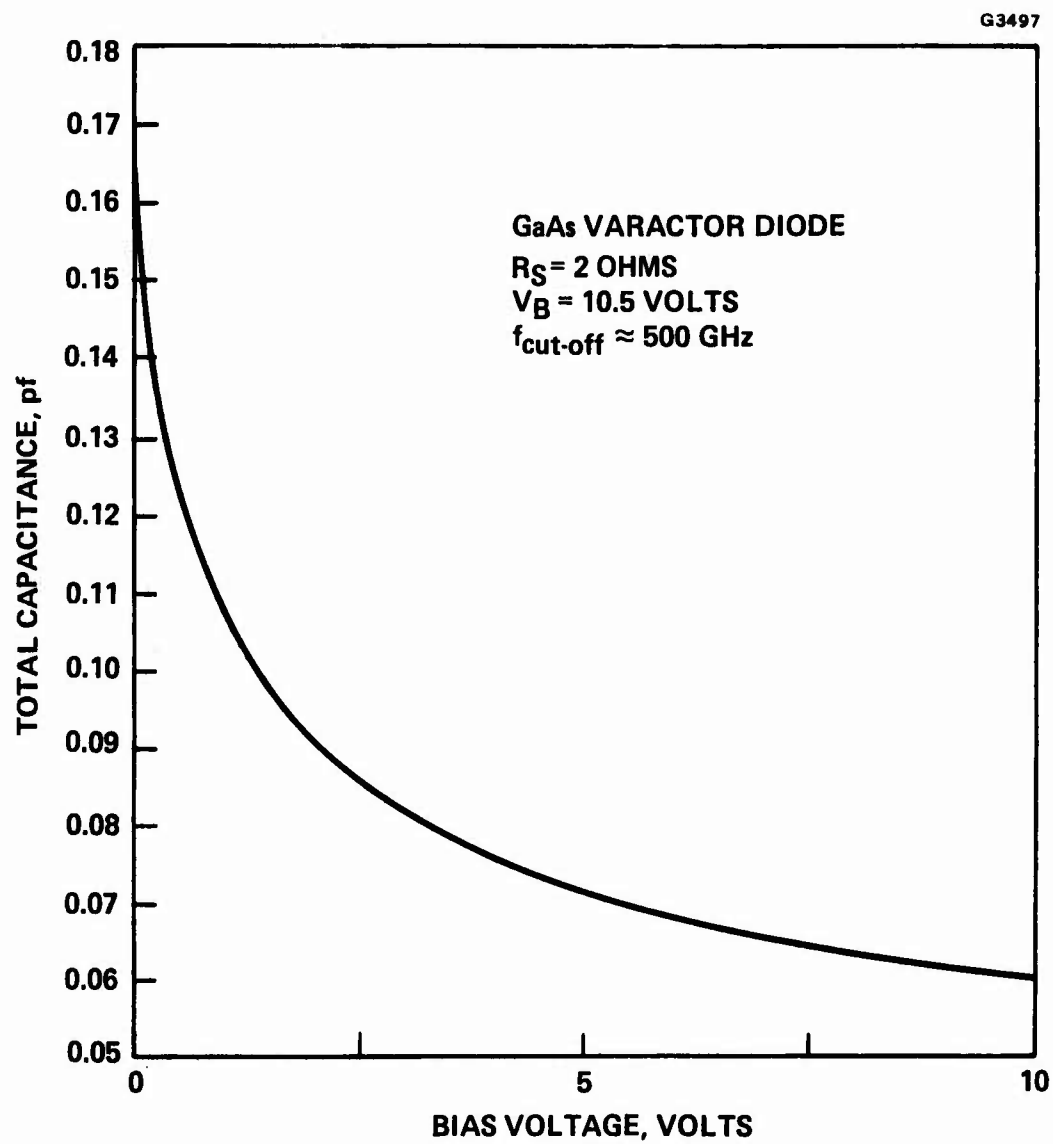


Figure 3.1-3 C-V characteristics of a GaAs mesa varactor diode.

In the next section, the experimental results of the VTOs will be discussed.

### 3.2 60 GHz LOW NOISE LOCAL OSCILLATOR UNITS (LNLOUs)

The 60 GHz LNLOUs, using a varactor diode for tuning the frequency of the local oscillators, were developed to match the 60 GHz FM IDTUs for transmitter and receiver application. This section presents our data on the tuning characteristics, AM noise characteristics, and temperature effect on the frequency shift of two LNLOUs, LO-V-A and LO-V-B.

Figure 3.2-1 and Figure 3.2-2 are the tuning characteristics of the varactor tuned local oscillator LO-V-A, and LO-V-B respectively. For the unit LO-V-A, the varactor diode used was a single-drift IMPATT diode of  $p^+-n-n^+$  doping profile in a quartz ring package. It was etched to a total capacitance (package plus diode at zero voltage) of 0.65 pf. The total capacitance ratio between zero bias and reverse bias near breakdown is about 2.5:1. The IMPATT diode used as oscillator was also a single-drift IMPATT diode. It has a thermal impedance of  $27^{\circ}\text{C/W}$  and operated at  $246^{\circ}\text{C}$  junction temperature. The unit has a voltage tuning range of 3.2 GHz with output power mostly between 30 mW and 40mW. The highest output power of 46 mW occurred at zero bias of the varactor.

For the unit LO-V-B, a GaAs  $p^+-n$  junction mesa diode was used as varactor diode as discussed earlier in Section 3.1.

The diode has a breakdown voltage of 10 volts with a total, package plus diode at zero bias, capacitance of 0.23 pf. The capacitance ratio of the varactor between zero bias and bias near breakdown is about 2:1.

For the oscillator, a single-drift IMPATT diode of  $p^+-n-n^+$  doping profile was used. The diode was operated at a junction temperature of

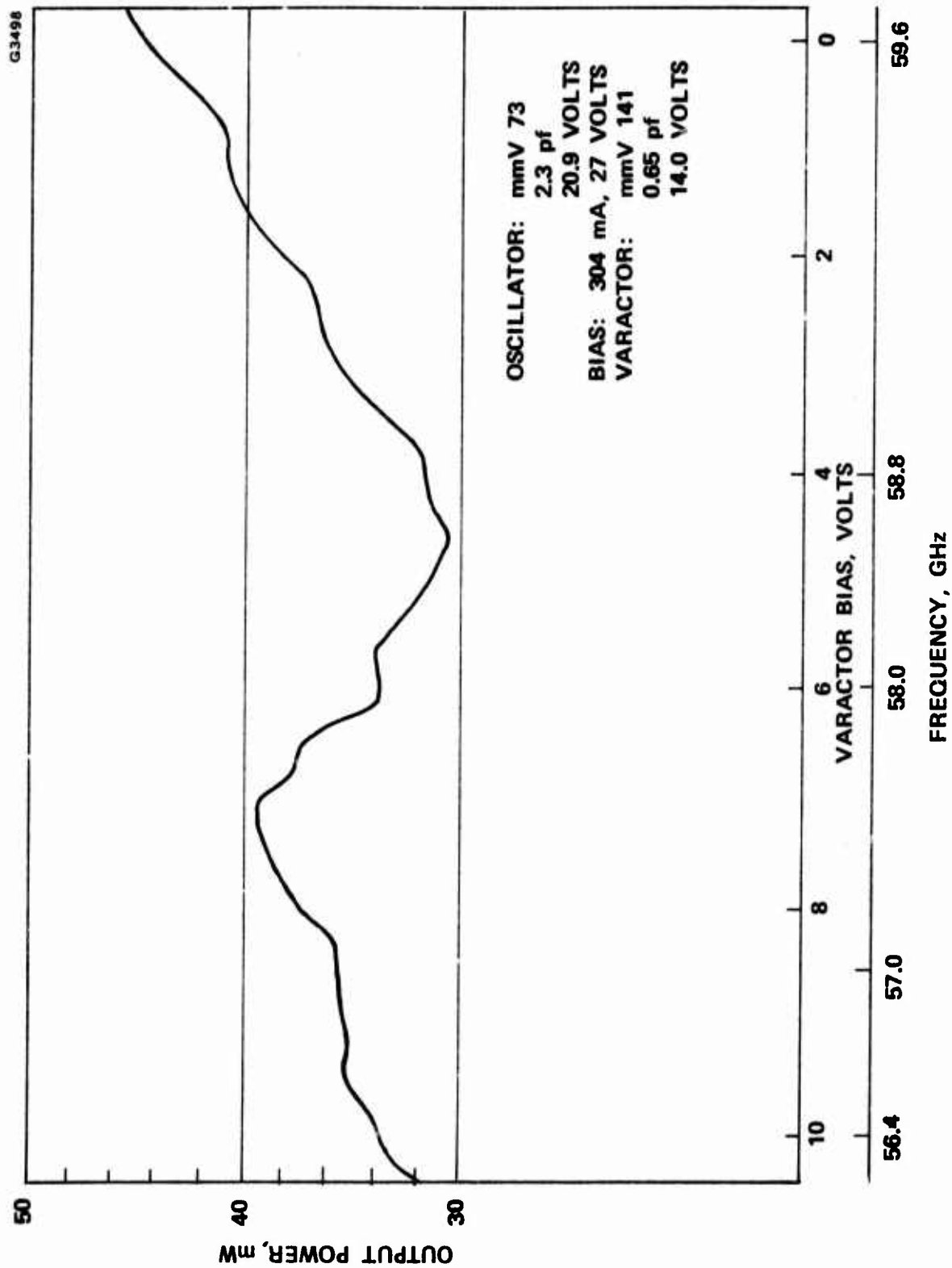


Figure 3.2-1 Tuning characteristics of the 60 GHz LN LO-V-A.

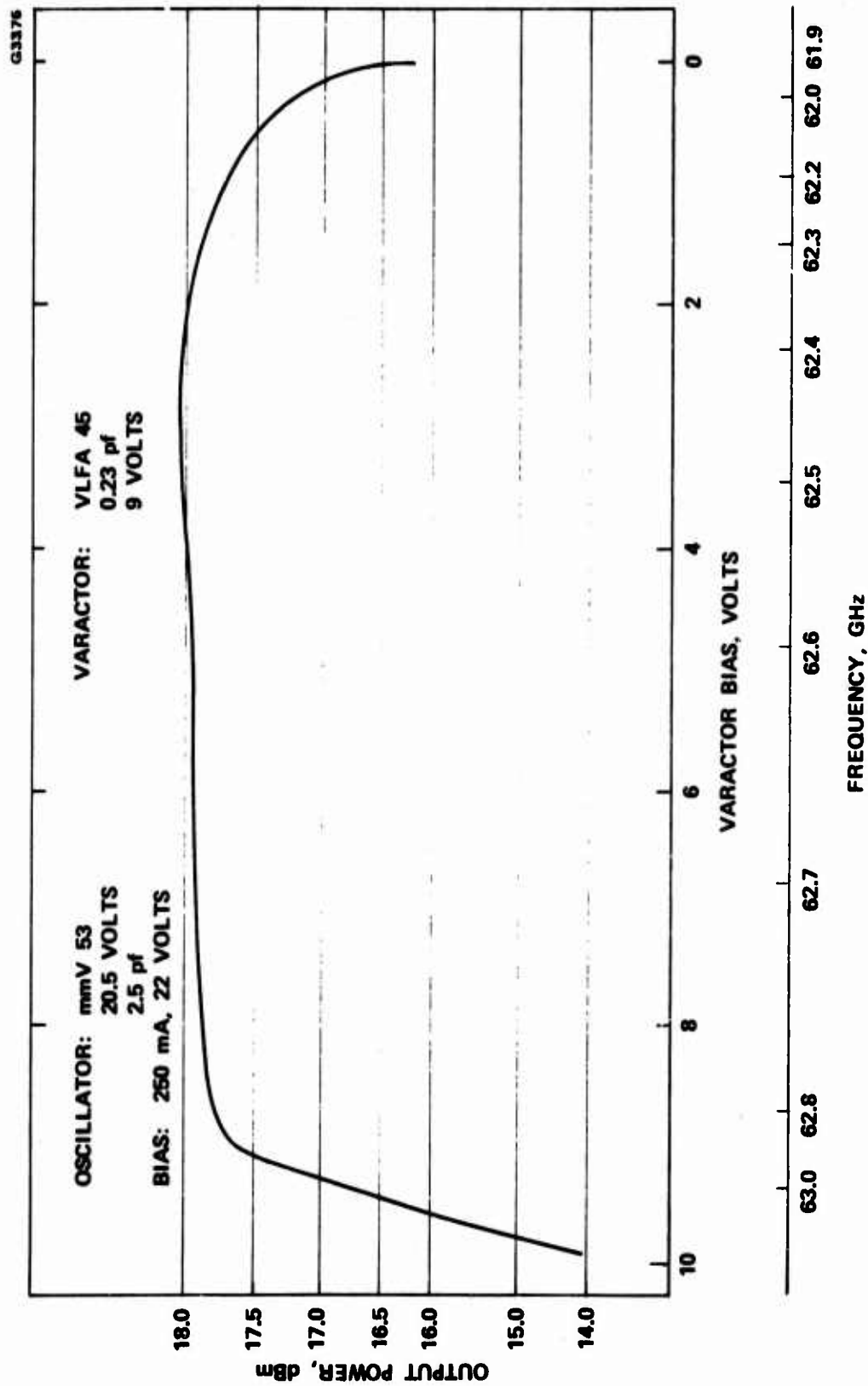


Figure 3.2-2 Tuning characteristics of the 60 GHz LN LOU, LO-V-B.

170°C with a tuning range of about 1 GHz and with output power variations less than 1 dB. Maximum output power was +18 dBm as shown in Figure 2.3-2.

The unit LO-V-B which uses a GaAs varactor as tuner shows a frequency increase with the bias voltage. This is predicted since for  $K \approx 0$ , the oscillator frequency

$$\omega \sim \frac{1}{\sqrt{L_V C_V}}$$

With  $C_V$  decreasing with bias voltage, the oscillator frequency will increase as shown. However, for the unit LO-V-A, the opposite happened with the frequency decreasing with an increase of bias voltage. This perhaps was determined by the external circuit of the oscillator. The tuning bandwidth was less than theoretically predicted because of the various diode package and mounting parasitics. The output power of the units was more than sufficient for local oscillator applications.

Double sideband AM noise of LO-V-A and LO-V-B are shown in Figure 3.2-3 and 3.2-4 respectively. The unit LO-V-B which operated at lower junction temperature had better noise performance compared with the unit LO-V-A. The noise at 1.5 GHz away from carrier is again worse than near carrier (60 MHz from carrier) noise because of the RF choke design, discussed earlier, that was not able to suppress bias circuit induced oscillations which generate noise sidebands.

Noise performance of VTOs are in general improved over bias current modulated IMPATT oscillators because good bias current regulation can be provided for the VTOs to minimize near carrier noise.



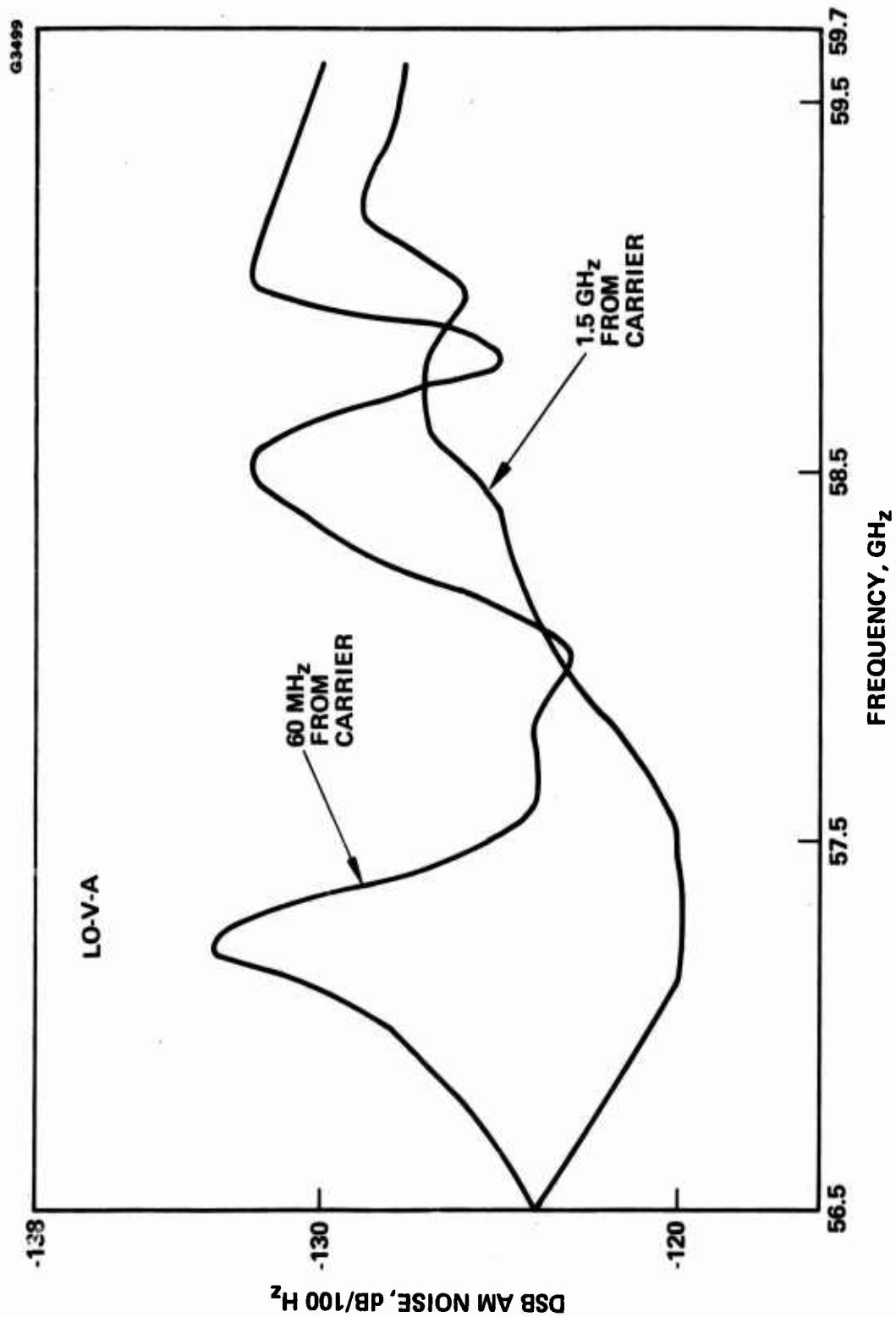


Figure 3.2-3 AM noise characteristics of the 60 GHz LN LOU, LO-V-A.

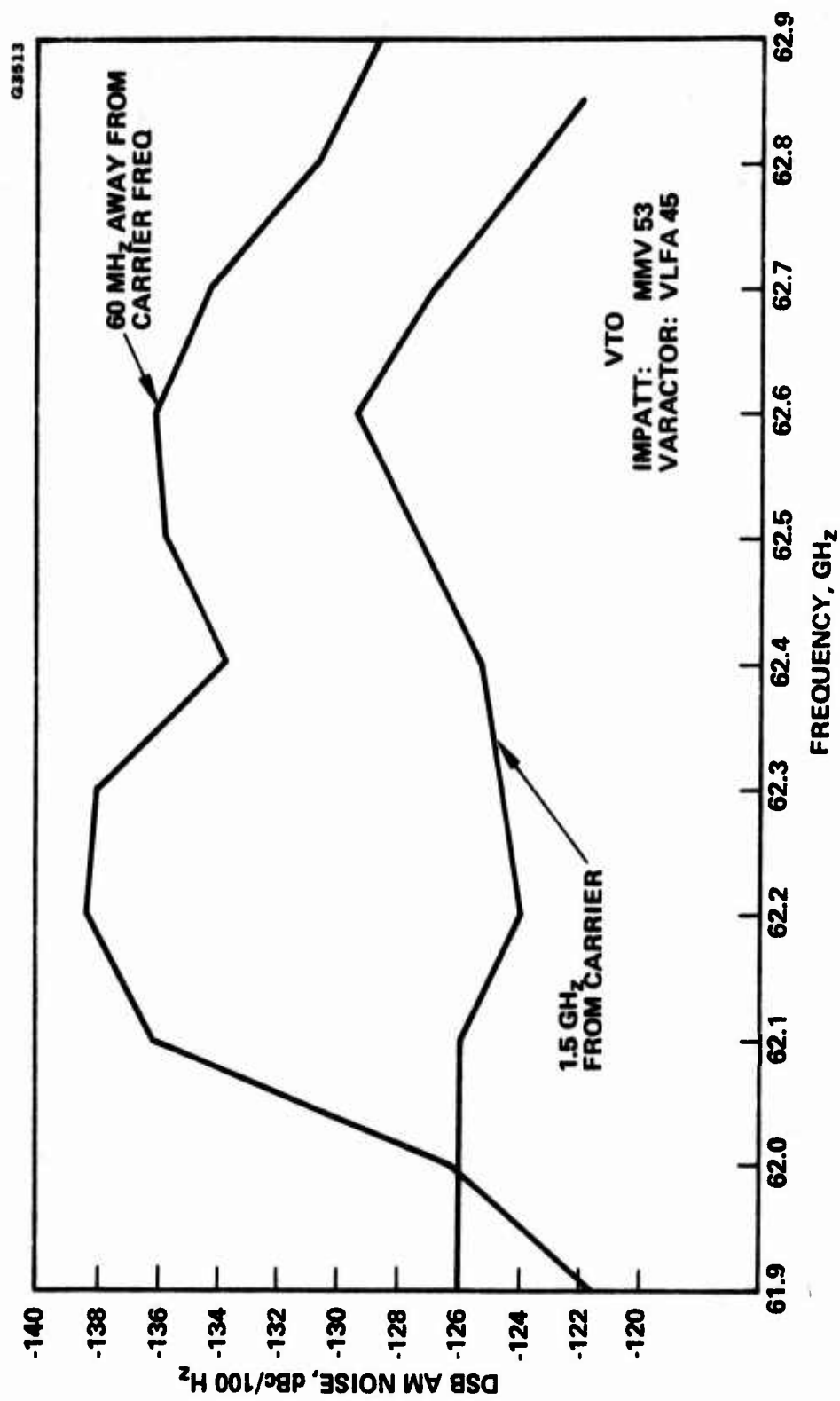


Figure 3.2-4 AM noise characteristics of the 60 GHz LN LOU, LO-V-B.

Since the receiver designed for system evaluation of this program operated at an i.f. centered at 1.5 GHz, the VTOs AM noises at 1.5 GHz from carrier is of major concern. The results shown in both Figure 3.3-2 and 3.3-3 indicate that the VTOs can be used with balanced mixers with 27 dB LO noise suppression without generating excess receiver noise figures.

#### Frequency Shift Characteristics Due to Ambient Temperature Change

The LO-V-A and LO-V-B shifted their operation frequency when the ambient temperature of the oscillators shifted. For VTOs, however, the temperature shift can be caused by both IMPATT diodes and varactor diodes. We have measured this effect for the units LO-V-A, and LO-V-B as shown in Figure 3.2-5 and 3.2-6 respectively. The best results are around 10 MHz/°C which is not as good as the cavity stabilized oscillators as expected because of the low Q-factor circuit we used.

### 3.3 94 GHz LOW NOISE LOCAL OSCILLATOR UNITS (LNLOUs)

#### Tuning Characteristics

The 94 GHz LNLOUs were also constructed using VTOs. The varactor diodes used were silicon IMPATT diodes etched to small junction areas. Figure 3.3-1 is the voltage tuning characteristics of the unit LO-W-A. The varactor diode is a silicon single-drift IMPATT diode of 0.79 pf in capacitance and 11.0 volts breakdown voltage. The oscillator diode is also a single-drift IMPATT diode of 14.4 volts breakdown voltage and 1.6 pf capacitance. It operated at a junction temperature of 225°C.

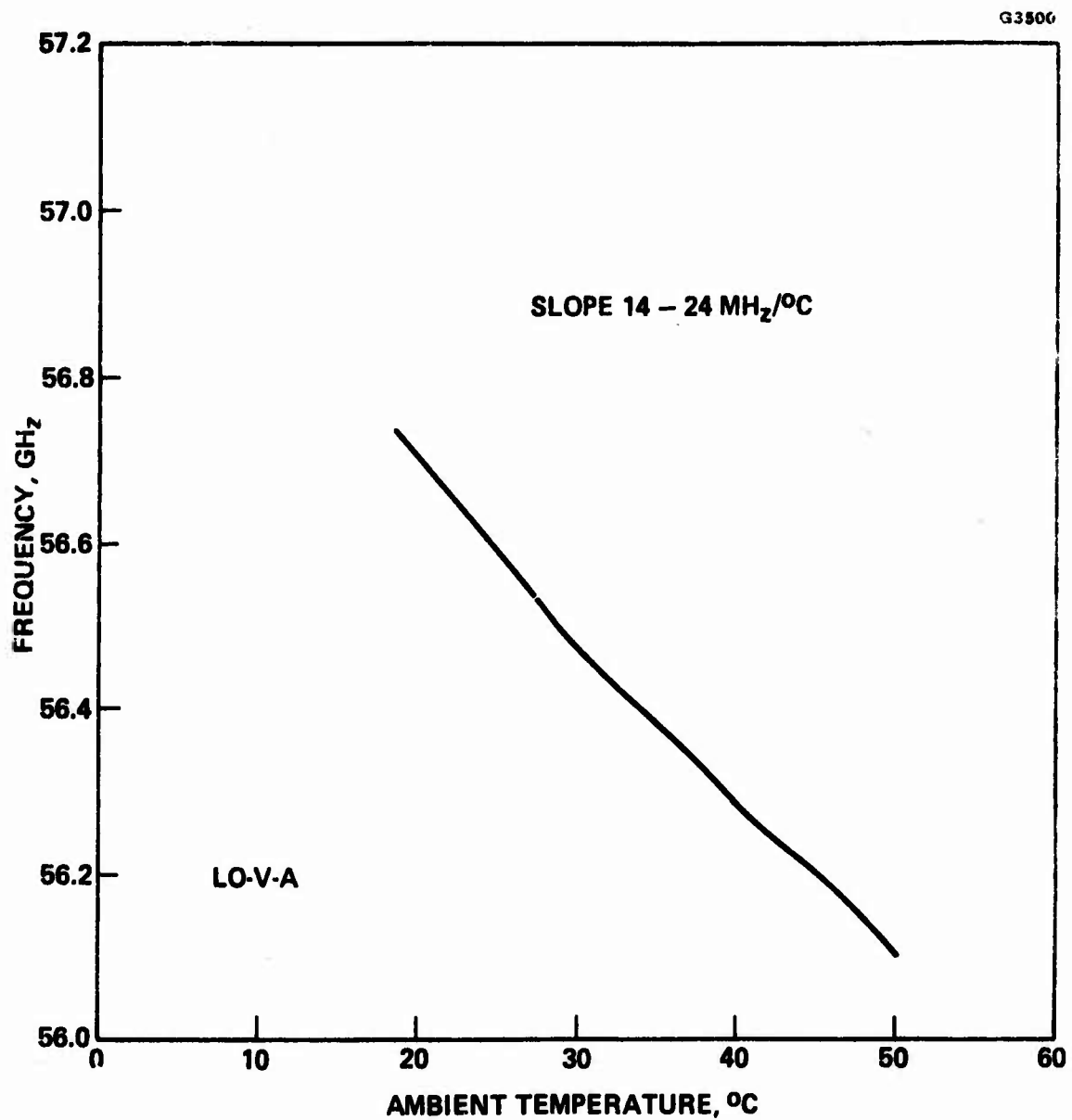


Figure 3.2-5 Temperature effect on the oscillator frequency shift, LO-V-A.

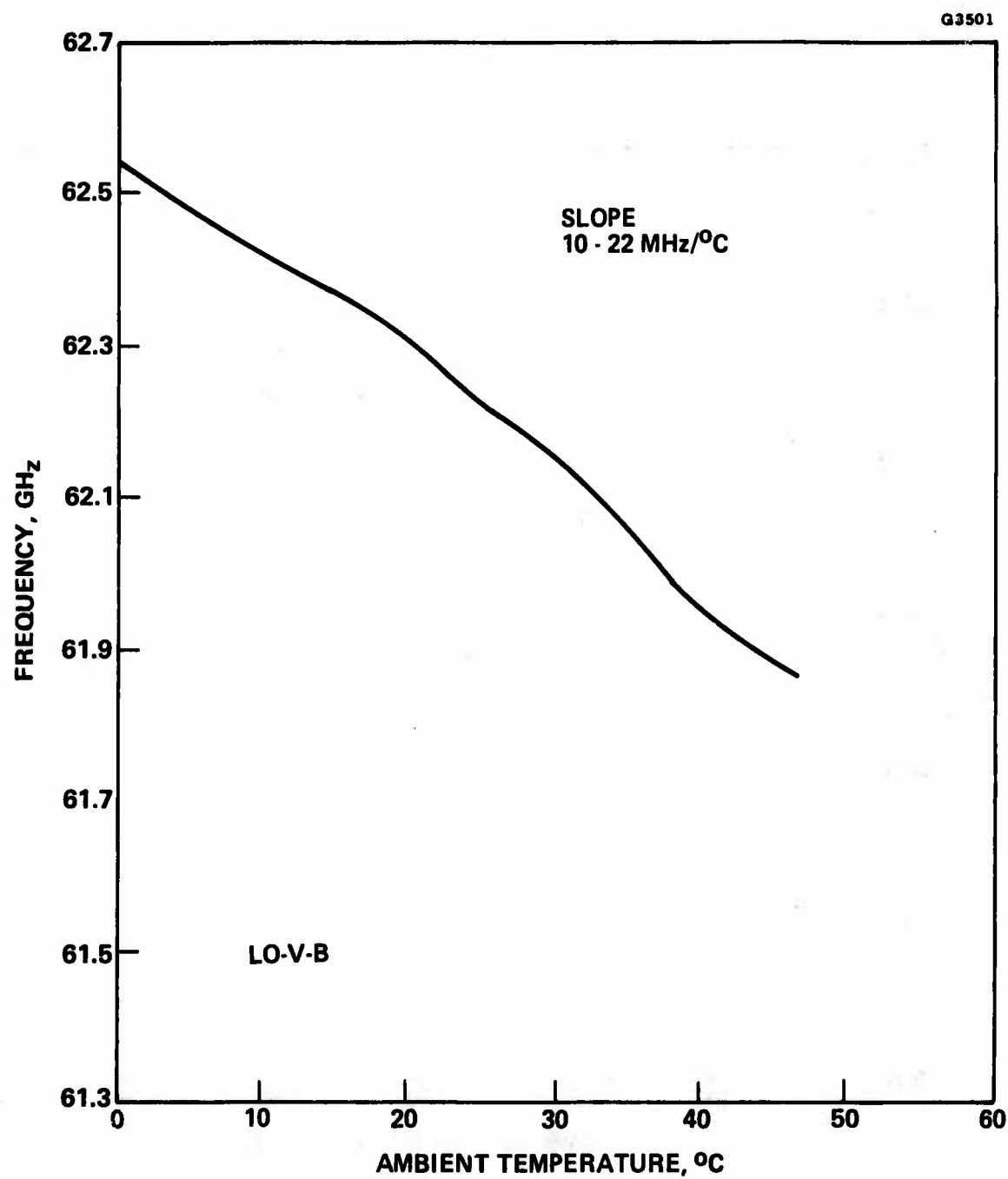


Figure 3.2-6 Temperature effect on the oscillator frequency shift, LO-V-B.

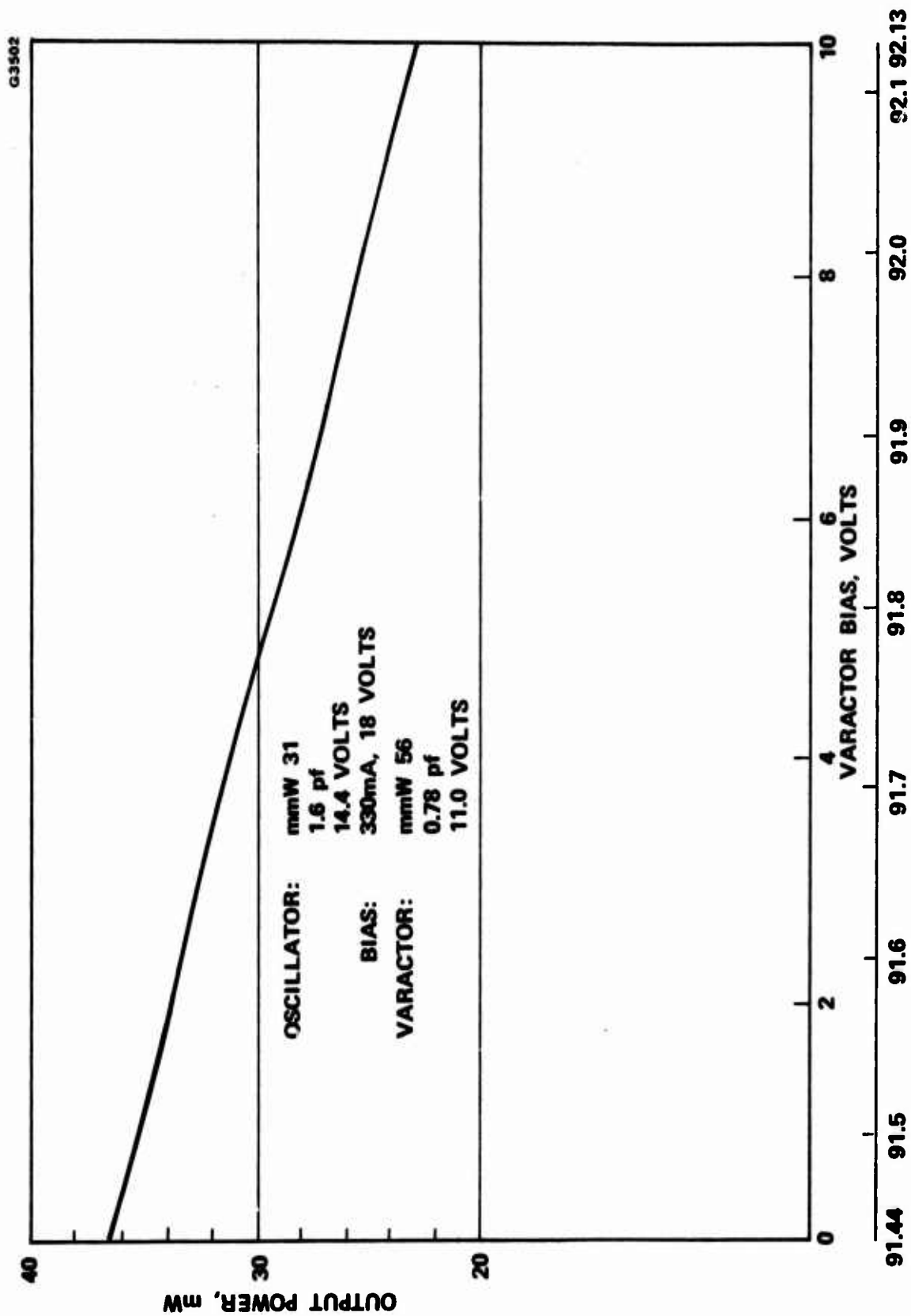


Figure 3.3-1 Tuning characteristics of the 94 GHz VTO, LO-W-A.

The oscillator frequency increases from 91.44 GHz to 92.13 GHz over a 700 MHz range. Output power of the unit varies from 36 mW to about 24 mW in the tuning range. The drop in output power with bias voltage indicates losses in the varactor diode at these frequencies. The second VTO unit, LO-W-B, also used a silicon single-drift IMPATT diode as a varactor. The varactor diode has 13.92 volts breakdown voltage, and 0.69 pf capacitance. The oscillator diode has 12.5 volts breakdown voltage and 1.5 pf capacitance. The voltage tuning range shown in Figure 3.3-2 is over 1 GHz from 93.0 to 94.15 GHz. The output power of LO-W-B is higher than that of LO-W-A. Maximum output power of 52 mW was achieved.

The output power of LO-W-A and LO-W-B reported in Figure 3.3-1 and 3.3-2 respectively included an integral isolator for each unit with loss of about 1 dB. Therefore the output power shown there should be added about 20% more as the actual output power of the VTOs.

#### Noise Characteristics

Double sideband AM noise characteristics of the unit LO-W-A, and LO-W-B have also been measured and shown in Figure 3.3-3 and 3.3-4 respectively. The noise for both oscillators was of the same order of magnitude, varied between -126 dBc/100 Hz and -133 dBc/100 Hz. The noise at near carrier and at 1.5 GHz from carrier were also about the same in magnitude. The noise characteristics were quite typical of IMPATT oscillators properly behaved.

Figure 3.3-5 is a picture of the unit LO-W-A. A ferrite isolator (Faraday Rotation type) was attached to the VTO cavity to prevent frequency pulling by the external load mismatch. The isolators cover the full waveguide band frequencies and with isolations about 30 dB typical.

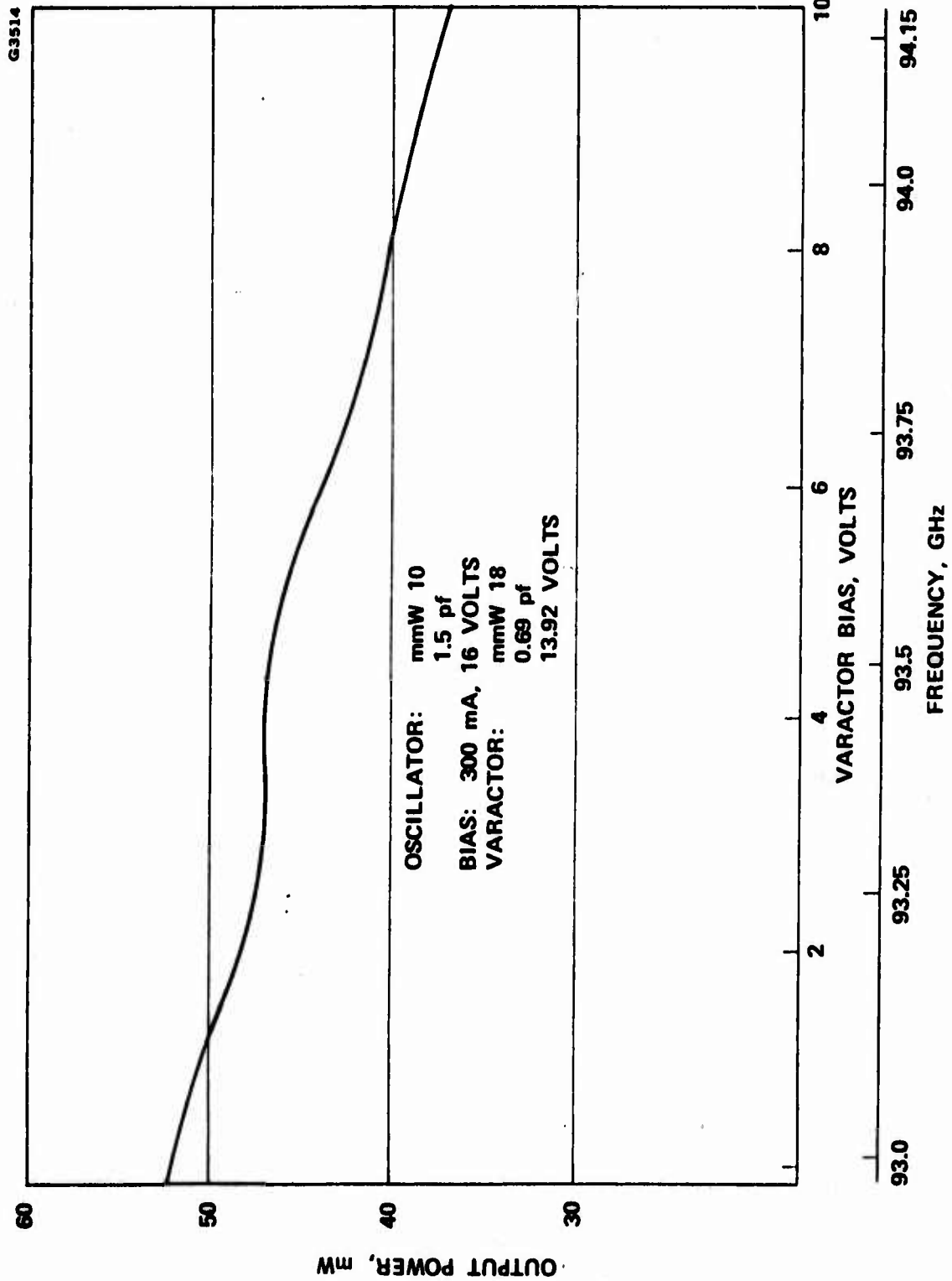


Figure 3.3-2 Tuning characteristics of the 94 GHz VTO, LO-W-B.



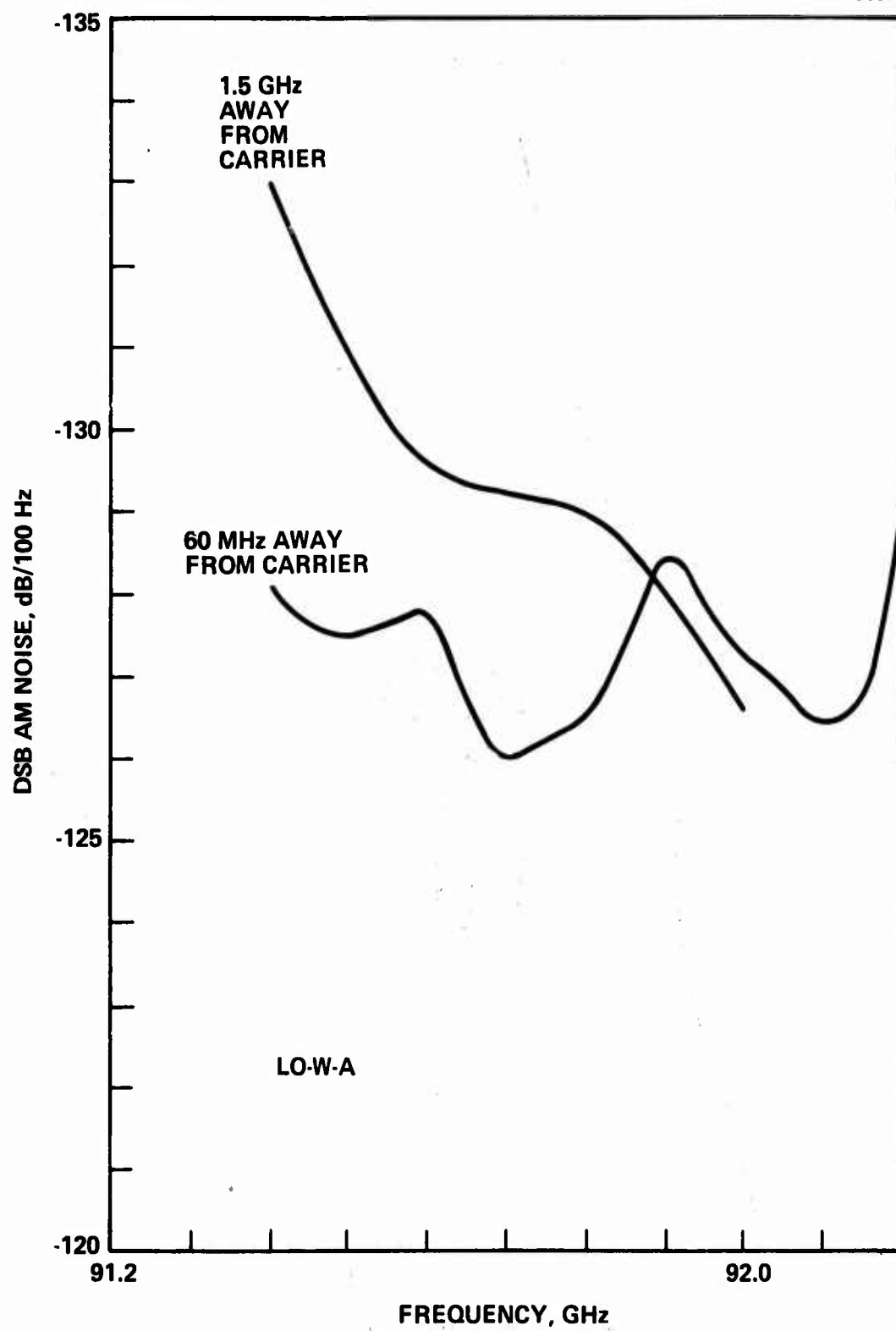


Figure 3.3-3 DSB AM noise of the 94 GHz VTO, LO-W-A.

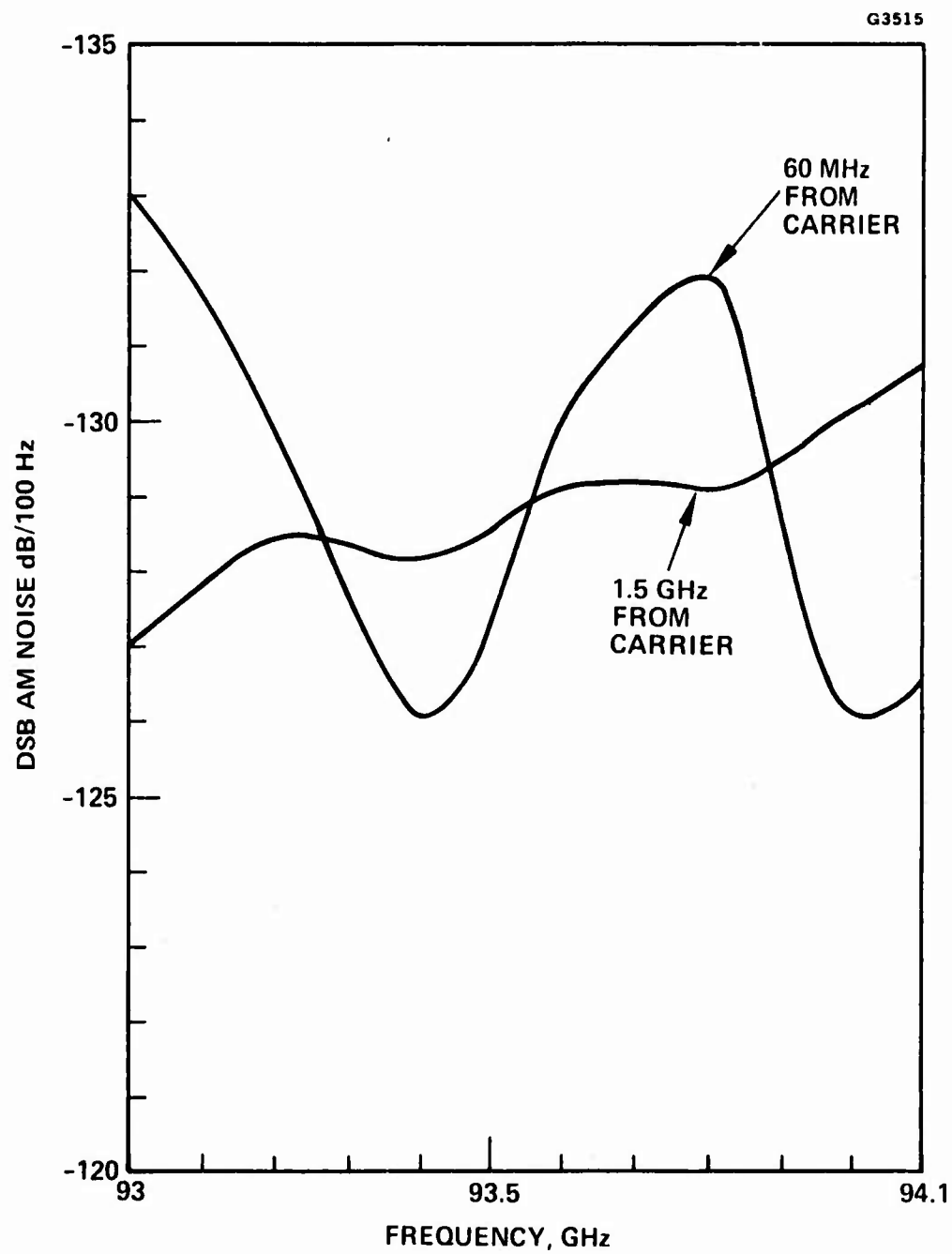


Figure 3.3-4 DSB AM noise of the 94 GHz VTO, LO-W-B.

E1177

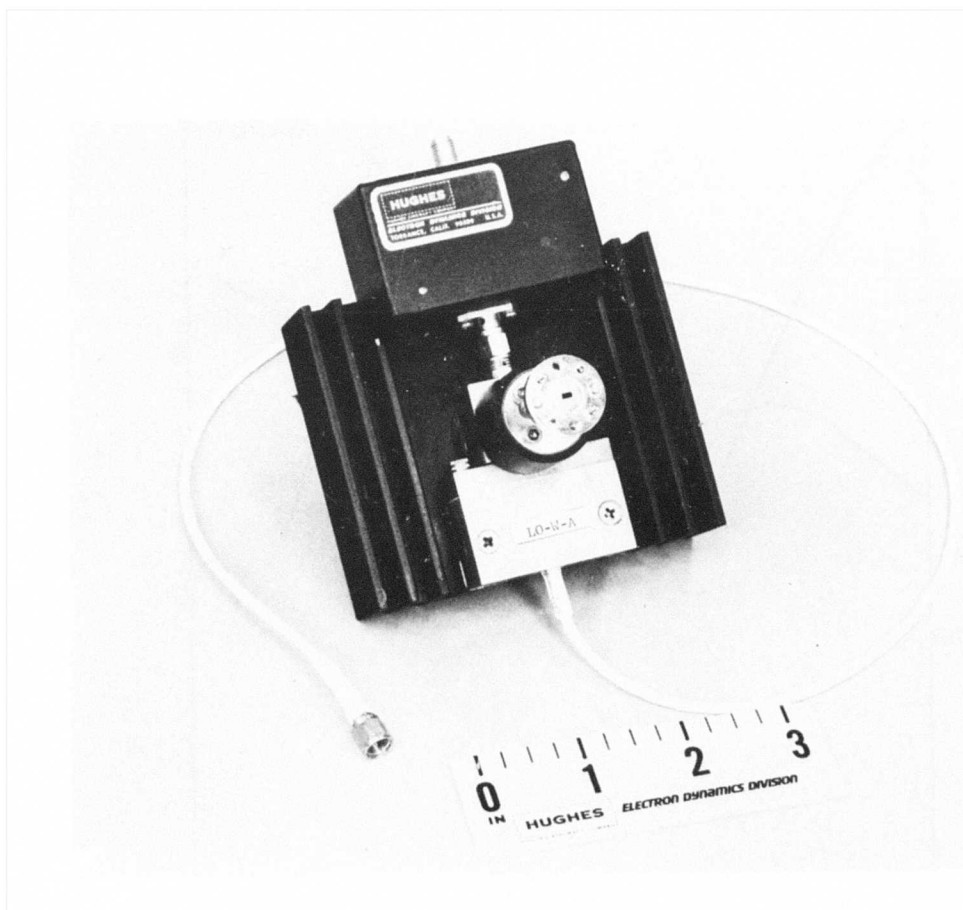


Figure 3.3-5 Photograph of a VTO unit (LN LOU).

The IMPATT diode was current regulated through a regulator circuit box while the varactor diode was biased through the bottom heat sink of the oscillator as shown in the figure. Again, the unit has a heat sink allowing it to be operated without cooling fans. The regulator circuit is identical to the regulator/modulator circuit presented later in Figure 4.1-2, except with the elimination of the modulator portion of the regulator/modulator circuit.

#### 4.0 SYSTEM PERFORMANCE EVALUATION

The goals of this program were to develop 60 GHz and 94 GHz solid state transmitter oscillators and local oscillators for secure and adverse weather FM communication respectively at high data rate of 100 Megabits per second and bit-error-rate (BER) of  $10^{-7}$  and less. In order to conduct system performance evaluation, a HP 3760A data generator, a HP 3761A error detector, and a HP 5055 printer were purchased as part of the test setup which includes a FM receiver developed for this program. The receiver includes AFC, search/lock, and AGC functions and a frequency discriminator centered at 1.5 GHz (i.f. frequency of the receiver).

This section first describes the system function block diagram and the various receiver circuitries developed for this program in Section 4.1. Section 4.2 describes various test results including video data output, output data frequency spectrum and bit-error-rate of the two 60 GHz transmitter-LO pairs TO-V-A/LO-VA and TO-V-B/LO-V-B and the two 94 GHz transmitter-LO pairs, TO-W-A/LO-W-A and TO-W-B/LO-W-B.

#### 4.1 SYSTEM FUNCTION BLOCK DIAGRAM AND CIRCUITS

##### Function Block Diagram

The system function block diagram for the performance evaluation of the solid state sources is shown in Figure 4.1-1. On the transmitter side, a HP3760A data generator drove an IMPATT transmitter oscillator under test through a regulator/modulator circuit. The output power of the transmitter oscillator can be either fed directly into the FM receiver, or directed into a thermistor connected to a power meter to measure the signal strength. On the receiver side, the input signal was detected with a balanced mixer- i.f. amplifier with a noise

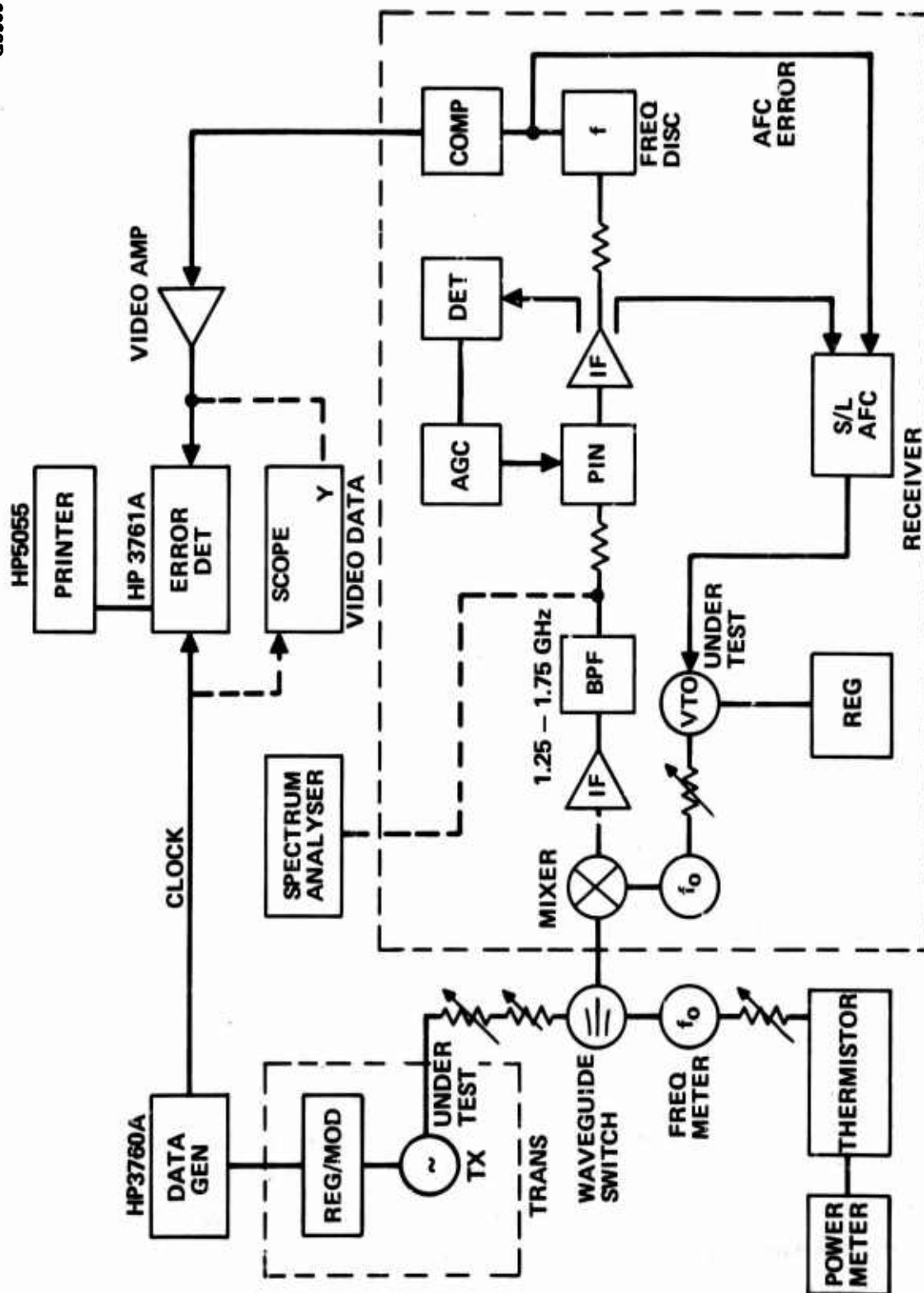


Figure 4.1-1 System block diagram.

figure of 9.5 dB at 60 GHz frequencies and 10 dB at 94 GHz frequencies. The output power of the local oscillator (VTO) under test was attenuated before input to the balanced mixer. The balanced mixer has a LO noise suppression factor of about 30 dB so that by adjusting the LO power into the mixer properly, no excess noise was generated in the receiver due to the LO noise. A bandpass filter (BPF) of 500 MHz bandwidth (1.25 - 1.75 GHz) was used following the mixer i.f. amplifier. Before the FM signal was detected by a frequency discriminator, a PIN diode attenuator and an amplifier were used to form the AGC loop so that input levels into the frequency discriminator were maintained at a fixed value. This is necessary since the voltage versus frequency linear slope of the frequency discriminator normally varies with input levels because of the discriminator detector diodes saturation characteristics. An AGC loop is favored over a hard limiter mainly because existing limiters hard limit at high power levels which are not compatible with our discriminator. Following the frequency discriminator, a comparator circuit is used so that a constant output data pulse amplitude can be maintained at and beyond the signal threshold. The output of the comparator was then amplified with a wideband video amplifier to drive the HP3761A error detector, or to display the video data pulses on a scope. The data spectrum output can also be displayed on a spectrum analyser by sampling at the BPF output. The AFC, search/lock function was provided by sampling the incoming signal at the AGC output and at the frequency discriminator output for AFC error. When in the search mode, the AGC output was below the limiting value. A ramp voltage was activated to drive the VTO for searching for the incoming signal. Detection of the signal after the AGC disengages the search, and locks the VTO onto the signal with the AFC error correction using the frequency discriminator output.

The i.f. bandwidth of 500 MHz (1.25 GHz - 1.75 GHz) was sufficient for 100 megabits per second data reception. According to the rule of thumb

relationship for a FM system, the i.f. bandwidth, B, required can be estimated from

$$B = 2 (\beta + 1) f_m$$

Where  $f_m$  is the modulation frequency,  $\beta = \Delta f / f_m$  is the index of modulation and  $\Delta f$  is the frequency deviation from carrier. For a 100 Megabit return-to-zero (RZ) data rate or a 200 Megabits non-return-to-zero (NRZ) data rate,  $f_m = 100$  MHz. For a fixed  $\Delta f = 100$  MHz, we need  $B = 400$  MHz. Add 100 MHz as guard band, and a bandwidth of 500 MHz is then sufficient for system evaluation. The balanced mixer- i.f. amplifier has a noise figure of 10 dB, using the VTO as LO. Therefore, the system noise floor is estimated to be -77 dBm per 500 MHz. We should expect to detect a signal of between -67 dBm and -62 dBm taking into consideration the FM detection threshold of between 10 and 15 dB, which should achieve a bit-error-rate (BER) of  $10^{-7}$  or better. Since the transmitter oscillator output power of +26 dBm at 60 GHz and 23.5 dBm at 94 GHz out of the isolator has been developed for this program, using 50 dB gain antennas for both transmitter and receiver, we expect that the transmitter-receiver pair can be operated over a maximum range of about 2 Km at 60 GHz and 5 Km at 94 GHz at rainfall rates up to 20 mm/hr. In Section 4.2, the test results for the developed oscillator pairs, i.e., TO-V-A/LO-V-A, TO-V-B/LO-V-B, TO-W-A/LO-W-A, and TO-W-B/LO-W-B, will be discussed to show that BER of less than  $10^{-7}$  was achieved.

#### Circuit Description

The regulator/modulator circuit specially developed for the IMPATT transmitter oscillators is shown in Figure 4.1-2. The IMPATT bias current was regulated at a fixed value by regulating the base current of the transistor MPS-UOS. Bias current modulation was achieved by shunting the current into the IMPATT diode with a large current, high



speed transistor, 2N4428. Modulation as high as 200 MHz at current levels above 400 mA is achieved with this circuit. The IMPATT LO bias current regulation circuit was constructed by removing the modulator circuit from the regulator/modulator circuit as shown in Figure 4.1-2. The frequency discriminator circuit is shown in Figure 4.1-3. The discriminator was constructed by placing a delay line on one of the two lines connecting the 2, 3-dB 90° hybrid couplers. Assuming an input RF voltage waveform of  $(\cos \omega t)$ , where  $\omega$  is the angular frequency and  $t$  is the time, the detector voltage output is proportional to  $\sin\left(\frac{\pi}{2} \frac{\Delta f}{f_0}\right)$  where  $f_0$  is the discriminator center frequency and  $\Delta f$  is the frequency deviation from  $f_0$ . And the delay line length  $\Delta L = v/(4f_0)$  where  $v$  is the propagation velocity in the line. Two matched tunnel diodes with video bandwidth of up to 150 MHz were used as detectors and the measured discriminator transfer characteristics are also shown in Figure 4.1-3, at two different signal input levels. Since the slope of the frequency-voltage transfer functions are different at different input levels, the input to the discriminator must be limited.

The AFC, search/lock circuitry is shown in Figure 4.1-4. It basically consists of a ramp voltage generator with adjustable search frequency and amplitude to drive the varactor tuned local oscillator. The detected signal (at the set threshold and above) after the AGC will disconnect the ramp generator switch (2N4857) to cease searching of the LO. The mean time, the AFC error detected at the discriminator output will adjust the LO bias to a proper value so that dc value of the discriminator will remain at zero output corresponding to center frequency 1.5 GHz of the discriminator. A ramp disable switch and an AFC disable switch are also provided to allow manual adjustment of the LO bias.

Figure 4.1-5 shows a photograph of the circuit box which contains the AGC, AFC, Search/lock and video circuitries with disabling switches

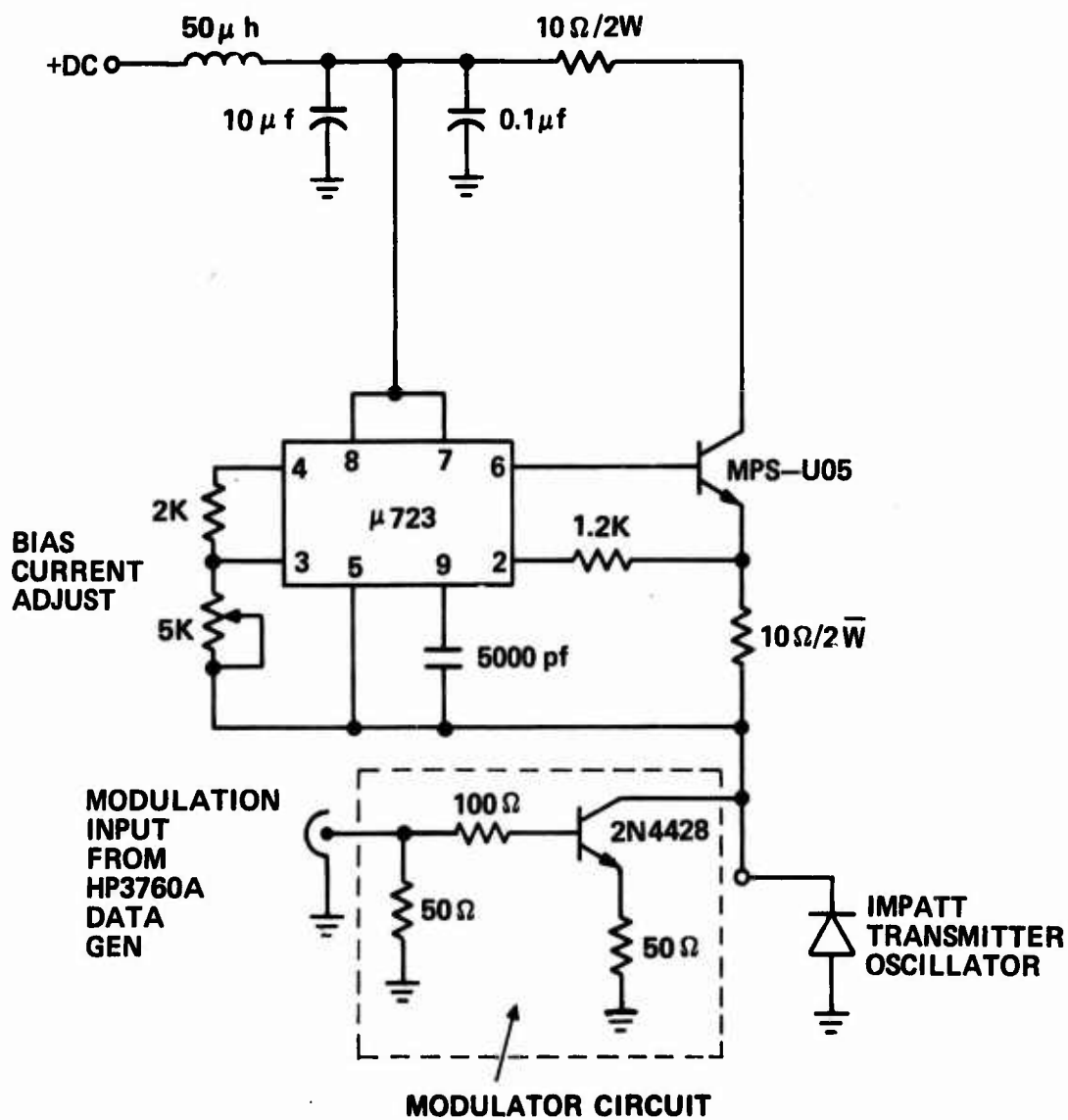


Figure 4.1-2 IMPATT transmitter oscillator regulator/modulator circuit.

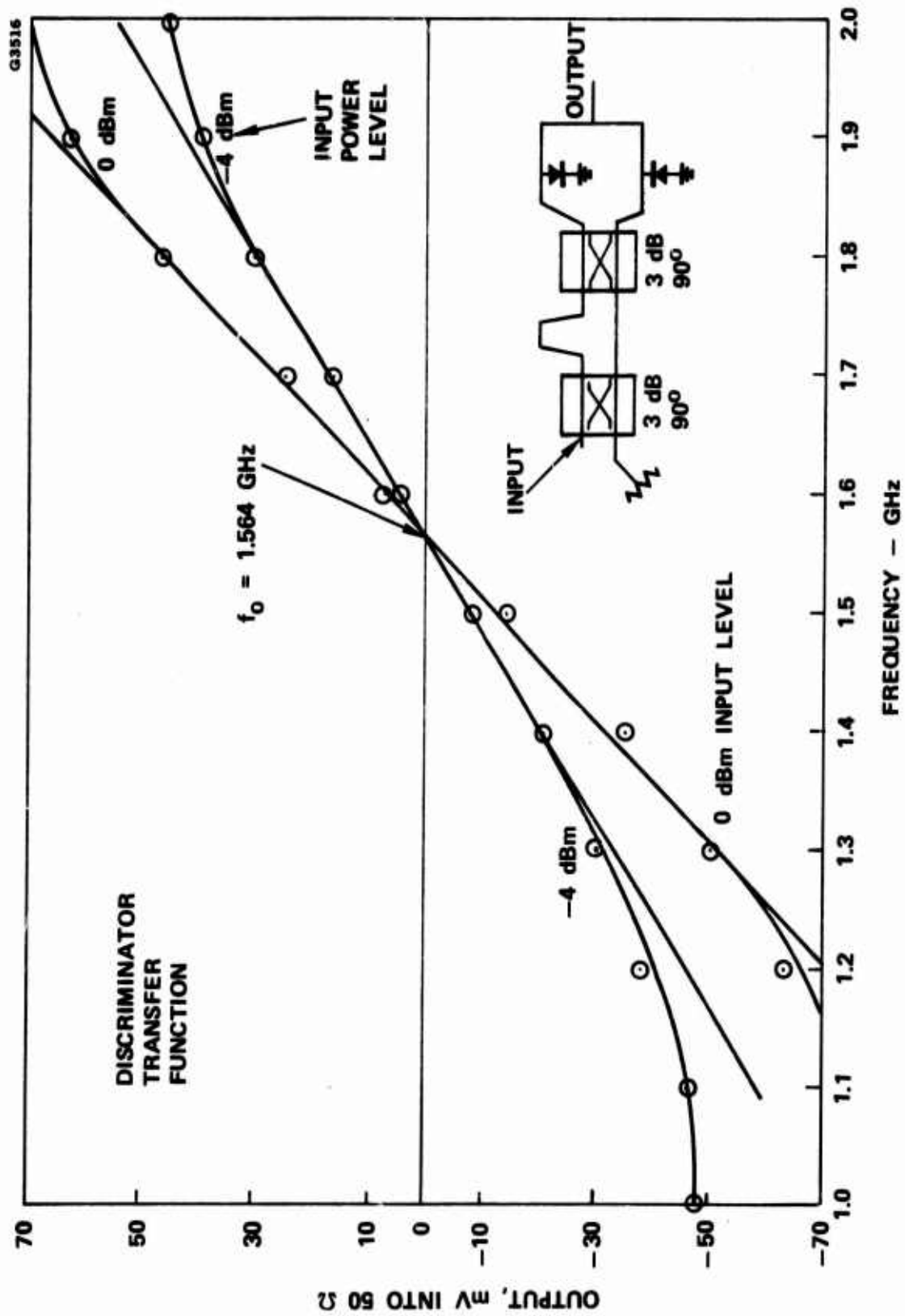


Figure 4.1-3 1-2 GHz frequency discriminator - measured results.

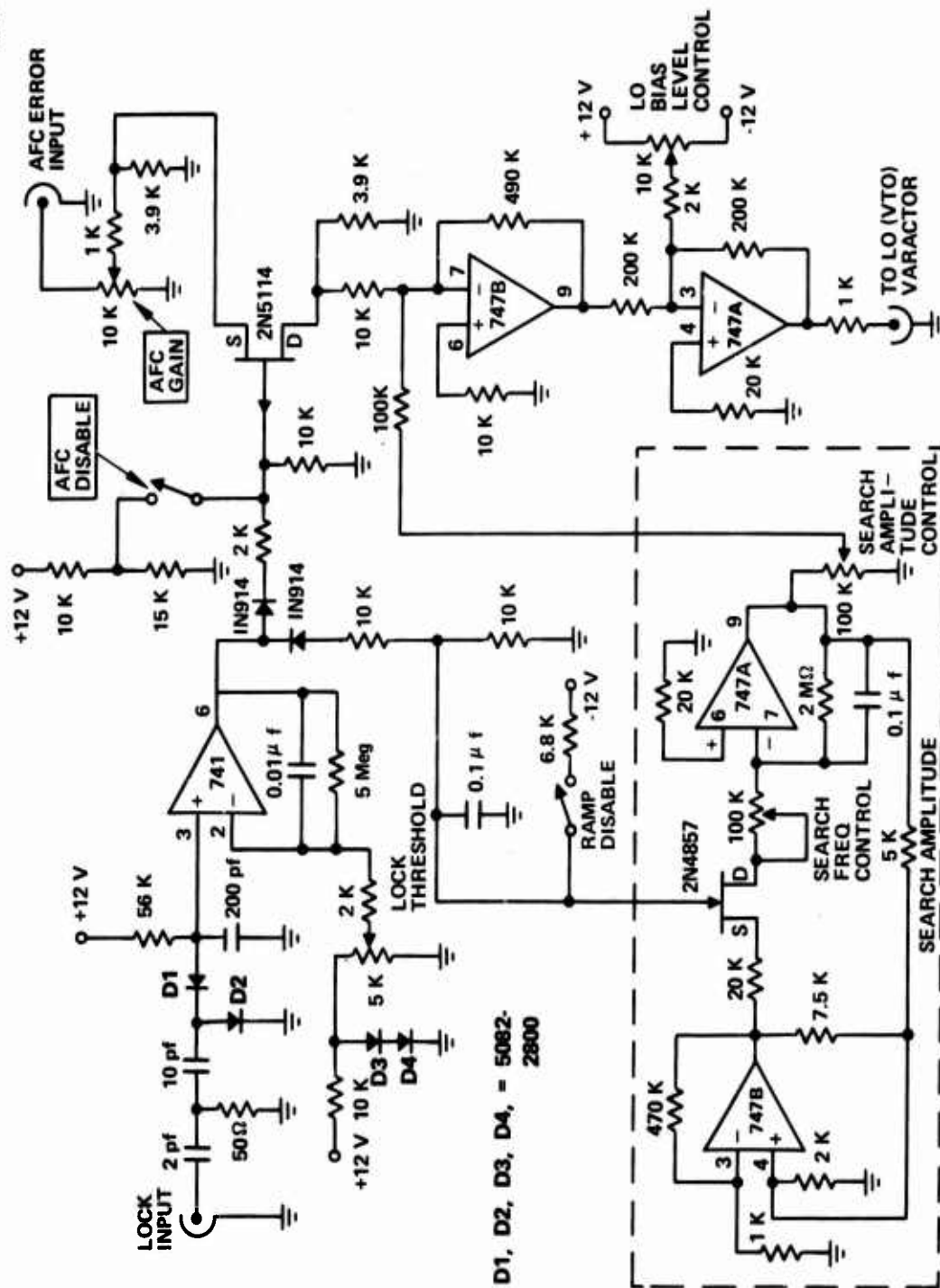


Figure 4.1-4 AFC, search/lock circuitry.

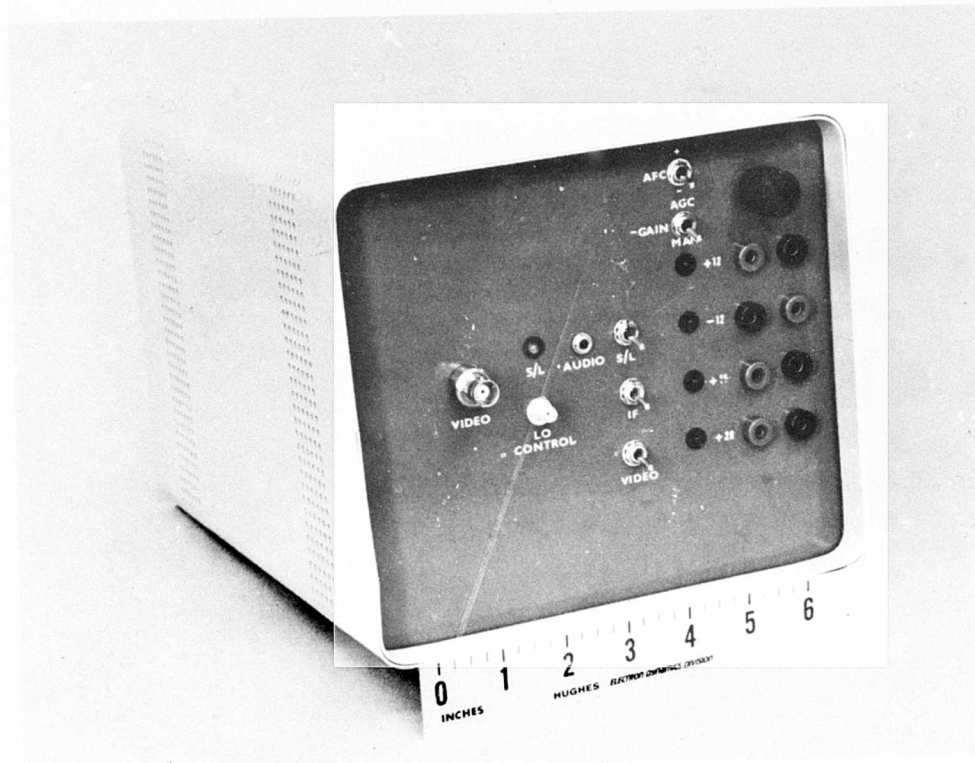


Figure 4.1-5 Photograph of the circuit box containing AGC, AFC, search/lock and video circuits.

to allow manual tuning of the AGC and LO frequency. An audio output was also provided for aligning the transmitter and receiver.

## 4.2 SYSTEM PERFORMANCE CHARACTERISTICS

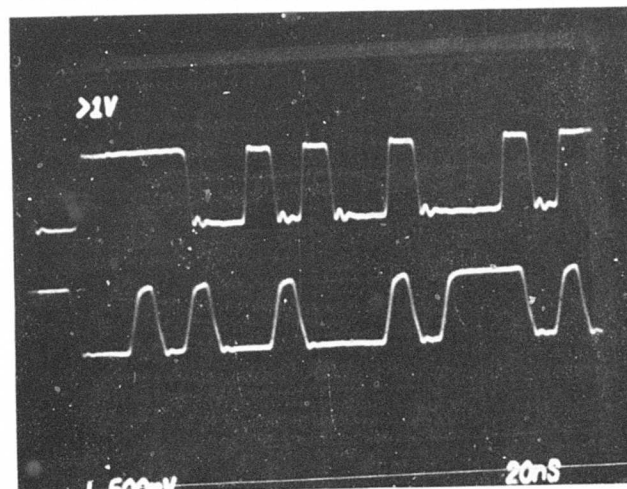
The typical detected video pulses for all the transmitter oscillators/LO pairs are shown in Figure 4.2-1 at the comparator circuit output. The data were obtained at the signal-to-noise ratio (S/N) of 16 dB and 100 megabits per second data rate of non-return-to-zero (NRZ). The detected pulses have an amplitude of 0.5 volts and were further amplified with a wideband pulse amplifier to drive the HP3761A error detector.

Spectral output of the signal was monitored with a spectrum analyzer at the i.f. amplifier output. Figure 4.2-2 shows the spectral picture of the pair TO-V-A and LO-V-A at 100 megabits/sec. data rate NRZ and word normal pattern 1010. The conditions are  $\Delta f = 100$  MHz and  $f_m = 50$  MHz corresponding to an index of modulation  $\beta = \Delta f / f_m = 2.0$ . The same spectral picture is shown in Figure 4.2-3 for the pair TO-W-A and LO-W-A, at 100 megabits/sec. data rate with word normal pattern 1010 NRZ, and at  $S/N = 16$  dB. The spectral picture is very clear. Figure 4.2-4 is the spectral picture of the same oscillator pair but at 200 megabits/sec. data rate, corresponding to  $\beta = 1$ . The spectrum is again very clean.

Figure 4.2-5 is the spectral picture of the pair TO-W-A/LO-W-A at 100 megabits per second data rate of Pseudo Random Binary Sequence (PRBS normal) of  $10^{10}-1$  word length generated by the HP3760A data generator.

The most important parameter for system evaluation of the transmitter/local oscillator pairs is the determination of the bit-error-rate (BER) of the FM data as a function of the detected signal-to-noise ratio ( $\gamma = S/N$ ). The desired BER for this program is required to be less than  $10^{-7}$  for the  $\gamma$  near the FM threshold of the receiver. Theoretically, for binary frequency-shift-keying (FSK), using rectangular frequency modulation and constant amplitude, the BER calculated for a

E1170



TRANSMITTED

RECEIVED  
(DELAYED)

Figure 4.2-1 Video data pulses output at 100 megabits/sec data rate. None-return-to-zero mode at S/N = 16 dB. Received data are arbitrarily delayed.



E1171

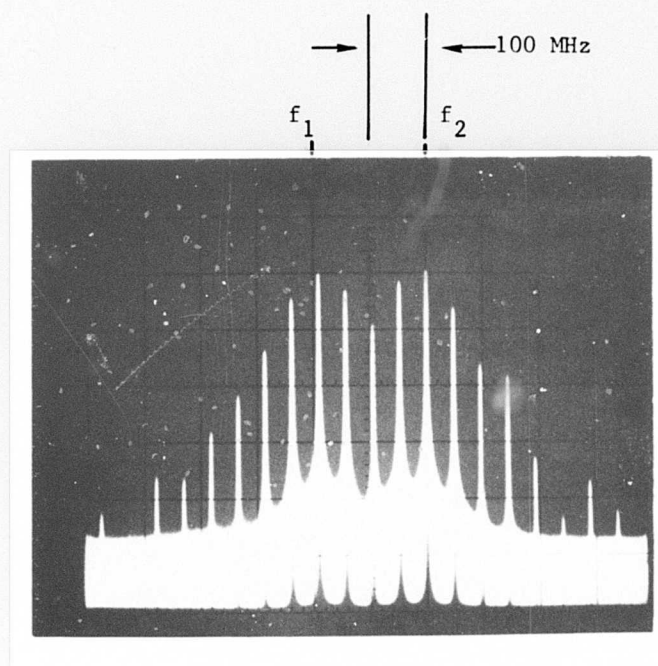


Figure 4.2-2 Spectral output of detected signal at 100 megabits/sec data rate NRZ. Word pattern 1010  $\Delta f = \pm 100$  MHz.

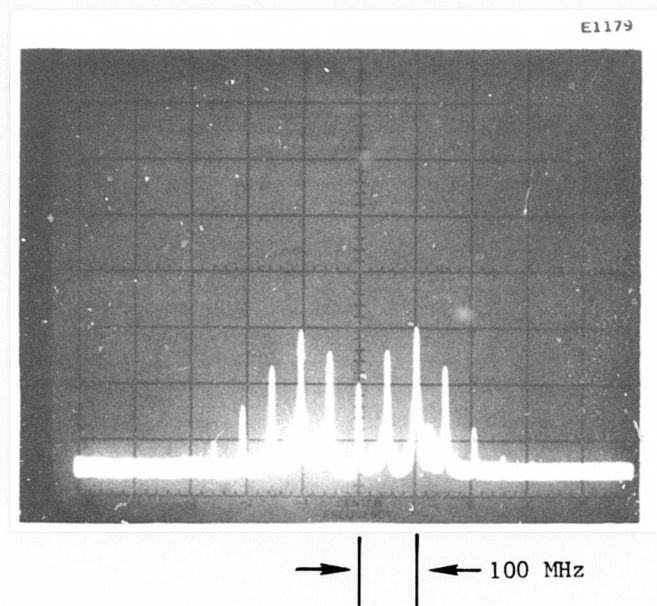


Figure 4.2-3 Spectral picture of the pair TO-W-A/LO-W-A, at 100 megabits/sec data rate with word normal pattern 1010 NRZ, and at S/N = 16 dB.

E1172

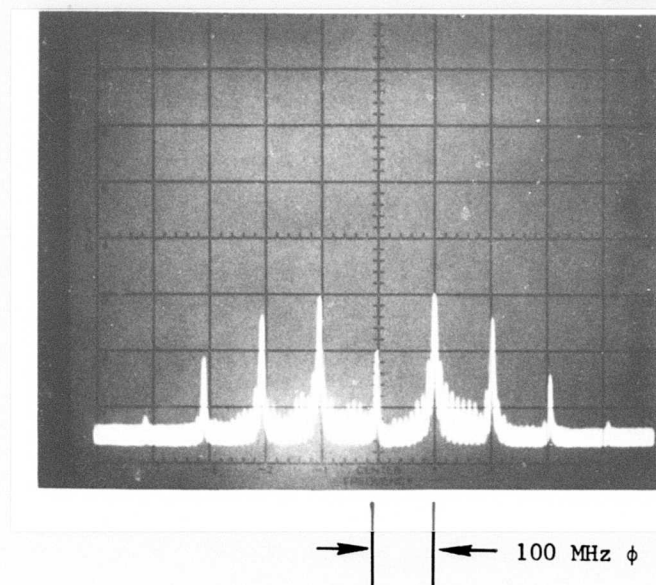


Figure 4.2-4 Spectral picture of the pair TO-W-A and LO-W-A at 200 megabits/sec data rate, 101010 word pattern NRZ, word normal  $10^{10}-1$ , and S/N = 16 dB.

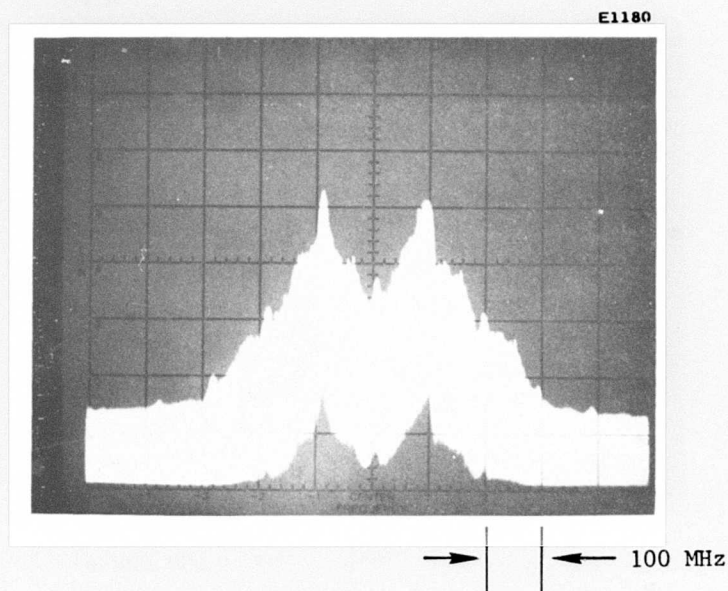


Figure 4.2-5 Spectral picture of the pair TO-W-A/LO-W-A at 100 megabits/sec data rate. Psuedo random binary sequence (PRBS normal) pattern of  $10^{10}-1$  word length was generated and detected.

noncoherent FSK system is an exponential function, (assuming no cross-talks between the two detected frequency shifts, called Mark and Space)

$$\text{BER} = 1/2 \exp (-\gamma/2)$$

based on pre-detection bandwidth wide enough to pass both Mark and Space waveforms.

The use of the comparator circuit after the frequency discriminator, however, resembles that of "sharp FM threshold" detection that no errors occur when the detected signal is larger than a certain pre-determined level and that errors occur with probability 1/2 when the signal is below the predetermined level.<sup>22</sup> The calculation shows

$$\text{BER} = 1/2 \exp (-\gamma)$$

Experimentally, intersymbol-interference effects, and the shape of the filters affect the detected BER. Normally, the relationship

$$\text{BER} = 1/2 \exp (-k\gamma)$$

followed where the factor k, lies between 0.6 and 0.8.<sup>22</sup>

BER measurements were made using the experimental setup shown previously at Figure 4.1-1. Pseudo random bit data of 100 megabits per second non-return-to-zero were generated with the modulation from the HP3760A data generator. The BERs were detected with the HP3761A error detector with digital display and with the use of the HP5055 Printer especially at low BER values for error detection over a long period of time to observe errors due to spontaneous noise generation in the environment surrounding the test setup. Since the BER measurements were conducted in a

laboratory environment without special precaution of noise shielding against low frequency noise leaking into the i.f. or measurement circuitries, the BER values obtained at low values, especially below  $10^{-8}$  were subject to errors showing deviations from the exponential laws as will be shown later in this section.

The measured BERs as a function of the system-to-noise ratio,  $\gamma = S/N$  are shown in Figure 4.2-6, 4.2-7, 4.2-8, and 4.2-9, respectively, for the pair TO-V-A/LO-V-A, TO-V-B/LO-V-B, TO-W-A/LO-W-A, and TO-W-B/LO-W-B. The pair TO-V-A/LO-V-A shows  $BER \sim 1/2 [\exp(-0.795\gamma)]$  between the noncoherent FSK and the FSK with sharp FM threshold. The deviations from the exponential law at low BER values were caused by system noise generated in the laboratory environment. BER of  $10^{-7}$  was achieved at  $\gamma = S/N = 13.4$  dB for the pair TO-V-A/LO-V-A, meeting the goal of this program.

The pair TO-V-B/LO-V-B shows BER results close to noncoherent FSK, which may be accidental. However, BER of less than  $10^{-7}$  was achieved at  $S/N = 15$  dB, also meeting our program goal.

The pair TO-W-A/LO-W-A shows  $BER = 1/2 \exp [-0.771 \gamma]$  as normally expected. Again  $BER = 10^{-7}$  was achieved at  $S/N = 13$  dB. The deviation from the exponential law at low BER values were again obvious.

The pair TO-W-B/LO-W-B, however, shows a BER worse than the noncoherent FSK values with BER of  $10^{-7}$  at  $S/N = 16.3$  dB. There was the possibility that noise generated in the laboratory may be excessive during the measurement of this pair. However, the BER degradation will not seriously affect the system performance at the desired  $S/N$  ratio with the  $S/N$  degradation in the order of 1 to 2 dB.



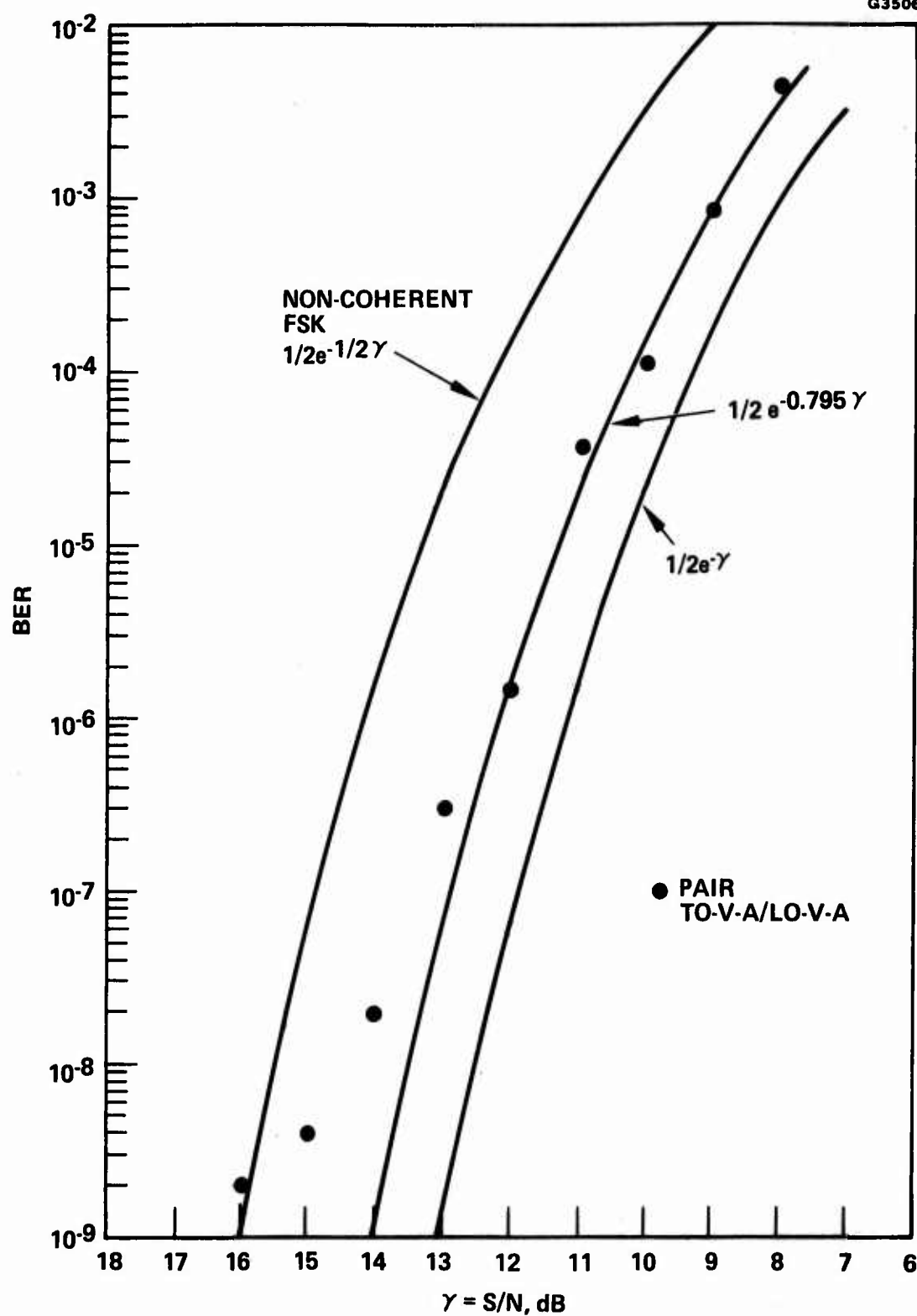


Figure 4.2-6 BIT-ERROR-RATE of the pair TO-V-A/LO-V-A.

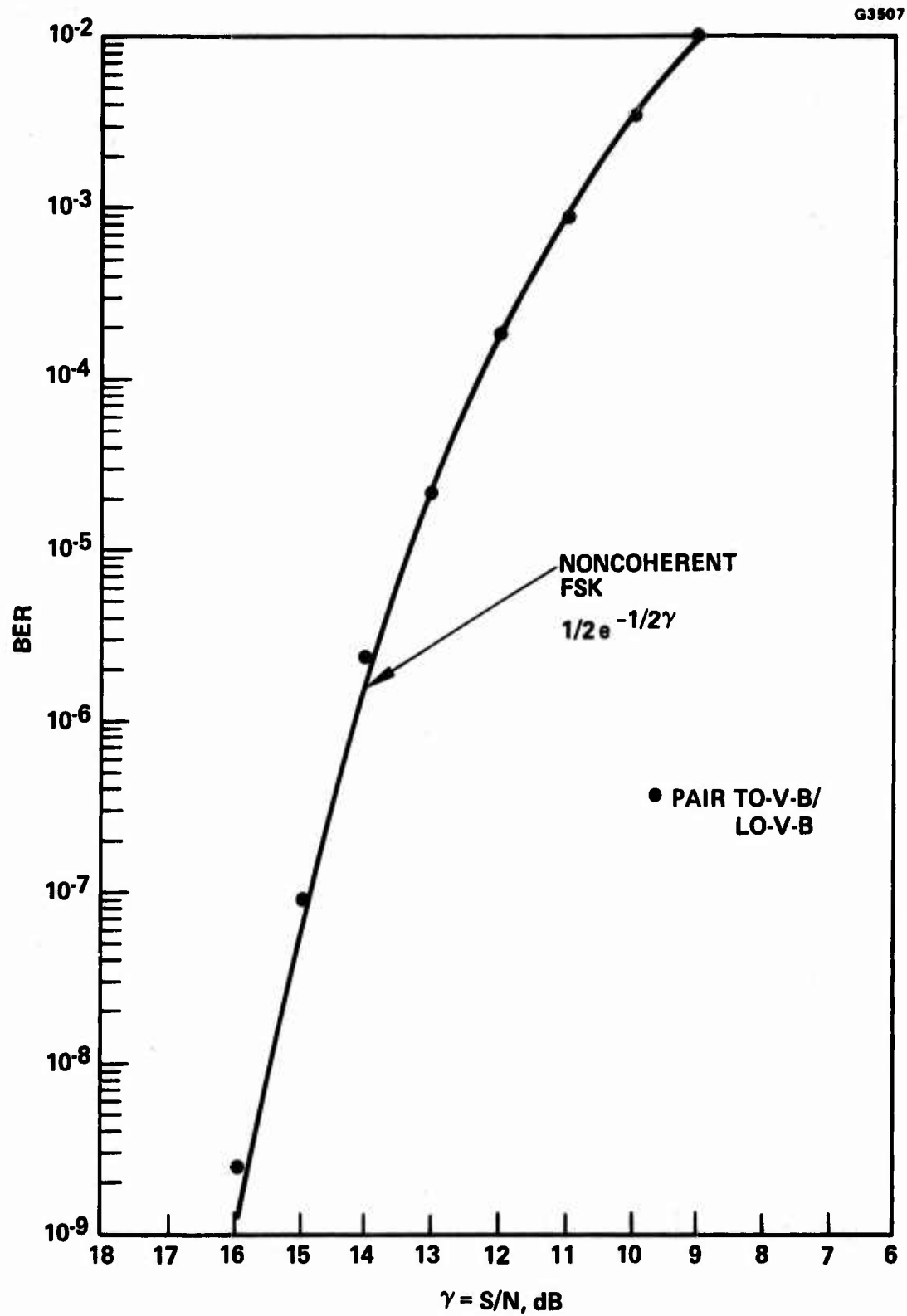


Figure 4.2-7 BIT-ERROR-RATE of the pair TO-V-B/LO-V-B.



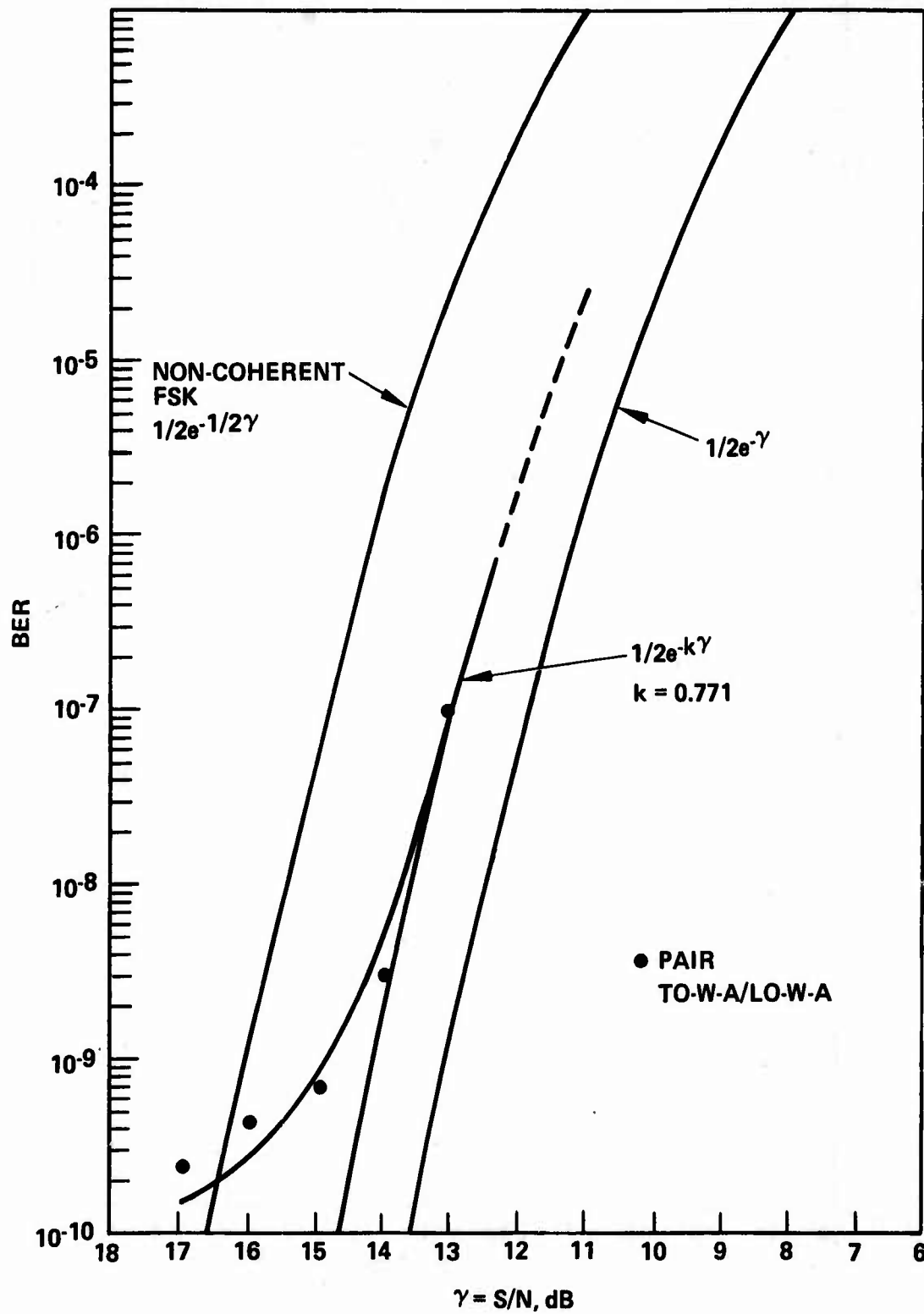


Figure 4.2-8 BIT-ERROR-RATE of the pair TO-W-A/LO-W-A.

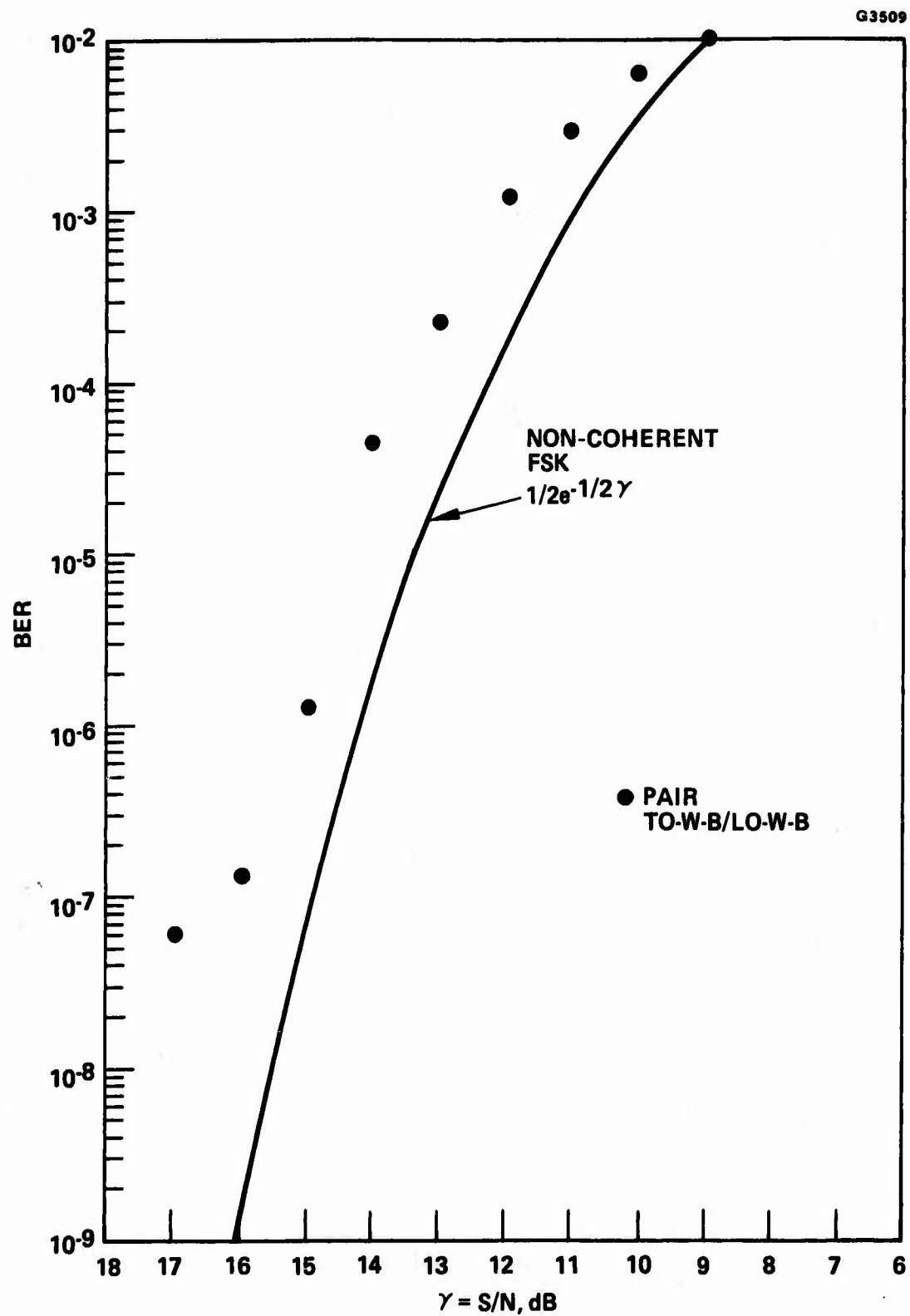


Figure 4.2-9 BIT-ERROR-RATE of the pair TO-W-B/LO-W-B.

## 5.0 CONCLUSIONS

This program clearly demonstrated that the silicon IMPATT diode oscillators can be successfully used as high power transmitter oscillators and low noise local oscillators for FM data communication of over 100 megabits per second data rate with BER of less than  $10^{-7}$  at S/N of 15 dB or less. According to Table 1.1 presented earlier in Section 1.0, most of the program goals have been achieved or close to the expected results in terms of output power, modulation, and noise.

Specifically, significant technical achievements developed in this program are listed as follows:

1. Diamond heatsinks for the 94 GHz FM IDIUs
2. Varactor-tuned-oscillators as the 60 GHz and 95 GHz LNLOUs
3. High data rate FM modulation up to 200 megabits/sec. data rate

However, the results also showed that we should expect better performance or improvement with future development effort on:

1. Improving diamond heatsink processing technique for large scale production.
2. Diamond heatsinks for 60 GHz FM IDIUs to improve the diode junction temperature, output power, and reliability.
3. Improving IMPATT circuit and device profile designs for large current density with low junction temperatures due to diamond heatsinks to allow the increase of oscillator efficiency, and output power.
4. Improving the IMPATT oscillator bias design to suppress excess noise away from carrier frequencies due to bias induced low frequency oscillations.

5. Further evaluation on the FM noise and loaded Q- factors of the oscillators
6. Reliability determination of small silicon double-drift IMPATT diodes on diamond heatsinks (60 and 94GHz diodes especially)
7. Further development of VTOs as local oscillators with wide tuning range.
8. The reproducibility of the oscillators to allow field-replacement of the devices in the military or combat environment.

The last (No. 8) of the future development goals is the most important one if millimeter-wave solid state devices are ever to be expected for large scale and wide spread usage. For this, not only further study and understanding of the device physics and device circuit interaction are necessary, it is also necessary to achieve standard diode processing techniques, diode packaging configuration, and diode and oscillator testing procedures.

## 6.0 ACKNOWLEDGEMENTS

The authors would like to thank Mr. W.R. Lane and Mr. G. Csanky for their special contribution to the double-drift IMPATT diode processing, fabrication, and packaging, and Mr. L.D. Thomas, Mr. C. Kruger, Mrs. B.E. Jaye, and Mr. G. Oransky for contributions on r.f. and i.f./video circuitry construction and testing.

#### REFERENCES

1. Scharfetter, D.L., W.J. Evans, and R.L. Johnston, "Double-Drift-Region ( $p^+pnn^+$ ) avalanche diode oscillators," Proc. IEEE (LETT), Vol. 58, pp. 1131-1133, July 1970
2. Lekholm A. and J. Mayr, "Computer Optimization of double-drift region IMPATT diodes," Electron. Lett., Vol. 9, pp/ 64-66, Feb. 1973
3. Sze S.M. and R.M. Ryder, "Microwave avalanche diodes," Proc. IEEE, Vol. 59, pp. 1140-1154, August 1971
4. Bernick, R.L., "Temperature profile and thermal spreading resistance for a semi-infinite type-IIa diamond heatsink," Electron. Lett., Vol. 8, pp. 180-181, 1972
5. Okuto, Y., "Junction temperature under breakdown conditions," Japan J. Appl. Phys., Vol. 8, pp. 917-922, 1969
6. Kenyon, N., and F. D'alessio, "Junction temperature measurement of IMPATT diodes," Electron. Lett., Vol. 8, pp. 118-119, 1972
7. Gibbons, G., "Transient temperature response of an avalanche diodes," Solid State Electron., Vol. 13, pp. 799-806, 1970
8. Seidel, T.E., R.E. Davis, and D.E. Iglesias, "Double-drift-region ion-implanted millimeter-wave IMPATT diodes," Proc. IEEE, Vol. 59, pp. 1222-1228, August 1971
9. Hirachi, Y., T. Nakagami, Y. Toyama, and Y. Fukukawa, "High power 50 GHz double-drift region IMPATT oscillators with improved

bias circuit for eliminating low-frequency instabilities," IEEE Trans. on Microwave Theory and Tech., Vol. MTT-24, pp. 731-737, November 1976

10. English, D.L., E.M. Nakaji, and R.S. Ying, "Improved performance of millimeter-wave IMPATT diodes on type-IIa diamond heatsinks," Electron. Lett., Vol. 12, pp. 675-676, December 1976.
11. Kurokawa, K., "Some basic characteristics of broadband negative resistance oscillator circuits," BSTJ, Vol. 48, pp. 1937-1955, August 1969
12. Ohtomo, M. "Experimental evaluation of noise parameters in Gunn and avalanche oscillators," IEEE Trans. on Microwave Theory and Tech., Vol. MTT-20, pp. 425-437, July 1972
13. Kuvas, R.L., "Nonlinear noise theory for IMPATT diodes," IEEE Trans. on Electron Devices, Vol. ED-23, pp. 395-411, April 1976
14. Weller, K.P., "Solid state millimeter wave sources," presented in 1976 WESCON, Los Angeles, September 14-17, 1976
15. OKamoto, H., "Noise characteristics of GaAs and Si IMPATT diodes for 50-GHz range operation," IEEE Trans. On Electron Devices, Vol. ED-22, pp. 558-565, August 1975
16. Singh, D.N., "AM noise of millimeter-wave Gunn oscillators," IEEE Trans on Electron Devices, Vol. Ed-23, pp. 1350-1351 December 1976

17. Thaler, H., G. Ulrich, and G. Weidmann, "Noise in IMPATT diode amplifiers and oscillators," IEEE Trans. on Microwave Theory and Tech., Vol. MTT-19, pp. 692-705, August 1971
18. Niehaus, W.C., T.E. Seidel, and D.E. Iglesias, "Double-drift IMPATT diodes near 100 GHz," IEEE Trans. on Electron Devices, Vol. ED-20, pp. 765-771, Sept. 1973
19. Denlinger, E.J., J. Rosen, E. Mykietyn, and E.C. McDermott, Jr., "Microstrip Varactor-tuned millimeter-wave IMPATT diode oscillators," IEEE Trans. on Microwave Theory and Tech., Vol. MTT-23, pp. 953-958, December 1975
20. Cawsey, D., "Wide-range tuning of solid-state microwave oscillators," IEEE So. Journal of Solid State Circuits, (Corresp.) Vol. SC-5 pp. 82-84, April 1970
21. Paik, S.F., "Q degradation in varactor-tuned oscillators," IEEE Trans. on Microwave Theory and Tech., Vol. MTT-22, pp. 578-579, May 1974
22. Schwartz, M., W.R. Bennet, and S. Stein, "Communication Systems and Techniques," International Electronics Series Vol. 4, McGraw-Hill, 1966



# DISTRIBUTION LIST

	<u># of Copies</u>		<u># of Copies</u>
Defense Documentation Center ATTN: DDC-TCA Cameron Station (Bldg 5) Alexandria, VA 22314	2	Commander USA Mobility Eqpt R&D Cmd ATTN: SMEFB-R Fort Belvoir, VA 22060	2
Office of Naval Research Code 427 Arlington, VA 22217	1	Commander US Army Materiel Development and Readiness Command ATTN: DRCDE-R 5001 Eisenhower Ave. Alexandria, VA 22333	1
Naval Ship Engineering Center ATTN: Code 6157D Prince Georges Center Hyattsville, MD 20782	1	NASA Scientific & Tech Info Fac ATTN: Acquisitions Br(S-AK/DL) Baltimore/Washington International Airport- P.O. Box 8757 Md	2
Commander Naval Electronics Lab Center ATTN: Library San Diego, CA 92152	1	Advisory Group on Electron Devices 201 Varick Street, 9th Fl. New York, NY 10014	2
Commander US Naval Ordnance Lab ATTN: Technical Library White Oak Silver Spring, MD 20910	1	Director Naval Research Laboratory ATTN: Code 2627 Washington, DC 20375	1
Rome Air Development Center ATTN: Documents Library (TILD) Griffis AFB, NY 13441	1	Cdr, U.S. Army Signals Warfare Lab ATTN: DELSW-OS Arlington Hall Station Arlington, VA 22212	1
HQ ESD (DRI) L. G. Hanscom AFB Bedford, MA 01730	1	Director Defense Communications Agency Technical Library Center Code: 205 Washington, DC 20305	1
OSASS-RD Washington, DC 20310	1	Director Naval Research Laboratory ATTN: Mr. Eliot Cohen Code: 5211 Washington, DC 20375	1
Commander, MIRCOM Redstone Scientific Info Ctr ATTN: Chief, Document Section Redstone Arsenal, AL 35809	2		
Commander Harry Diamond Laboratories ATTN: Library 2800 Powder Mill Rd. Adelph, MD 20783	1		

	<u># of Copies</u>		<u># of Copies</u>
Commander USASATCOMA Fort Monmouth, NY 07703 ATTN: Technical Director	1	Texas Instruments, Inc. Semiconductor Rsch & Eng Labs ATTN: Dr. Turner E. Hasty, Dir. P. O. Box 5012, M.S. 72 Dallas, TX 75222	1
AIL, Division of Cutler Hammer Inc. ATTN: Dr. Jesse Taub Deer Park, L.I., N.Y. 11729	1	Varian Associates ATTN: Dr. Berin Fank 611 Hansen Way Palo Alto, CA 94304	1
AFAL/TEM ATTN: Richard Remski Wright Patterson AFB, OH 45433	1	Alpha Industries, Inc. Dr. Walter Niblack 20 Sylvan Road Woburn, Massachusetts 01801	1
RCA Laboratories David Sarnoff Research Center ATTN: Dr. Barry Perleman Princeton, NJ 08540	1	Renesselaer Research Corp. Dr. Ken Mortenson, President 1125 Peoples Avenue Troy, NY 12181	1
Dr. George Haddad, Director Electron Physics Laboratory University of Michigan Ann Arbor, Michigan 48104	1	Dr. Lester Eastman Dept. Electrical Engineering Cornell University Ithaca, NY 14850	1
Director US Army Ballistic Missile Defense Advanced Technology Center ATTN: ATC-R, Mr. George Jones P.O. Box 1500 Huntsville, AL 35807	1	Dr. Robert Ryder Bell Labs Murray Hill, NJ	1
TRW, Inc. Radio Frequency Laboratory ATTN: Dr. Jorge Rau Redondo Beach, CA 90278	1	Raytheon Company SMDO 130 Second Avenue Waltham, Mass 02154 ATTN: Dr. Frank Paik	1
Institute of Defense Analysis Arlington, VA 22209	1	Raytheon Company Research Division 28 Seyon Street Waltham, Mass ATTN: Mr. Bob Beirig	1
Microwave Associates, Inc. ATTN: Mr. W. G. Matthei South Avenue Burlington, MA 01803	1		
Westinghouse Defense & Space Center Box 1521 MS 3717 Baltimore, Md 21203 ATTN: Dr. Mary Cohn	1		

# of Copies

Cdr, CERCOM	1	MIT/Francis Bitter Natl Magnet Lab
ATTN: DRSEL-PL-ST	2	ATTN: K. J. Button
ATTN: DRSEL-MS-TI		170 Albany St.
Fort Monmouth, NJ 07703		Cambridge, MA 02139
Cdr, ERADCOM	1	
ATTN: DELET-DD	1	
ATTN: DELET-DT	1	
ATTN: DELET-B	1	
ATTN: DELET-I	1	
ATTN: DELET-P	1	
ATTN: DELET-E	1	
ATTN: DELET-M	1	
ATTN: DELET-MJ (Contr file)	2	
ATTN: DELET-MF	1	
ATTN: DELET-MM	1	
ATTN: DELET-MK	1	
ATTN: DELET-MJ (A.Kerecman)	11	
Fort Monmouth, NJ 07703		
Case Western Reserve University	1	
School of Engineering		
ATTN: Dr. Joseph E. Rowe		
Vice Provost and Dean		
312 Glennan Building		
Cleveland, OH 44106		
Raytheon Company	1	
Microwave & Power Tube Division		
ATTN: Mr. Lawrence L. Clampitt		
190 Willow Street		
Waltham, MA 02154		
Director, Applied Physics Lab	1	
Sperry Research Center		
ATTN: Dr. Richard Damon		
Sudbury, MA 01776		
University of Washington	1	
Dept of Electrical Engineering		
ATTN: Dr. Daniel G. Dow		
Seattle, WA 98195		
University of Illinois	1	
Dept of Electrical Engineering		
200 EERL		
ATTN: Dr. Paul D. Coleman		
Urbana, Illinois 61801		